STATISTICAL MODELING OF LAPPED TRANSFORM COEFFICIENTS AND ITS APPLICATIONS

A

Thesis Submitted

in Partial Fulfilment of the Requirements

for the Degree of

DOCTOR OF PHILOSOPHY

By

VIJAY KUMAR NATH

to the

DEPARTMENT OF ELECTRONICS AND ELECTRICAL ENGINEERING

INDIAN INSTITUTE OF TECHNOLOGY GUWAHATI

GUWAHATI - 781039, ASSAM, INDIA

MARCH 2011

STATISTICAL MODELING OF LAPPED TRANSFORM COEFFICIENTS AND ITS APPLICATIONS

Vijay Kumar Nath

Certificate

This is to certify that the thesis entitled "**STATISTICAL MODELING OF LAPPED TRANSFORM COEFFICIENTS AND ITS APPLICATIONS**", submitted by **Vijay Kumar Nath** (03610203), a research scholar in the *Department of Electronics and Electrical Engineering, Indian Institute of Technology Guwahati*, for the award of the degree of **Doctor of Philosophy**, is a record of an original research work carried out by him under my supervision and guidance. The thesis has fulfilled all requirements as per the regulations of the Institute and in my opinion has reached the standard needed for submission. The results embodied in this thesis have not been submitted to any other University or Institute for the award of any degree or diploma.

Dated:

Guwahati

Dr. Anil Mahanta
Professor
Dept. of Electronics and Electrical Engg.
Indian Institute of Technology Guwahati
Guwahati - 781039, Assam, India.

To my parents, wife and daughter

Acknowledgements

First of all, I would like to thank my supervisor Prof. Anil Mahanta for his valuable guidance, moral support and endless encouragement. His kindness, dedication, accessibility and attention to detail have been a great inspiration to me. I would particularly like to thank him for his help in patiently and carefully correcting all my manuscripts. I would also like to thank my doctoral committee members, Dr. P. K. Bora, Dr. S. Dandapat and Dr. R. Paily. Their suggestions and assistance have been very valuable. I am thankful to Mr. Sanjib Das, Mr. L. N. Sharma and Ms. S. Josephine, Scientific Officers in the Department, for their help during the entire course of this work. I am grateful to all the faculty and the staff members of EEE Department.

Among my friends, I would like to extend my thanks to Dr. Babusena Paul, Dr. Prabin Padhi, Mr. Bhabesh Deka, Dr. Vinod P, Ms. Amrita Ganguli, Dr. M. Singh, Mr. K. C. Narsimhamurthy and Dr. Ali. I would like to extend my special thanks to Ms. Amrita Ganguly from whom I learnt most of the little I know about LATEX.

My parents, wife, brother and sister were always with me - their love and confidence gave me strength when I needed it most. Finally, I am specially thankful to my wife and my daughter, Deepika and Ananya, for their love and patience throughout my Ph.D program.

(Vijay Kumar Nath)

Abstract

In the last two decades, statistical modeling in wavelet domain has been an active research area due to its multiresolution and time frequency localization properties. These properties have been efficiently exploited in many image processing applications like image compression, denoising, deblocking, deblurring etc with considerable success. The main drawback of wavelet transform is that it is not very good in capturing the directional information present in natural images.

The Lapped Transforms have been proposed to overcome the blocking artifacts of the DCT with increased coding gain. It was observed that the Lapped Transforms (LT) based methods are very good in preserving oscillatory components present in images like textures. This thesis deals with statistical modeling of LT coefficients of natural images and its applications.

The thesis first considers an exhaustive study on the determination of a suitable statistical distribution that best approximates the block Lapped Orthogonal Transform (LOT) and Lapped Bi-orthogonal Transform (LBT) coefficients. The widely used Kolomogrov-Smirnov (KS) and Chi-square goodness of fit tests indicate that the Generalized Gaussian is the most appropriate statistical distribution that best approximates the block LOT and LBT coefficients of natural images. Such a study is very useful in the design of optimal quantizers that may lead to minimum distortion. Employing the dyadic remapping feature of LTs, the LT coefficients can be rearranged into octave-like representation. The rearranged LT coefficients in various detailed subbands show highly non Gaussian statistics and can be modeled in a way similar to wavelet coefficients. The dyadic remapped LT coefficients when used in compression and denoising applications show performance comparable to that of wavelet based methods. This thesis next considers an exhaustive study on the determination of a suitable statistical distribution that best models the dyadic remapped LT coefficients. The experimental results indicate that the Generalized Gaussian distribution best approximates the dyadic remapped LT coefficients. Such a study plays an important role in developing more efficient algorithms for compression and denoising applications.

The problem of reducing additive white Gaussian noise in LOT domain is considered in the thesis. The main motivation is that LOT has good energy compaction, it is robust to oversmoothing and the noise and the signal statistics can be modeled precisely in the LT domain. We propose three LT based image denoising methods based on statistical modeling of dyadic rearranged LT

coefficients. The first method uses a Bayesian minimum mean square error (MMSE) estimator based on modeling the global distribution of dyadic rearranged LT coefficients by Generalized Gaussian distribution. The second method assumes the local distribution of the rearranged LT coefficients to be Gaussian with spatially varying variance and applies local Wiener filter to reduce the noise. Based on the encouraging performance of single local Wiener filtering in LT domain, a doubly local Wiener filtering framework is developed in the same domain. The third method employs a maximum a posteriori (MAP) estimator which uses the local Laplace probability density function with local variance for the estimation of the noise free coefficients. Experimental results show the effectiveness of the proposed statistical models in reducing the additive white Gaussian noise while preserving edges and textures.

The thesis also focuses on the reduction of blocking and ringing artifacts in the orthogonal LT domain. The good denoising property of LTs is utilized for reducing the blocking artifacts from the block DCT compressed images. Two LT based methods are proposed for reducing the blocking and ringing artifacts from the block DCT compressed images. The first method is based on soft thresholding of rearranged orthogonal LT coefficients and requires very low computational complexity. A global, adaptive threshold is proposed which significantly reduces the blocking artifacts in LT domain and shows significant increase in PSNR results. The second method is a two stage method which is based on combined LT and adaptive bilateral filtering. The first stage reduces the blocking artifacts in LT domain using local Wiener filtering and the second stage reduces the residual artifacts in time domain. The bilateral filter parameter selection is made adaptive to the quantization tables used in the compression process. The experimental results show the effectiveness of the proposed techniques in reducing the blocking and ringing artifacts in block DCT compressed images while preserving the edges and textures.

Contents

List of Figures

List of Tables

List of Acronyms

2-D	Two-dimensional
3-D	Three-dimensional
CDF	Cumulative distribution function
CBIR	Content based image retrieval
DCT	Discrete cosine transform
DHT	Discrete Hadamard transform
DWT	Discrete wavelet transform
EZW	Embedded zerotree wavelet
GOF	Goodness of fit
HMT	Hidden Markov tree
JPEG	Joint photographic experts group
KLT	Karhunen Loeve transform
KS	Kolomogrov Smirnov
LAWML	Locally adaptive window-based denoising using ML (wavelet domain)
LAWMAP	Locally adaptive window-based denoising using MAP (wavelet domain)
LMMSE	Linear minimum mean square error
LOT	Lapped orthogonal transform
LOT-HMT	Image denoising algorithm using hidden Markov tree in LOT domain
LOT-GG	LOT domain image denoising method based on Generalized Gaussian prior
LOT-Lap	LOT domain image denoising method based on local Laplace prior
LOT-LWF-ML	Local Wiener filtering algorithm in LOT domain using ML
LOT-LWF-MAP	Local Wiener filtering algorithm in LOT domain using MAP
LT	Lapped transform
LT1	Lapped transform-1
LT2	Lapped transform-2

LTDLWF	Doubly local Wiener filtering algorithm in LT domain
LBT	Lapped bi-orthogonal transform
MMSE	Minimum mean square error
MAP	Maximum a posteriori
ML	Maximum likelihood
MSE	Mean square error
pdf	probability density function
PSNR	Peak signal to noise ratio
SA-DCT	Shape adaptive - DCT
SNIG	Symmetric normal inverse Gaussian
SPIHT	Set partitioning in hierarchical trees
SSIM	Structural similarity
WT-GG	Wavelet based image denoising method based on Generalized Gaussian prior
WT-Lap	Wavelet based image denoising method based on local Laplace prior

List of Symbols

$*$	convolution operator
κ_x	kurtosis of the histogram (noise free signal)
$\sigma_x^2(k)$	variance (noise free signal) at a position k
σ_s	bilateral filter parameter which controls the weight in spatial domain
σ_i	bilateral filter parameter which controls the weight in intensity domain
$\widehat{\sigma}_{xp}^2(k)$	signal variance estimated from the pilot image at a position k
$\sigma_y^2(k)$	variance (noisy signal) at a position k
σ_n^2	variance (noise)
η_t	additive noise in time domain
λ	rate parameter in the pdf of an exponential distribution
ρ	intersample correlation coefficient
χ^2	chi-square
μ	mean
$\Gamma(.)$	Gamma function
α	scale parameter in generalized Gaussian pdf
α_s	parameter which controls the steepness of the SNIG distribution
β	shape parameter in generalized Gaussian pdf
β_s	asymmetry parameter of SNIG pdf
δ	scale parameter of SNIG pdf
$\psi(.)$	digamma function
$\Delta(u,v)$	quantization interval of $(u,v)^{th}$ DCT coefficients
b	scale parameter in Laplace pdf
$C(.)$	cost function
C_0	columns of an image
$\tilde{C}(j)$	transform coefficient of the pilot image at position j

dB	decibel
D	matrix whose columns are the basis functions
D_e	Even DCT functions
D_o	Odd DCT functions
$\tilde{d}$	image which does not satisfy the quantization constraint
E_i	expected frequency in bin B_i
$\tilde{F}_X(x)$	empirical CDF of X at a point x
$F_X(x)$	model CDF of X at a point x
$f_X(x)$	probability density function
F	normalization factor
G_{TC}	transform coding gain
G	number of coefficients in $Z(k)$
$HH1$	diagonally oriented (2D) subband (1st level)
$HH2$	diagonally oriented (2D) subband (2nd level)
$HH3$	diagonally oriented (2D) subband (3rd level)
$HH4$	diagonally oriented (2D) subband (4th level)
$HL1$	horizontally oriented (2D) subband (1st level)
$HL2$	horizontally oriented (2D) subband (2nd level)
$HL3$	horizontally oriented (2D) subband (3rd level)
$HL4$	horizontally oriented (2D) subband (4th level)
I	identity matrix
J_d	number of decomposition levels
J	counter identity matrix
k_s	sample kurtosis
K_1	modified Bessel function of the second kind of order 1
KS_{stat}	Kolomogrov Smirnov statistic
L	input signal length
$LH1$	vertically oriented (2D) subband (1st level)
$LH2$	vertically oriented (2D) subband (2nd level)
$LH3$	vertically oriented (2D) subband (3rd level)
$LH4$	vertically oriented (2D) subband (4th level)
$\tilde{m}$	set of DCT coefficients of image $\tilde{d}$

m	sample mean
M	output signal length
$M4y$	fourth moment (noisy image)
n	additive white Gaussian noise
N	number of observations
O_i	observed frequency in bin B_i
P	*feasible* LOT matrix
P_0	optimal LOT matrix
P_f	LBT synthesis matrix
P_i	LBT analysis matrix
Q_f	JPEG image quality factor
Q_1	block DCT quantization table
Q_2	block DCT quantization table
Q_3	block DCT quantization table
Q_{av}	average of first 3x3 values of the quantization table
R_0	rows of an image
R_{xx}	signal covariance matrix
S	shift operator
$S_{T_h}(.)$	soft thresholding operator
T_h	threshold
T	transform matrix
$V(k)$	output of the bilateral filter at a spatial position k
v	sample variance
$x(k)$	noise free signal in transform domain at a position k
x_t	original uncompressed signal
$y_{LT2}(k)$	coefficients of the noisy signal in LT2 domain at a position k
$y(k)$	noisy signal in transform domain at a position k
y_t	block DCT decompressed signal
Y_f	scaling matrix in the forward transformation in LBT
Y_i	scaling matrix in the inverse transformation in LBT
z	original input vector
Z	orthogonal matrix

$Z(k)$	square shaped window centered at a given position

Chapter 1

Introduction

The procedure of analysis, storage, manipulation and display of digital images by digital computer from various sources is known as digital image processing. Digital image processing has a wide range of applications and many theoretical and technological developments have taken place in the last two decades. Two broad areas of research in image processing field are :

1. Analysis and development of fundamental image representation and modeling.
2. The wide range of applications which takes the maximum advantages from the analysis and developments of image representation and modeling.

Both areas of research are very closely related to each other. This thesis focuses on both the areas i.e. image modeling and some of its applications.

Images are usually described by simple statistical models in image processing. The objective of statistical modeling is to capture the important characteristics of natural images in the form of a few parameters which can be used as prior model information in various image processing applications like image denoising, compression etc. It is well known that the image processing performance can be significantly enhanced if the prior model information is known. A simple, efficient and accurate model is a very important factor in various image processing problems. For example, in image denoising applications, a Bayesian estimator like minimum mean square error (MMSE) estimator or maximum a posteriori (MAP) estimator is developed using the prior statistical distribution information to denoise the noisy transformed coefficients. Since real world images consist of combinations of small or large smooth regions, edges, textures and many other important details, the appropriate modeling becomes a very tough problem. The ability of spatial domain models to describe the large scale behavior is limited. In the last two decades, researchers have focussed more on statistical modeling in the transform domain. Natural images are well characterized by their singularity structure- the

discrete wavelet transforms (DWT) [77] are able to capture this singularity structure and hence provide an appropriate domain for image modeling. Wavelet transforms have become very popular over the Fourier transform due to their multiresolution and time frequency localization properties. The important characteristics of wavelet transforms which allow for efficient image processing in wavelet transform domain are:

1. Each coefficient represents the content of the image localized in space and frequency,
2. The image can be represented by wavelet transform at a nested set of scales,
3. The edges in images in the wavelet transform domain are represented by large magnitude coefficients at the corresponding spatial positions,
4. Wavelet coefficients of natural images tend to be approximately decorrelated,
5. Wavelet transforms can achieve good sparsity for spatially localized details, such as edges and singularities.

The separable two dimensional discrete wavelet transforms (DWT) has been widely used in many image and video processing applications. The DWT gives sparse representations for digital images, as a result of which various DWT based algorithms have been proposed in the literature for efficient signal and image statistical analysis. In applications like image denoising, compression, compression artifacts removal etc. the DWT has shown excellent results. The motivation for denoising in the wavelet domain is that the wavelet transforms has excellent energy compaction- the large coefficients represent the important signal informations and small coefficients are likely to be caused by noise. Several approaches have been proposed in the literature in statistical wavelet based denoising [7, 21, 22, 26, 38, 40, 43, 51, 63]. One popular approach is to design a statistically optimal threshold for a nonlinear thresholding. Generally, thresholding is carried out on one coefficient at a time. In thresholding process, each coefficient is thresholded by comparing it with a given threshold, if the coefficient is found to be greater than the given threshold, then the coefficient is kept or modified, else it is set to zero. Another approach is to design a shrinkage function by minimizing Bayesian risk under the maximum a posteriori (MAP) criterion. When MAP estimator is used the *a priori* knowledge about the distribution of wavelet coefficients is required. In the literature, several probability density functions like Gaussian, Laplacian, Generalized Gaussian, Symmetric Normal Inverse Gaussian (SNIG) [7, 51, 63] and many others were proposed for modeling the noise free wavelet coefficients.

Researchers have also applied wavelet transforms in reducing the compression artifacts of the block DCT compressed images [30, 42, 81, 83]. The main challenge in image deblocking [2, 25, 30, 42, 50, 55, 57, 58, 65, 81, 84, 86–88, 90] problem is to smooth the blocking artifacts without smoothing the edges and textures. The good denoising property of wavelet transforms is used in reducing the blocking artifacts.

Although wavelet transforms have shown very good performance in many image processing applications, they are not very good in capturing the 2-D singularities found in images. It is well known that edges and textures contain most important information of the image signal and represent the structural properties of an image. As we know it is the edges and textures that stimulate our human visual system and pass on the visual information to our mind. Hence, the preservation of edges and textures are highly important in almost all image processing tasks.

Lapped Transforms (LT) [45–48] have shown encouraging results in the field of image compression and denoising when compared with wavelet transform based algorithms [18, 19, 64, 85]. It is observed that the LTs are very good in preserving the oscillatory components in images such as textures in natural images. LTs are generally viewed as block transforms, composed of M passband filters. LTs have higher coding gain compared to DCT. The lapped orthogonal transform (LOT) [44] has been proposed to overcome the blocking artifacts of the DCT because of its extended basis functions which overlap across its block boundaries. For a block of M samples, the LT bases have a length of $L = 2M$ [44]. LOT strongly reduces blocking artifacts but do not totally eliminate them because the basis functions do not decay exactly to zero at the boundaries. Lapped biorthogonal transform (LBT) [47, 48] which nearly eliminate the blocking artifacts is based on a few modifications of the original LOT computations. LBT synthesis basis functions decay to zero at the boundaries and this is why blocking artifacts are almost eliminated. The LTs are based on DCT for which fast implementation algorithms are available. The LT coefficients when used directly in the JPEG [59] framework, outperforms the DCT based JPEG with almost no blocking artifacts [47]. In image compression applications, LTs [45–48] have shown better results compared to discrete cosine transforms (DCT) both subjectively and objectively. LTs can be rearranged into octave or dyadic like representation [18, 19, 49, 64]. LTs divide the frequency band into equally spaced M bands in contrast to the dyadic or octave based wavelet representation. The LOT or LBT coefficients can be rearranged into dyadic or octave like structure with $\log_2 M$ decomposition levels, where M is a power of 2 and is usually taken to be either 8 or 16. In [49], Malvar applied zero tree quantizer [70] on LT coefficients rearranged in octave-based form and has shown results comparable to state of the art wavelet based Set Partitioning in

Hierarchical Trees (SPIHT) algorithm [70]. Author also demonstrated that the LT (used in [49]) has much lower computational complexity as compared to the fastest possible implementation of the "9/7" wavelet transform via lifting. Tran et al. [79] has shown that well designed LTs when used in dyadic rearranged form are able to outperform the wavelet transform based methods for natural image compression when used in embedded zero tree (EZW) framework. The LOT and the LBT can be efficiently computed using the flowgraphs discussed in [45] and [47] respectively.

Recently, some methods on image denoising based on LT have been reported [18, 19, 64, 85]. The motivation for image denoising in LT domain is that the LT has good energy compaction and is orthogonal, hence the signal and noise statistics can be modeled efficiently in the same domain. Some important features of LTs which make it a suitable domain for efficient image processing are

- Good energy compaction
- Robustness to oversmoothing
- Sharper frequency attenuation properties of the M filters (possibly reducing aliasing throughout the subbands)
- The dyadic remapping property of LT coefficients
- Low computational complexity compared to discrete wavelet transforms.

The earlier works on LT based image denoising have observed that the LT coefficients in different subbands obtained after rearranging into octave-like representation have statistics similar to wavelet coefficients. A few models like non Gaussian Bivariate model, Gaussian mixture and Laplacian mixture models were used for modeling the rearranged orthogonal LT coefficients in subbands. The previous LT based image denoising schemes have shown encouraging results as compared to wavelet transform based methods. It was observed that the LT based schemes are very good in preserving the oscillatory patterns like textures as compared to wavelet transform based methods. However, in literature [18, 19, 64, 85], we find that the authors have assumed certain distribution for the LT coefficients and applied the assumed pdf in image denoising.

1.1 Motivation and Problem Definition

It is observed in the previous section that image modeling can be efficiently done in LT domain and can be used in various image processing applications. The LT domain image processing applications

[18,19,49,64,85] show comparable performance when compared to wavelet transform based schemes. However, we notice that so far no definitive study has been performed on the statistical modeling of LT coefficients, Further results on the applications of LTs in various image processing applications is also very limited. The thesis addresses the following problems:

1. The block LOT and LBT coefficients performs better than block DCT in image coding when used in the JPEG like framework with significantly reduced blocking artifacts. We observe that there is no exhaustive study regarding the determination of appropriate statistical distribution which best approximates the statistics of block LOT and LBT coefficients. In contrast, considerable work has been reported pertaining to study the statistical distributions of 2D block DCT coefficients for images [11,20,36,54,66] and recently Bhaskaranand and Gibson [5] have studied the statistical distribution of 3D DCT coefficients for video. In this thesis an extensive study is carried out to find a suitable statistical distribution which best approximates the block LOT and LBT coefficients. The knowledge of the statistical distribution of LT coefficients helps in design of optimal quantizers that may help in achieving optimal coding efficiency.

2. From last section we can see that, through dyadic remapping of LT coefficients, encouraging results can be achieved for various image processing applications. Though, the dyadic remapping property of LT coefficients is viewed as an very important feature of LTs, we find that no exhaustive study has been performed to determine the most suitable statistical distribution which best models the statistics of rearranged LT coefficients in subbands. An extensive study of the performance of Gaussian and several non Gaussian pdfs in modeling the subband LT coefficients is performed in this thesis. Such studies are very important in developing more efficient algorithms to perform several tasks like image compression, denoising, deblocking etc.

3. The LT based image denoising schemes have shown good results when compared to wavelet based image denoising schemes because of sharper frequency attenuation properties of the M filters (reducing aliasing throughout the subbands). Very few image denoising schemes have been reported in LT domain and the performance of LT domain image denoising has not been systematically evaluated for different statistical models. This thesis examines the performance of image denoising in LT domain for various efficient statistical models.

4. In various image deblocking algorithms reported in literature, iterative methods [34,57,86–88] have shown very good objective and subjective results. The problem with the iterative schemes is that they are computationally expensive. The wavelet domain image deblocking schemes [30,

42, 81, 83] have shown good results and show competitive performance with iterative schemes. The main problem with wavelet based methods is that they often oversmooths the textural patterns present in images while smoothing the block discontinuities. In this thesis, we propose to solve the image deblocking problem in LT domain that is known for its good performance in preserving textures. The nice denoising property of LTs is utilized to smooth out the blocking artifacts in LT domain.

1.2 Thesis Contributions

Main contributions of this thesis are summarized as follows:

1. Based on Kolomogrov Smirnov (KS) and Chi-square goodness of fit (GOF) [67] test, an appropriate probability density function (pdf) is proposed which best models the block LOT and LBT coefficients. An extensive comparative study is carried out on the performance of Gaussian, Laplacian, Gamma and Generalized Gaussian distributions in modeling the block LT coefficients. The goodness of fit test carried out on large number of different test images shows that no single distribution can be used to model the distributions of all AC coefficients for natural images. However the distribution of a majority of the significant AC coefficients can be modeled by Generalized Gaussian distribution.

2. Based on KS goodness of fit test, an extensive study on the performance of Gaussian, Laplacian, Gamma, Generalized Gaussian and Symmetric Normal Inverse Gaussian pdfs in modeling the subband rearranged LOT coefficients is carried out. The experiments performed on a large number of different test images show that no single distribution can be used to model the subband rearranged LOT coefficients for natural images but the majority of the subband coefficients can be modeled by Generalized Gaussian distribution.

3. We propose three LT based image denoising algorithms based on three different statistical models.

    - Based on KS goodness of fit test, it was found that the Generalized Gaussian pdf best models the statistics of subband rearranged LOT coefficients. Based on this finding we propose a LOT based image denoising technique using a Bayesian estimator based on modeling the global distribution of the rearranged LOT coefficients using a Generalized Gaussian distribution. The proposed LT based image denoising scheme outperforms a

recent wavelet based scheme which uses a Bayesian estimator based on modeling the global distribution of wavelet coefficients using a SNIG distribution where SNIG distribution is shown as highly suitable prior for modeling the wavelet transform coefficients.

- The pdfs with local parameters can better exploit the local statistics and captures the intrascale dependencies of the subband LT coefficients. We observe that the average values of kurtosis and skewness for various subband LT coefficients for small local neighborhoods are close to 3 and 0 respectively. It may be noted that kurtosis of 3 and a skewness of 0 correspond to a Gaussian distribution. Assuming the local distribution of the coefficients to be iid Gaussian with zero mean and spatially varying variance, we extend the local Wiener filtering concept in orthogonal LT domain and next propose a efficient doubly local Wiener filtering framework in the same domain. Local Wiener filtering in LT domain outperforms the local Wiener filtering in wavelet domain for most of the test images in both objective and subjective measures. The results are encouraging for highly textured test images. The efficient doubly local Wiener filtering in LT domain outperforms many well known wavelet based image denoising techniques.
- The encouraging performance of local Wiener filtering in LT domain motivated us to model the rearranged LT coefficients in a subband using Laplace pdf with local variance. A *maximum a posteriori* (MAP) estimator using the Laplace pdf with local variance is proposed for the estimation of noise free lapped transform coefficients. Experimental results show that the proposed low complexity image denoising method outperforms several wavelet based image denoising techniques and also outperforms the previous results on LT based image denoising schemes.

4. The non iterative wavelet based image deblocking schemes have shown good results as compared to iterative schemes in literature. The wavelet based schemes often oversmooths the textural information present in the images while smoothing the block discontinuities. Motivated by the encouraging denoising performance of LTs, we proposed two non iterative image deblocking schemes. The nice denoising ability of orthogonal LT is used to smooth the block discontinuities in LT domain.

    - A low complexity LT domain image deblocking scheme is proposed which is based on soft thresholding of LT coefficients. We demonstrate that the 'optimal' measured threshold has a strong relationship with the JPEG image *Quality factor* (Q_f) and also with the

average of first 3x3 values from the quantization table used in compression. The proposed global threshold is adaptive to the image *Quality factor* (Q_f) and the quantization table specified by the coder. The proposed algorithm shows good objective and subjective improvement over the blocky image. The proposed algorithm outperforms several well-known deblocking methods.

- A two stage blocking and ringing artifacts removal algorithm is proposed based on combined LT and adaptive bilateral filtering. The first stage reduces the blocking artifacts in LT domain using the local Wiener filtering concept and the second stage reduces the ringing artifacts using a adaptive bilateral filter. The first stage filter uses local variance in LT domain for pixel adaptive processing. The parameters of the proposed adaptive bilateral filter are chosen based on an empirical study. The proposed image deblocking and deringing algorithm shows comparable results when compared to one well known state of the art image deblocking algorithm both in terms of PSNR and SSIM index [80] results. The proposed algorithm also outperforms several well known image deblocking schemes.

1.3 Thesis Organization

The organization of the thesis is outlined as follows:

Chapter 2: This chapter reviews the concept of LOT and LBT. The description on octave or dyadic like representation of LT coefficients is next discussed.

Chapter 3: Based on Kolomogrov Smirnov (KS) and Chi-square goodness of fit test an extensive study on the determination of appropriate statistical distribution that best fits the block LOT and LBT coefficients is presented in this chapter. The detailed study using KS goodness of fit test on the performance of Gaussian and several non Gaussian pdfs in modeling the subband LT coefficients obtained after remapping of block LT coefficients is next described in the chapter. Detailed experimental results are presented to validate the findings.

Chapter 4: A brief review of the previous works on various wavelet domain image denoising techniques is presented in this chapter. Then the proposed image denoising algorithms in orthogonal LT domain based on three different efficient statistical models is described. Detailed experimental results are presented and are compared with various well known image denoising techniques.

Chapter 5: A brief review of the previous works on various image deblocking techniques is provided in this chapter. Next, two LT domain image deblocking algorithms are described. The

detailed experimental results are presented and are compared with several well known wavelet and non wavelet based image deblocking algorithms which validates the efficiency of the proposed scheme.

Chapter 6: Conclusions from the research work and the scope for future research are discussed.

Chapter 2

Lapped Transforms

The discrete cosine transform (DCT) [1] is a popular transform used in many image, video and audio coding applications because its performance is close to that of the Karhunen-Loeve transform (KLT) which is known to be optimal in the mean square error sense [33]. The block DCT has been used in many image/video coding standards like JPEG, H.261 and MPEG [4, 32, 59].

Reeve et al. [65] proposed two approaches to reduce the blocking artifacts. In the first approach, the blocks overlap by a small amount and the redundant information for the samples in the block boundaries is transmitted. In the decoder, the reconstructed samples from the neighborhood blocks are averaged in the overlapping areas. The main problem of the overlapping approach is that the bit rate increases because of increase in the total number of samples to be processed. In the second approach low pass filtering is applied to the pixels at the block boundaries. The filtering based approach is a postprocessing approach to reduce the blocking artifacts. This approach blurs the edges and textures at the block boundaries.

Cassereau [9] introduced a new class of transforms known as the Lapped Orthogonal Transforms (LOT) which lead to reduced blocking artifacts without increasing the bit rate. In this chapter, we begin with an introduction to traditional orthogonal block transforms, then the concepts of Lapped Orthogonal Transform (LOT) and Lapped Biorthogonal Transform (LBT) are reviewed. We also discuss the wavelet structure (octave like representation) of LOT and LBT and its applications to image coding and image denoising.

2.1 Traditional Orthogonal Block Transforms

In applications like image and speech coding, when traditional block transforms are used, the signal is divided into N non overlapping blocks of M samples where each block is independently transformed

and coded.

Let z be the original input vector of length MN samples, then the corresponding transformed vector y is given by

$$y = Tz \tag{2.1}$$

where T is a (MN) x (MN) block diagonal matrix of the form

$$T = \begin{pmatrix} D & 0 & 0 & .... & 0 \\ 0 & D & 0 & .... & 0 \\ . & & . & & . \\ . & & . & & . \\ 0 & .... & 0 & D & 0 \\ 0 & ... & 0 & 0 & D \end{pmatrix} \tag{2.2}$$

where D is a matrix of order N, whose columns are the basis functions that define the transform of each block.

2.2 Lapped Orthogonal Transform (LOT)

In Lapped Orthogonal Transform [45], the size of the input signal is twice that of the output signal

$$L = 2M \tag{2.3}$$

where M is the output signal length and L is the input signal length. Here, the neighboring blocks overlaps by $(L-M)$ samples. The basic idea of LOT is somewhat similar to the overlapping approach of [65] with an important difference: the LOT outputs M transform coefficients for an input of L samples of each block. Since the output signal length is equal to the block size, there is no increase

in the bit rate unlike in [65]. The transform matrix for LOT is given by

$$T = \begin{pmatrix} P_1 & 0 & 0 & .... & 0 \\ 0 & P_0 & 0 & .... & 0 \\ . & & . & & . \\ . & & . & & . \\ 0 & .... & 0 & P_0 & 0 \\ 0 & ... & 0 & 0 & P_2 \end{pmatrix} \tag{2.4}$$

where P_0 (of size LxM) defines the LOT basis functions. For a block with M samples, the LOT bases will have length of *2M*. The LOT for the first and the last blocks of a segment are tackled in a slightly different manner to ensure that none of the basis functions extend beyond the segment boundaries.

To ensure the orthogonality of the basis functions within a block, the following condition must be satisfied:

$$P_0' P_0 = I \tag{2.5}$$

where I is an identity matrix and to ensure the orthogonality in the overlapping regions, the basis functions of the adjacent blocks must satisfy the following condition:

$$P_0' S P_0 = P_0' S' P_0 = 0 \tag{2.6}$$

where S is a shift operator given by [45]

$$S = \begin{pmatrix} 0 & I \\ 0 & 0 \end{pmatrix} \tag{2.7}$$

The I matrix in (2.7) is of MxM size. In [9], optimal LOT was obtained using iterative optimization method which searches for the maximum *transform coding gain* G_{TC} [45], where at every step new basis functions are obtained. The main problem with this approach is that it is highly sensitive to numerical errors.

The *transform coding gain* or *energy compaction measure* is given by [45]

$$G_{TC} = \frac{\frac{1}{M}\sum_{i=1}^{M}\sigma_i^2}{\left[\prod_{i=1}^{M}\sigma_i^2\right]^{\frac{1}{M}}} \tag{2.8}$$

where σ_i^2 is the variance of the i^{th} diagonal entry of the matrix

$$R_0 = P_0' R_{xx} P_0 \tag{2.9}$$

Here R_{xx} is the signal covariance matrix [45] and is given by

$$R_{xx} = \begin{pmatrix} 1 & \rho & \rho^2 & .... & \rho^L \\ \rho & 1 & \rho & .... & \rho^{L-1} \\ . & & . & & . \\ . & & . & & . \\ \rho^{L-1} & .... & \rho & 1 & \rho \\ \rho^L & ... & \rho^2 & \rho & 1 \end{pmatrix} \tag{2.10}$$

Malvar et al. [45] derived an optimal LOT using an approach which is insensitive to numerical errors. They started with a *feasible* LOT matrix P (not necessarily optimal) defined as

$$P = \frac{1}{2}\begin{pmatrix} D_e - D_o & D_e - D_o \\ J(D_e - D_o) & -J(D_e - D_o) \end{pmatrix} \tag{2.11}$$

where D_e and D_o are the M x M/2 matrices containing the even and the odd DCT functions respectively and J is the *counter identity* matrix:

$$J = \begin{pmatrix} 0 & 0 & .... & 0 & 1 \\ 0 & 0 & .... & 1 & 0 \\ . & & . & & . \\ . & & . & & . \\ 0 & 1 & .... & 0 & 0 \\ 1 & 0 & ... & 0 & 0 \end{pmatrix} \tag{2.12}$$

The optimal LOT matrix is given by

$$P_0 = PZ \tag{2.13}$$

where Z is an orthogonal matrix. To obtain an optimal LOT, we need to find an optimal Z in (2.13).

Substituting (2.13) into (2.9), we have

$$R_0 = Z'P'R_{xx}PZ \tag{2.14}$$

With P and R_{xx} fixed, the G_{TC} is maximized when R_0 is diagonal which implies that the columns of Z are the eigen vectors of $P'R_{xx}P$. The optimal LOT matrix P_0 can be obtained with such Z. The LOT basis functions decay nearly to zero at the boundaries as shown in Fig. 2.1 (for M=8, L=16) and Fig. 2.2 (for M=16, L=32 and illustrated for a subset of indices).

2.3 Lapped Biorthogonal Transform (LBT)

Although LOT can significantly reduce the blocking artifacts of images, some blocking artifacts are still visible as the LOT basis functions do not decay exactly to zero at the boundaries. In contrast the Lapped Biorthogonal Transform (LBT) [47, 48] bases decay to zero at the boundaries resulting in LBT exhibiting fewer blocking artifacts as compared to LOT. In LBT, the forward and inverse transform matrices P_f and P_i do not maintain the orthogonality conditions, but as a pair they still maintain the orthogonality constraint

$$P_f'P_i = I \tag{2.15}$$

and the lapped orthogonality condition

$$P_f'SP_i = I \tag{2.16}$$

where the shift operator S is given by [45]

$$S = \begin{pmatrix} 0 & I \\ 0 & 0 \end{pmatrix} \tag{2.17}$$

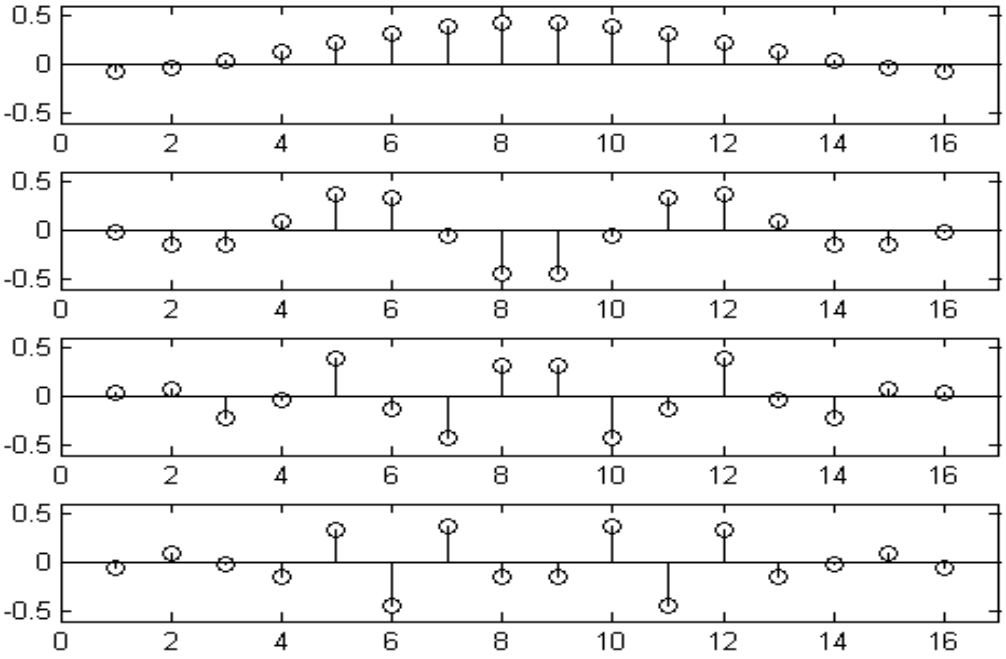

(a) Odd basis functions

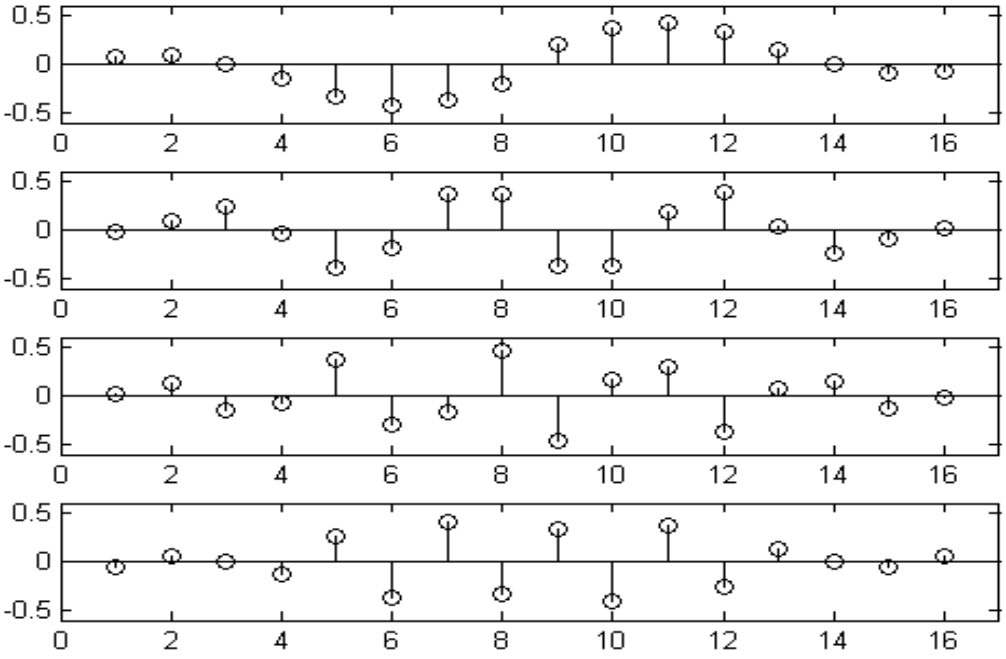

(b) Even basis functions

Fig. 2.1: An optimal LOT for M=8, L=16 and $\rho = 0.95$

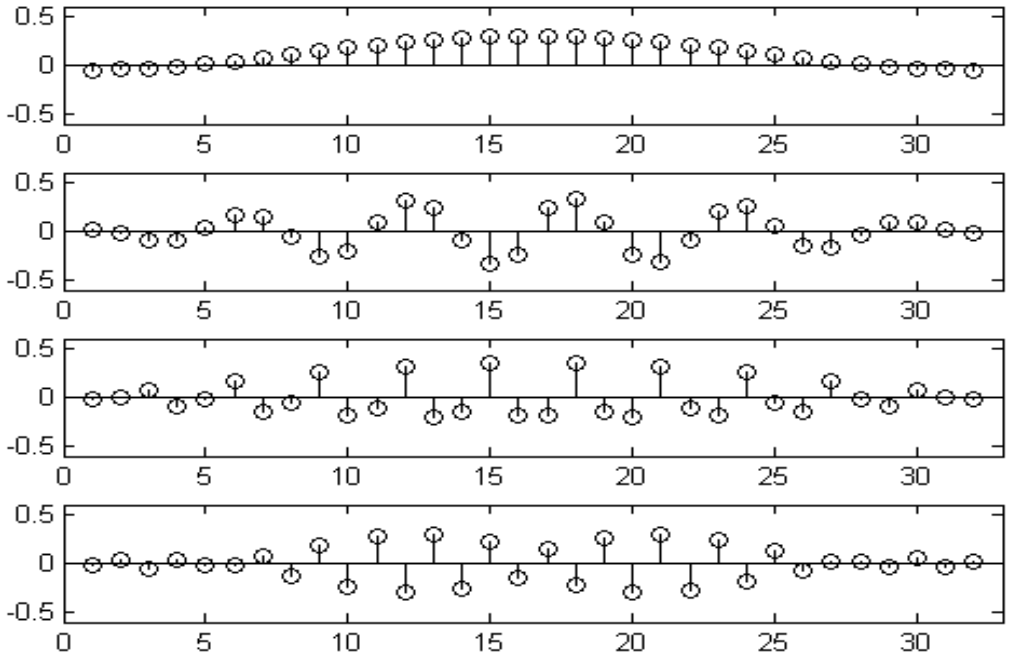

(a)

Fig. 2.2: A subset of basis functions of LOT for M = 16, L=32 (for indices 0, 5, 10 and 15)

The forward transform matrix T_f for LBT is given by

$$T_f = \begin{pmatrix} P_{f1} & 0 & 0 & .... & 0 \\ 0 & P_f & 0 & .... & 0 \\ . & & . & & . \\ . & & . & & . \\ 0 & .... & 0 & P_f & 0 \\ 0 & ... & 0 & 0 & P_{f2} \end{pmatrix} \tag{2.18}$$

where P_f (of size LxM) contains the LBT analysis basis functions. The inverse transform matrix T_i for LBT is given by

$$T_i = \begin{pmatrix} P_{i1} & 0 & 0 & .... & 0 \\ 0 & P_i & 0 & .... & 0 \\ . & & . & & . \\ . & & . & & . \\ 0 & .... & 0 & P_i & 0 \\ 0 & ... & 0 & 0 & P_{i2} \end{pmatrix} \tag{2.19}$$

where P_i (of size LxM) contains the LBT synthesis basis functions. In the forward and the inverse transformation process, the first and the last blocks are tackled in a slightly different manner to ensure that none of the basis functions extends beyond the segment boundaries.

The LBT can be obtained from LOT with a few modifications [47]. The first odd DCT functions are multiplied by $\sqrt{2}$ in the forward transformation and by $\frac{1}{\sqrt{2}}$ in the inverse transformation. The scaling matrix Y_f in forward transformation is given by

$$Y_f = \begin{pmatrix} \sqrt{2} & 0 & 0 & .... & 0 \\ 0 & 1 & 0 & .... & 0 \\ . & & . & & . \\ . & & . & & . \\ 0 & .... & 0 & 1 & 0 \\ 0 & ... & 0 & 0 & 1 \end{pmatrix} \tag{2.20}$$

and the scaling matrix Y_i in the inverse transformation is given by

$$Y_i = \begin{pmatrix} \frac{1}{\sqrt{2}} & 0 & 0 & .... & 0 \\ 0 & 1 & 0 & .... & 0 \\ . & & . & & . \\ . & & . & & . \\ 0 & .... & 0 & 1 & 0 \\ 0 & ... & 0 & 0 & 1 \end{pmatrix} \tag{2.21}$$

The LBT analysis matrix is given by

$$P_f = \frac{1}{2} \begin{pmatrix} D_e - Y_f D_0 & D_e - Y_f D_0 \\ J(D_e - Y_f D_0) & -J(D_e - Y_f D_0) \end{pmatrix} \tag{2.22}$$

while the synthesis matrix is given by

$$P_i = \frac{1}{2} \begin{pmatrix} D_e - Y_i D_0 & D_e - Y_i D_0 \\ J(D_e - Y_i D_0) & -J(D_e - Y_i D_0) \end{pmatrix} \tag{2.23}$$

The basis functions of the LBT (M=8) for synthesis and analysis are shown in Fig. 2.3 and Fig. 2.4 respectively. A subset of basis functions of LBT for M=16 are shown in Fig. 2.5 for illustration. It

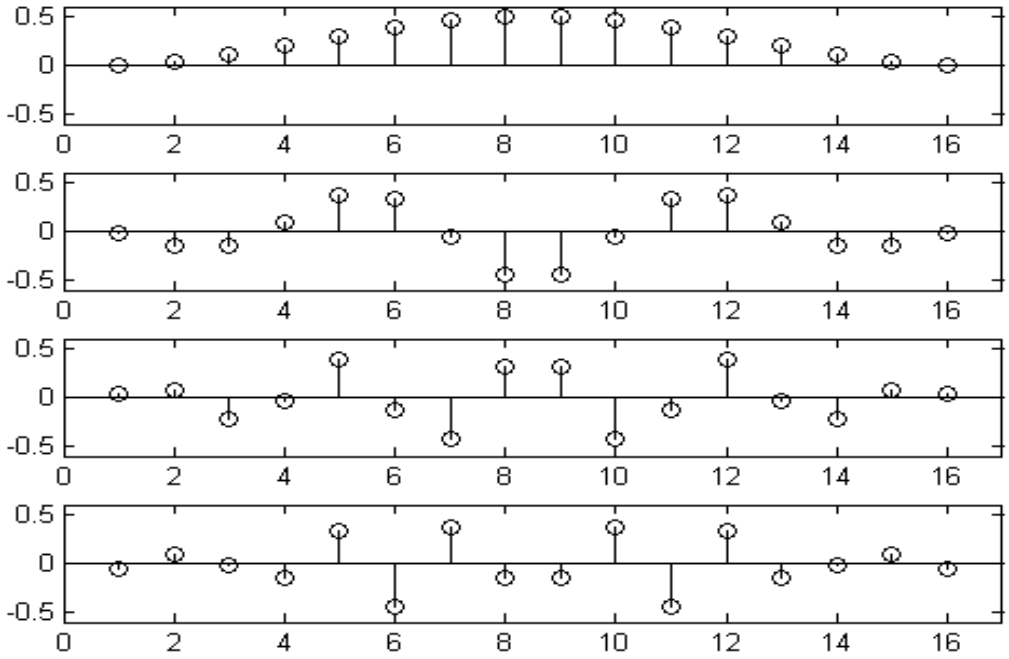

(a) Odd basis functions

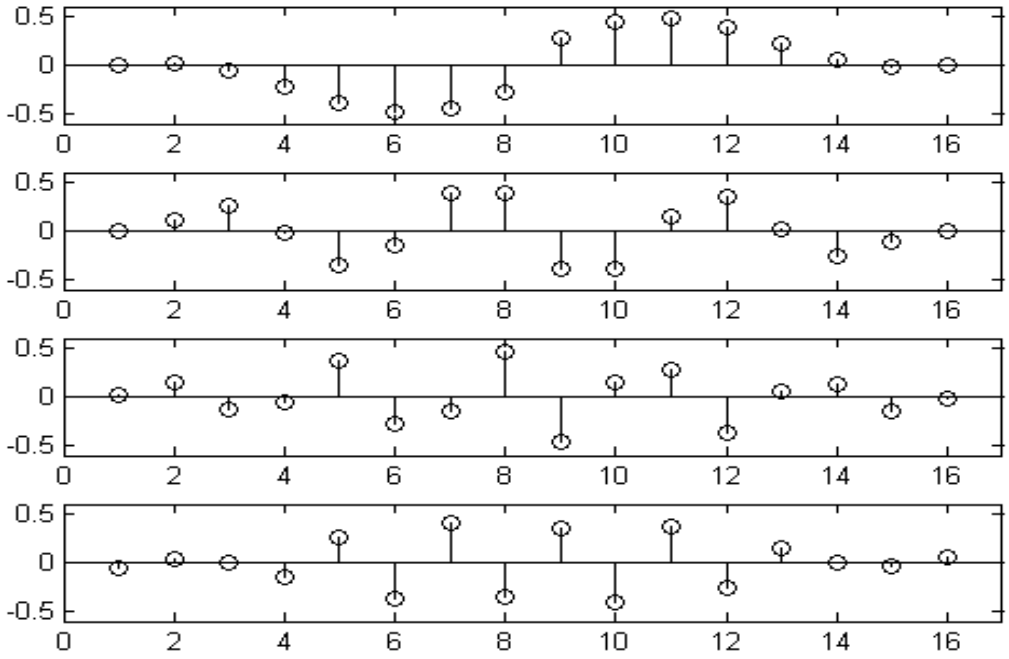

(b) Even basis functions

Fig. 2.3: Synthesis basis functions of an LBT for M=8, L=16 and $\rho = 0.95$

may be noted that the LBT synthesis basis functions decay to zero at the boundaries. This is the reason why LBT exhibits lesser blocking artifacts as compared to LOT. Though the LBT analysis

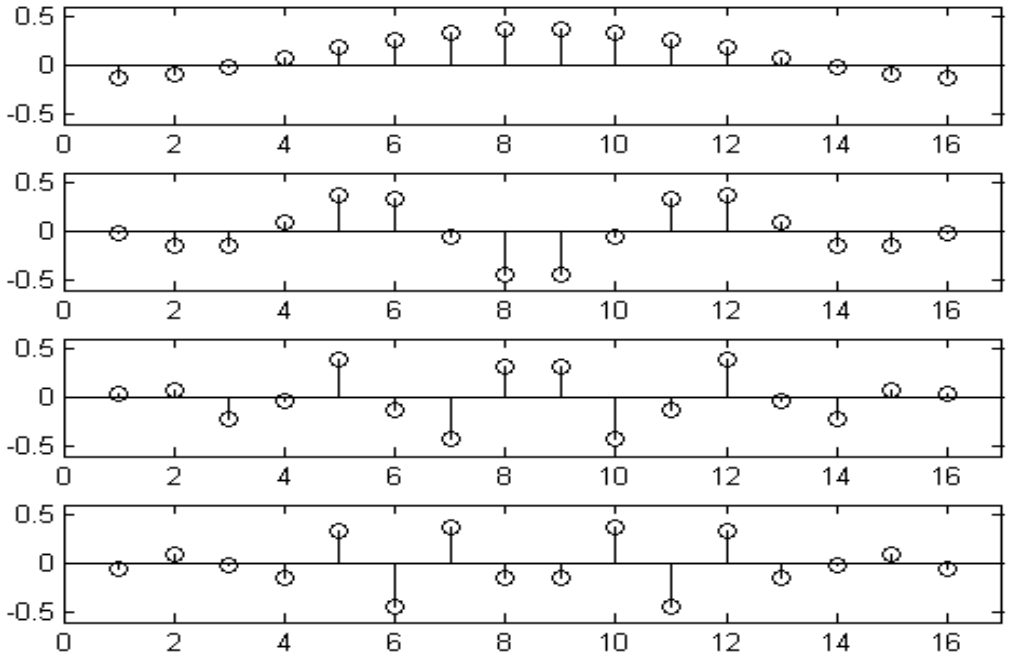

(a) Odd basis functions

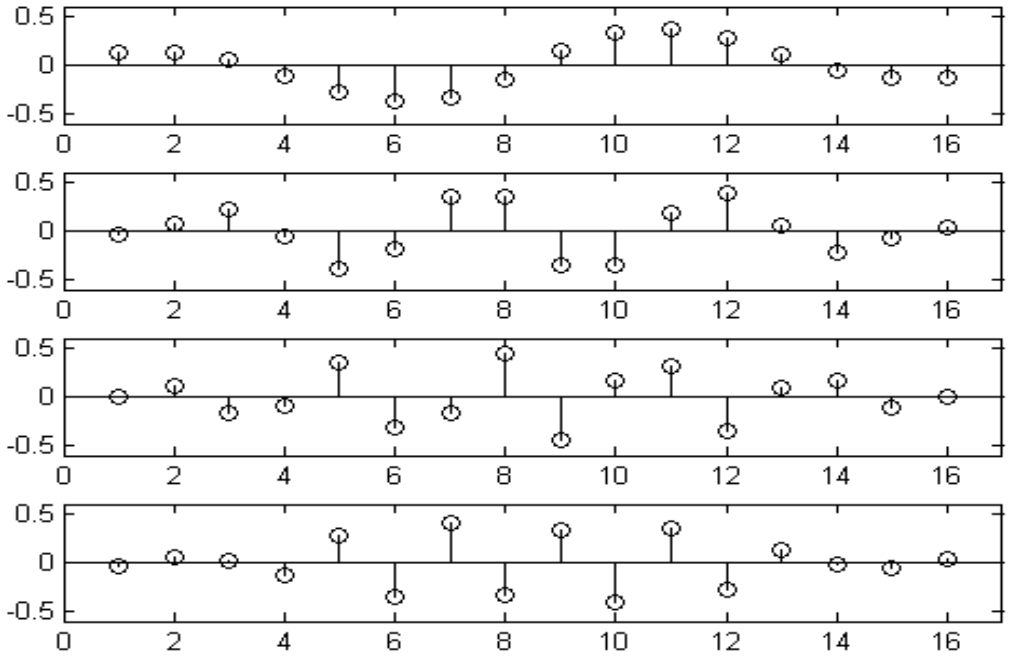

(b) Even basis functions

Fig. 2.4: Analysis basis functions of an LBT for M=8, L=16 and $\rho = 0.95$

basis functions have comparatively larger non zero values at the boundaries, these do not contribute to the blocking artifacts. The LBT has higher coding gain and has almost the same computational

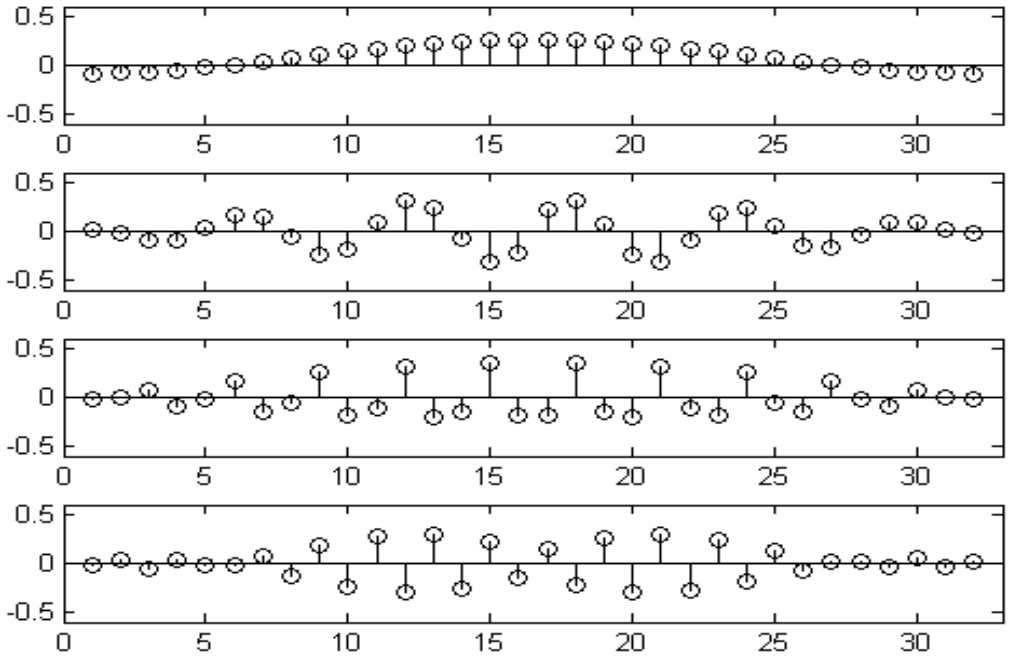

(a) LBT, analysis

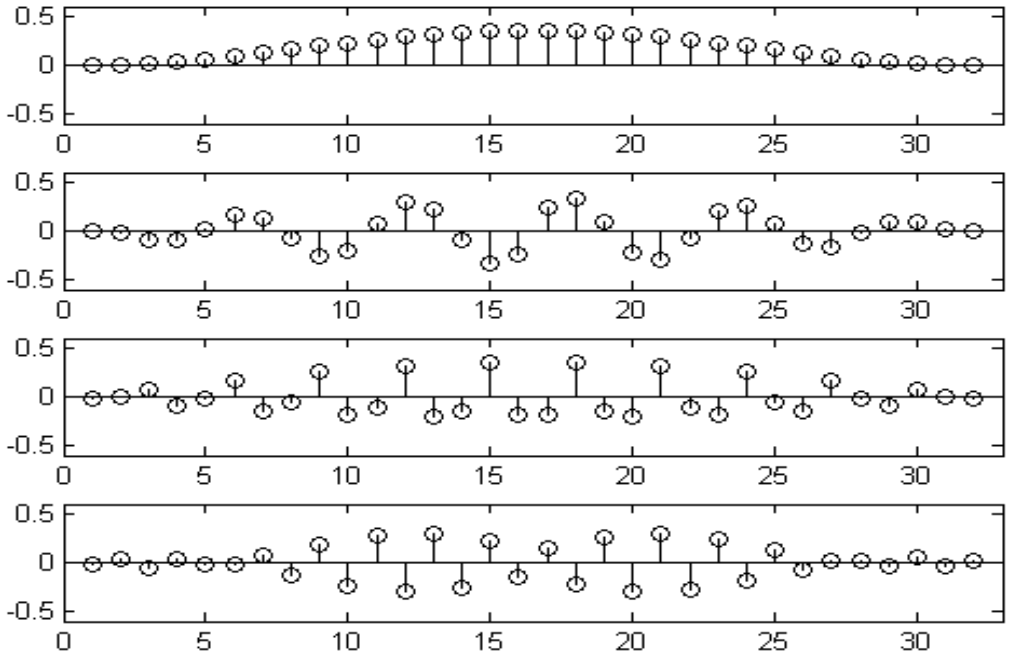

(b) LBT, synthesis

Fig. 2.5: A subset of basis functions of LBT for M = 16, L=32 for indices 0, 5, 10, and 15

complexity as LOT. The LBT computation flowgraph can be obtained from the LOT computation flowgraph by slight modifications as discussed in [47].

2.4 Wavelet Like Structure (Octave Like Representation) of LOT and LBT

The discrete wavelet transform (DWT) decomposes image into a set of bandpass filtered subimages. DWT decomposes the image into various subbands of various resolutions. This decomposition process can be viewed as very similar to the basis function decomposition in DCT. Basically the DWT and DCT provide a localized frequency representation of the original image. The way the output data are organized is different in the two cases. DCT when applied to 2x2 non overlapping blocks of an image results in four DCT coefficients in each DCT transformed blocks as shown in Fig.2.6(a). The four DCT coefficients are labeled as DCT_0 (which indicates the lowest frequency) to DCT_3 (which indicates the highest frequency). The 2x2 DCT transformed image coefficients can be rearranged into a 1-level wavelet like structure (Octave like Representation) as shown in Fig. 2.6(b). The rearranged coefficients in the subbands shown in Fig. 2.6(b) have statistics similar to the wavelet coefficients and can be modeled in a similar way as in the wavelet coefficients [82]. Fig. 2.6(b) can be viewed as a single level discrete wavelet transform decomposition of an image with the detailed subband consisting of the highest frequency coefficients of each DCT transformed blocks. The block DCT (MxM block decomposition) coefficients can be rearranged into a wavelet like structure with

$$J_d = \log_2 M \tag{2.24}$$

decomposition levels. Fig. 2.7(b) shows the 8x8 block DCT decomposition for Barbara image and Fig. 2.7(c) shows the rearrangement of the coefficients into 3-level wavelet like structure. The wavelet like structure of DCT has been successfully used in the field of image compression and has shown encouraging results when compared to wavelet transform based schemes [82]. The basic idea in these algorithms is to rearrange the block DCT coefficients into a wavelet like structure and apply the efficient wavelet based compression algorithms. The embedded zero wavelet (EZW) coding [70, 73] is a very efficient scheme for encoding the wavelet transform coefficients because of its superior features like embedded bit stream, scalability and precise rate control. Similar to wavelet transform coefficients, the rearranged DCT coefficients also exhibit good intrascale and interscale dependencies. Embedded zero tree coding when applied to rearranged DCT coefficients shows results comparable to similar discrete wavelet transform based methods [70, 73].

The LBT or LOT coefficients can also be similarly rearranged into a J level wavelet like struc-

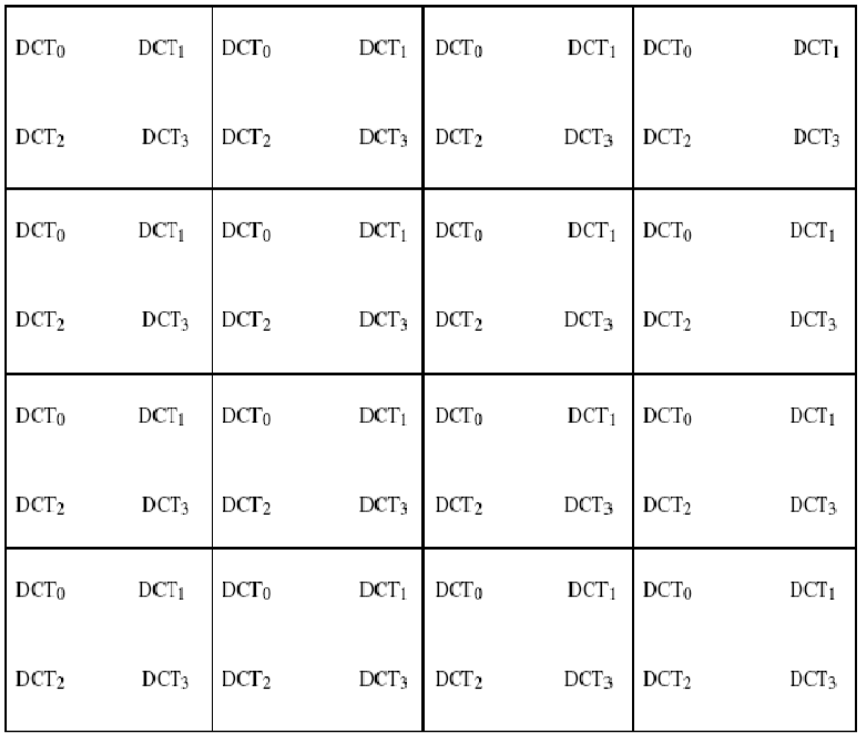

(a) DCT transformed image

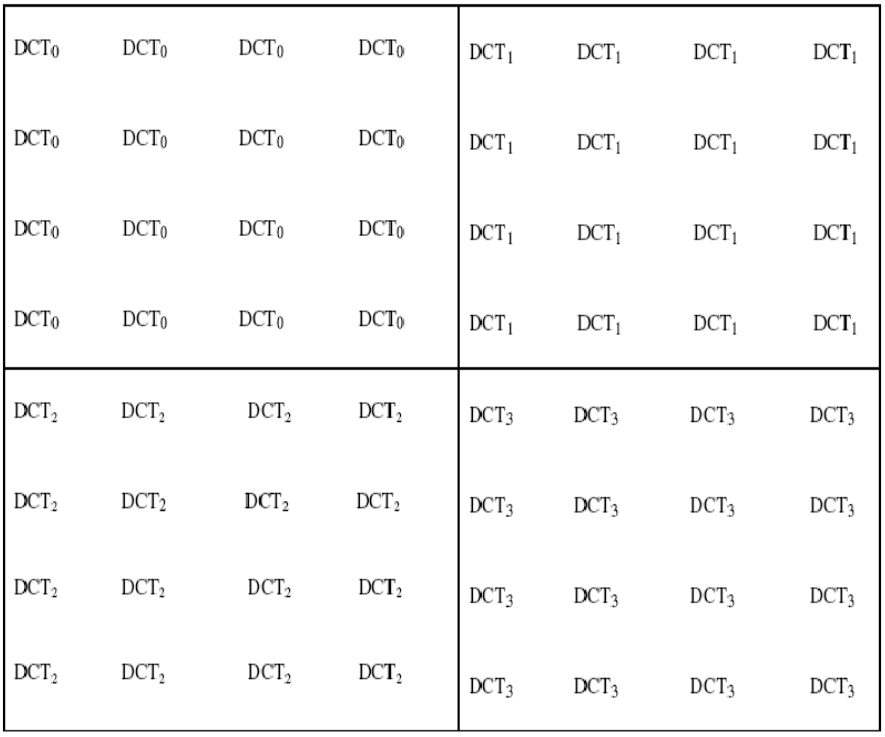

(b) Wavelet like structure (Octave like representation)

Fig. 2.6: Rearrangement of DCT coefficients into wavelet pyramid like structure

(a) Original image

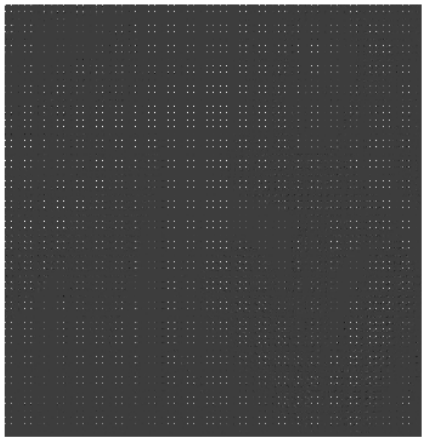

(b) DCT (8x8) block decomposition

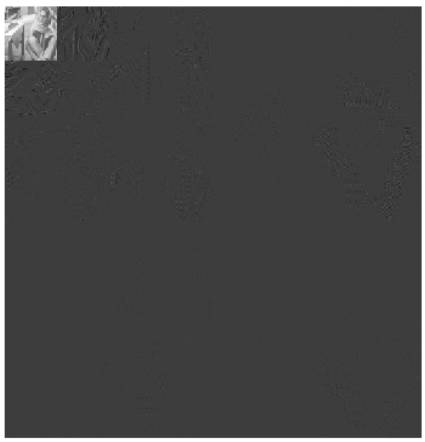

(c) Wavelet like structure (Octave like representation)

Fig. 2.7: Rearrangement of block DCT (8x8) coefficients into 3 level wavelet pyramid like structure

ture. The rearranged LOT or LBT coefficients exhibit strong intrascale and interscale dependencies as in the case of discrete wavelet transform coefficients. The efficient embedded zero tree coding when applied to rearranged LBT or LOT coefficients performs better than the DCT based zero tree coding technique [82] and shows performance comparable to similar discrete wavelet transform based techniques.

Recently, a few approaches on lapped transform based image denoising [18, 19, 64, 85] have been proposed exploiting the octave-like representation of LT coefficients. The motivation for image denoising in lapped transform [45,46] domain is that lapped transforms have good energy compaction and are robust to oversmoothing. The lapped transforms are orthogonal transforms, thus signal and noise statistics can be modeled precisely in the lapped transform domain.

Chapter 3

Statistical Distributions of Image Lapped Transform Coefficients

The lapped transforms (LT) [45–48] have been proposed as an alternative to the discrete cosine transform (DCT) with reduced blocking artifacts and better energy compaction. As discussed in the last chapter, the two important properties of LTs which lead to significant reduction of blocking artifacts are

- The basis functions are longer than the block size
- The basis functions decay to zero smoothly at the boundaries

The basis function of LOT decay nearly to zero at the boundaries which leads to considerable reduction in blocking artifacts, though not totaly eliminated. Since the LBT synthesis basis functions decay to zero at the boundaries, the blocking artifacts are almost eliminated in LBT. The LOT and LBT have almost the same computational complexity and LBT has higher coding gain compared to LOT and DCT. Higher coding gain provides lower reconstruction error energies. Successful application of an orthogonal transform in image compression, denoising or deblocking requires knowledge of the statistical distribution of the transform coefficients. However, till now, no exhaustive study has been reported on the distribution of lapped transform coefficients of images.

The LT coefficients can be rearranged into octave-like representation as discussed in Section 2.4 and this can be used efficiently with zero tree quantizers [49]. The rearranged orthogonal LT coefficients in octave form can also be used efficiently in image denoising applications [18, 19, 64, 85]. The octave like representation of orthogonal LT coefficients when used in image denoising applications has shown encouraging performance as compared to wavelet transform based schemes. The rearranged coefficients in different subbands show statistical behavior similar to that of wavelet coefficients.

In literature [18, 19, 64, 85], researchers have proposed different statistical models of rearranged orthogonal LT coefficients in subbands. However, no studies have been carried out to determine the appropriateness of different distributions in modeling the dyadic remapped LT coefficients.

In this chapter, we first study four different statistical distributions and identify the one that best approximates the statistics of the block LOT and LBT coefficients. We use Kolomogrov-Smirnov (KS) and Chi-square goodness of fit tests [67] to determine the statistical distribution that best fits the block LOT and LBT coefficients. Next we make an extensive study on the performance of Gaussian and several non Gaussian pdf's in modeling the rearranged orthogonal LT coefficients in different subbands.

This chapter is organized as follows: In Section 3.1, we discuss previous work on statistical distributions of DCT coefficients (a block transform) followed by our study on statistical distributions of block LOT and LBT coefficients in Section 3.2. The experimental results regarding the study on statistical distributions of block LOT and LBT coefficients are provided in the same section. In Section 3.3, we consider modeling of rearranged orthogonal LT coefficients in different subbands followed by experimental results.

3.1 Previous Study on Statistical Distributions of DCT Coefficients

DCT [1] based transform coding is very popular in image, video and speech compression. The DCT has good energy compaction and decorrelating properties. However, at low bit rates, the reconstructed images generally suffer from visually annoying blocking artifacts as a result of coarse quantization. Lapped transform [45] was proposed as an alternative to the DCT with reduced blocking artifacts and increased coding gain. Lapped transforms have basis functions that are longer than the block size and decay smoothly to zero at their boundaries. Lapped transforms are popular for their good performance, robustness against oversmoothing and availability of fast implementation algorithms. However there is no definitive study reported in the literature regarding the statistical distributions of block LOT and LBT coefficients.

In contrast, there is a large body of studies in the literature dealing with the distributions of 2-D DCT coefficients of natural images [11, 20, 54, 66]. Rieninger et al. [66] study the statistical distribution of the 2D DCT coefficients considering Gaussian, Laplacian, Gamma and Rayleigh distributions as probable models. Based on the Kolomogrov-Smirnov (KS) goodness of fit test they found that the statistics of the DC coefficients are best approximated by a Gaussian distribution while the non

DC coefficients are best approximated by the Laplacian distribution. Through some mathematical analysis, Lam and Goodman [49] proved that 2D DCT coefficients are better modeled by the Laplacian distribution. Eggerton et al. [20] concluded that no particular density function can be used for each of the coefficients but Laplacian fits the majority of the coefficients. They also found that when all the coefficients are lumped into one density function, the Cauchy distribution provides the best fit. Muller [54], found that the Generalized Gaussian distribution best approximates the statistics of the 2D DCT coefficients. In [36], Joshi and Fischer compared the performance of Generalized Gaussian and Laplacian models when applied to image coding; the authors concluded that the more complex Generalized Gaussian model does not give significant advantage over the Laplacian model. In [11], Chang et al. concluded that the Generalized Gamma distribution best models the statistics of the 2D DCT coefficients. Smoot and Reeve [76] study the statistics of the DCT coefficients of the differential signal obtained after motion estimation. They observe that the statistics are best approximated by the Laplacian distribution. Bellifemine et al. [3] demonstrate that the DCT coefficients of the differential signal obtained after motion estimation are best approximated by the Laplacian distribution. Recently, Malavika et al. [5] studied the statistics of 3D DCT coefficients for video, considering Gaussian, Laplacian, Double Gamma and Rayleigh distributions as probable models and concluded that no single distribution can be used to model the distributions of all the coefficients for different video sequences; however Gamma distribution fits the majority of the significant AC coefficients while the DC coefficients can be well approximated by Gaussian distribution.

3.2 Statistical Distributions of Block LOT and LBT Coefficients

In this section, we study the statistical distribution that best approximates the block LOT and LBT coefficients. We use Kolomogrov-Smirnov (KS) and Chi-square goodness of fit tests considering Gaussian, Laplacian, Gamma and Generalized Gaussian distributions as probable models as these distributions are commonly used for statistical modeling of DCT coefficients [5, 20, 54, 66].

3.2.1 Kolomogrov - Smirnov (KS) Goodness of Fit Tests

Kolomogrov-Smirnov test [67] is one of the popular goodness of fit test used in [5, 20, 66, 76] for determination of distributions of DCT coefficients of an image or video. The KS goodness of fit test statistic is a distance measure between the empirical cumulative distribution function (CDF) for a

given data set and the given model cumulative distribution function. For a given sample data set

$$X = \{x_1, x_2, ..., x_T\} \tag{3.1}$$

having the order statistics $x_{(s)}, s = 1, 2.....T$, the empirical cumulative distribution function is given as

$$\tilde{F}_X(x) = \begin{cases} 0, x < x_{(1)} \\ 1, x \geq x_{(T)} \\ \frac{s}{T}, x_{(s)} \leq x < x_{(s+1)}, s = 1, 2....., T-1 \end{cases} \tag{3.2}$$

The KS goodness of fit test statistic is given as

$$KS_{stat} = \max_{j=1,2,.....,T} \left| F_X(x_{(j)}) - \tilde{F}_X(x_{(j)}) \right| \tag{3.3}$$

When testing several distributions against the sample data, the one that gives the smallest KS statistic KS_{stat} is considered to be the best fit for the data.

3.2.2 Chi-Square Goodness of Fit Tests

Chi-square test [67] is also one of the widely used goodness of fit test [3,5,11,54] for determination of distributions of DCT coefficients of an image or video. The Chi-square goodness of fit test compares the model probability density functions with the empirical data and finds out the distortion by the following equation

$$\chi^2 = \sum_{i=1}^{k_d} \frac{(O_i - E_i)^2}{E_i} \tag{3.4}$$

where the range of data is partitioned into k_d disjoint and exhaustive bins B_i, i=1,2,3,.....k_d. $E_i = n_c p_i$ is the expected frequency in bin B_i where $p_i = P(x \in B_i)$ and O_i is the observed frequency in bin B_i. n_c is the total number of data samples. The model probability density function which gives the minimum chi-square value can be considered as the best fit.

3.2.3 Probability Distributions

In the KS and the Chi-square goodness of fit tests, Gaussian, Laplacian, Gamma and Generalized Gaussian distributions were considered. The parameters of all the distributions were found using the maximum likelihood (ML) method [37].

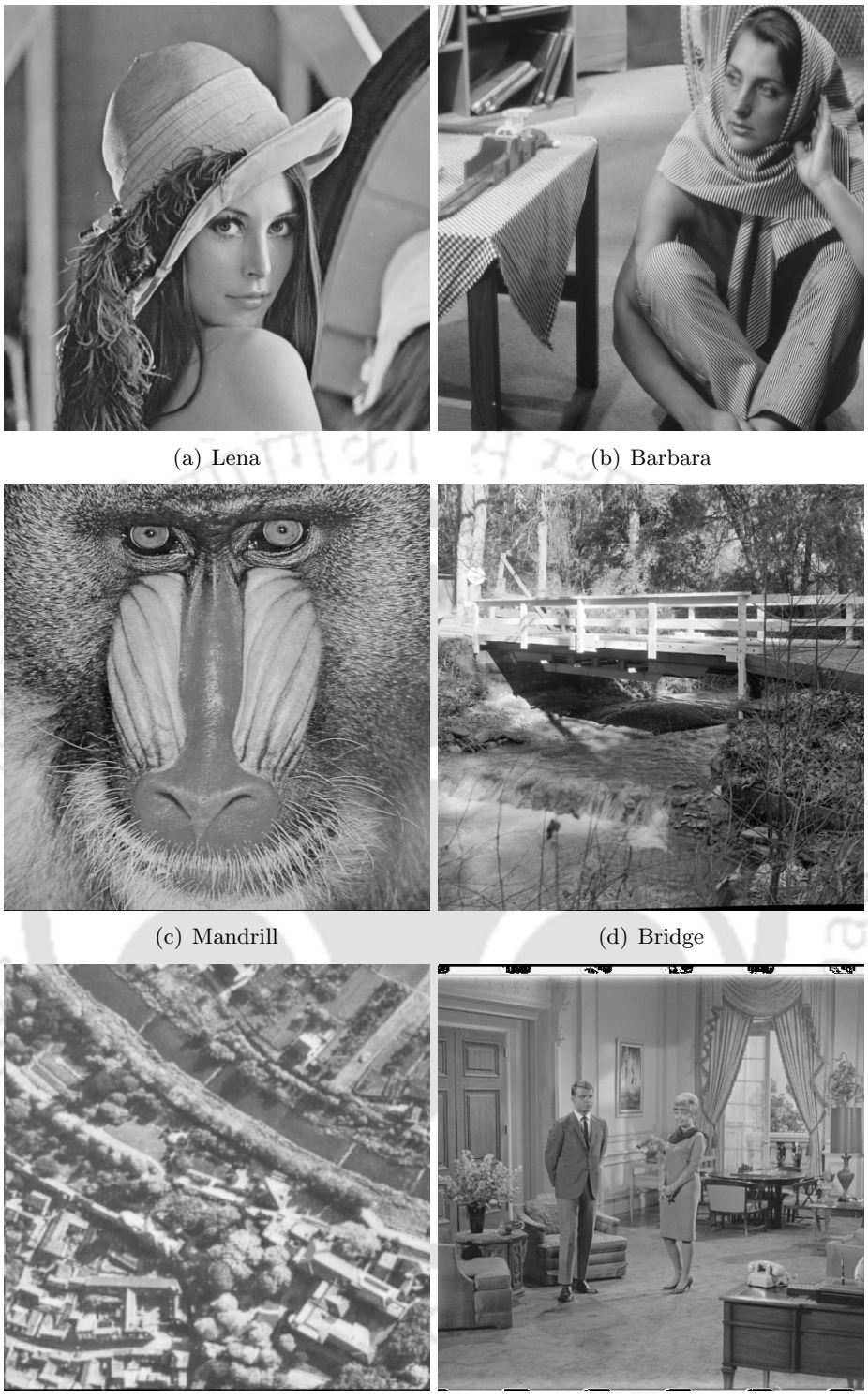

(a) Lena (b) Barbara

(c) Mandrill (d) Bridge

(e) Aerial (f) Couple

Fig. 3.1: Test images used in KS test

Gaussian probability density function

The Gaussian probability density function is given by

$$f_X(x) = \frac{1}{\sqrt{2\pi}\sigma} \exp\left(-\frac{(x-\mu)^2}{2\sigma^2}\right) \tag{3.5}$$

where μ is the mean and σ^2 is the variance. The ML estimates of μ and σ^2 are given by

$$\widehat{\mu} = \frac{1}{n}\sum_{i=1}^{n} x_i \tag{3.6}$$

$$\widehat{\sigma}^2 = \frac{1}{n}\sum_{i=1}^{n} (x_i - \widehat{\mu})^2 \tag{3.7}$$

Laplacian probability density function

The Laplacian probability density function is given by

$$f_X(x) = \frac{1}{2b}\exp\left(\frac{-|x-\mu|}{b}\right) \tag{3.8}$$

where μ is the mean and b is the scale parameter. The variance is given by $2b^2$. The ML estimate of the parameter b is given by

$$\widehat{b} = \frac{1}{N}\sum_{i=1}^{N} |x_i - \widehat{\mu}| \tag{3.9}$$

where $\widehat{\mu}$ is estimated using (3.6).

Gamma probability density function

The Gamma probability density function [35] is given by

$$f_X(x) = \frac{\sqrt[4]{3}}{\sqrt{8\pi\sigma\,|x-\mu|}}\exp\left(\frac{-\sqrt{3}\,|x-\mu|}{2\sigma}\right) \tag{3.10}$$

The parameters μ and σ are estimated using (3.6) and (3.7).

Generalized Gaussian probability density function

The Generalized Gaussian probability density function [44] is given by

$$f_X(x) = \frac{\beta}{2\alpha\Gamma\left(\frac{1}{\beta}\right)}\exp -\left(\frac{|x-\mu|}{\alpha}\right)^{\beta} \tag{3.11}$$

where $\Gamma(.)$ is the Gamma function given by

$$\Gamma(z) = \int_0^\infty e^{-t} t^{z-1} dt, z > 0 \tag{3.12}$$

and α, β respectively are known as the scale parameter and the shape parameter. For the special cases $\beta = 2$ or $\beta = 1$, the generalized Gaussian pdf becomes a Gaussian or a Laplacian pdf respectively. The ML estimation of the parameters α and β can be obtained as follows: The shape parameter $\widehat{\beta}$ is the solution of the equation

$$1 + \frac{\psi\left(\frac{1}{\beta}\right)}{\beta} - \frac{\sum_{i=1}^{N} |x_i|^\beta \log |x_i|}{\sum |x_i|^\beta} + \frac{\log\left(\frac{\beta}{N}\sum_{i=1}^{N} |x_i|^\beta\right)}{\beta} = 0 \tag{3.13}$$

where $\psi(.)$ is the digamma function given by

$$\psi(z) = \frac{\Gamma'(z)}{\Gamma(z)} \tag{3.14}$$

The ML estimate of α (for known ML estimate $\widehat{\beta}$) is given by

$$\widehat{\alpha} = \left(\frac{\widehat{\beta}}{N}\sum_{i=1}^{N} |x_i|^{\widehat{\beta}}\right)^{\frac{1}{\widehat{\beta}}} \tag{3.15}$$

where N is number of observations. The $\widehat{\beta}$ is determined using the Newton Raphson iterative procedure [37] with the initial guess from the moment based method described in Section 3.3.1. Experimental results indicates that only 3-4 iteration steps are required to compute the solutions within an accuracy of 10^{-6}.

In Table 3.1, the estimated shape parameter $\widehat{\beta}$ of M=8 LOT coefficients for different test images are shown. Table 3.2, shows $\widehat{\beta}$ values of M=8 LBT coefficients for the same images. In Table 3.1 and 3.2, we can see that ML estimates of β are considerably different from 1 in most of the cases. For the Mandrill and the Bridge images, the statistics for a few coefficients is likely to be Laplacian (β=1). Further it may be observed that within a given image the estimated shape parameter values of different coefficients do not vary much.

Table. 3.1: Estimated shape parameter $\widehat{\beta}$ of LOT (M=8) coefficients for different test images

	Lena	Barbara	Mandrill	Boat	Bridge	Couple
C_{10}	0.4583	0.5160	0.8329	0.5192	0.8495	0.4170
C_{11}	0.4148	0.4972	1.0039	0.5129	0.9812	0.4711
C_{01}	0.4574	0.5032	1.0553	0.4585	0.8654	0.5157
C_{20}	0.5678	0.5758	0.6934	0.5377	0.8856	0.5912
C_{02}	0.4927	0.5725	0.9316	0.4632	0.9025	0.4911
C_{12}	0.4363	0.4905	0.9139	0.5081	0.9345	0.4889
C_{21}	0.4680	0.5637	0.7568	0.5895	1.0562	0.5235
C_{03}	0.5746	0.5888	0.8918	0.4835	0.8572	0.4763
C_{30}	0.6747	0.7108	0.6918	0.6030	0.9673	0.5378

Table. 3.2: Estimated shape parameter $\widehat{\beta}$ of LBT (M=8) coefficients for different images

	Lena	Barbara	Mandrill	Boat	Bridge	Couple
C_{10}	0.4682	0.5466	0.8695	0.5165	0.8172	0.3889
C_{11}	0.4232	0.5341	1.0496	0.5014	1.0032	0.4596
C_{01}	0.4732	0.5450	1.0381	0.4734	0.8739	0.5374
C_{20}	0.6329	0.6040	0.6603	0.5585	0.8559	0.5892
C_{02}	0.5189	0.6038	0.9353	0.4750	0.9091	0.5043
C_{12}	0.4296	0.4983	0.9286	0.5007	0.9455	0.4918
C_{21}	0.4794	0.5922	0.7590	0.5791	1.0770	0.5229
C_{03}	0.5882	0.6962	0.9673	0.5130	0.8847	0.5163
C_{30}	0.5784	0.6874	0.7127	0.6213	0.9974	0.5287

3.2.4 Experimental Results

We use Lena, Barbara, Mandrill, Bridge, Aerial and Couple test images for experiments because these images contains variety of image details and textural informations. The KS and Chi-square goodness of fit performance was evaluated using 2D block LOT and 2D block LBT coefficients with M=8 and M=16 against the model distributions. The model distribution which provides the minimum KS statistic or Chi-square statistic is considered to be the best fit under the KS or Chi-square criterion. The nine AC coefficients C_{10}, C_{11}, C_{01}, C_{20}, C_{02}, C_{12}, C_{21}, C_{03} and C_{30} used in the experiments were chosen because they usually have the most effect on the image quality.

If N_1xN_2 is the size of the image after computation of 2D LOT or LBT, then each frequency coefficient will have (N_1/M)x(N_2/M) values for the image to be used in KS and Chi-square test. The KS statistic results for modeling of block LOT and LBT coefficients are shown in Fig. 3.2 - 3.5 in form of graphs where the X-axis is composed of six discrete points representing the six test images with bargraphs showing the KS statistic for the Gaussian, Laplacian, Gamma and Generalized Gaussian distributions. We consider the Gaussian and Gamma distributions with mean and variance equal to sample mean and sample variance. The Laplacian and Generalized Gaussian model parameters were

calculated using maximum likelihood method.

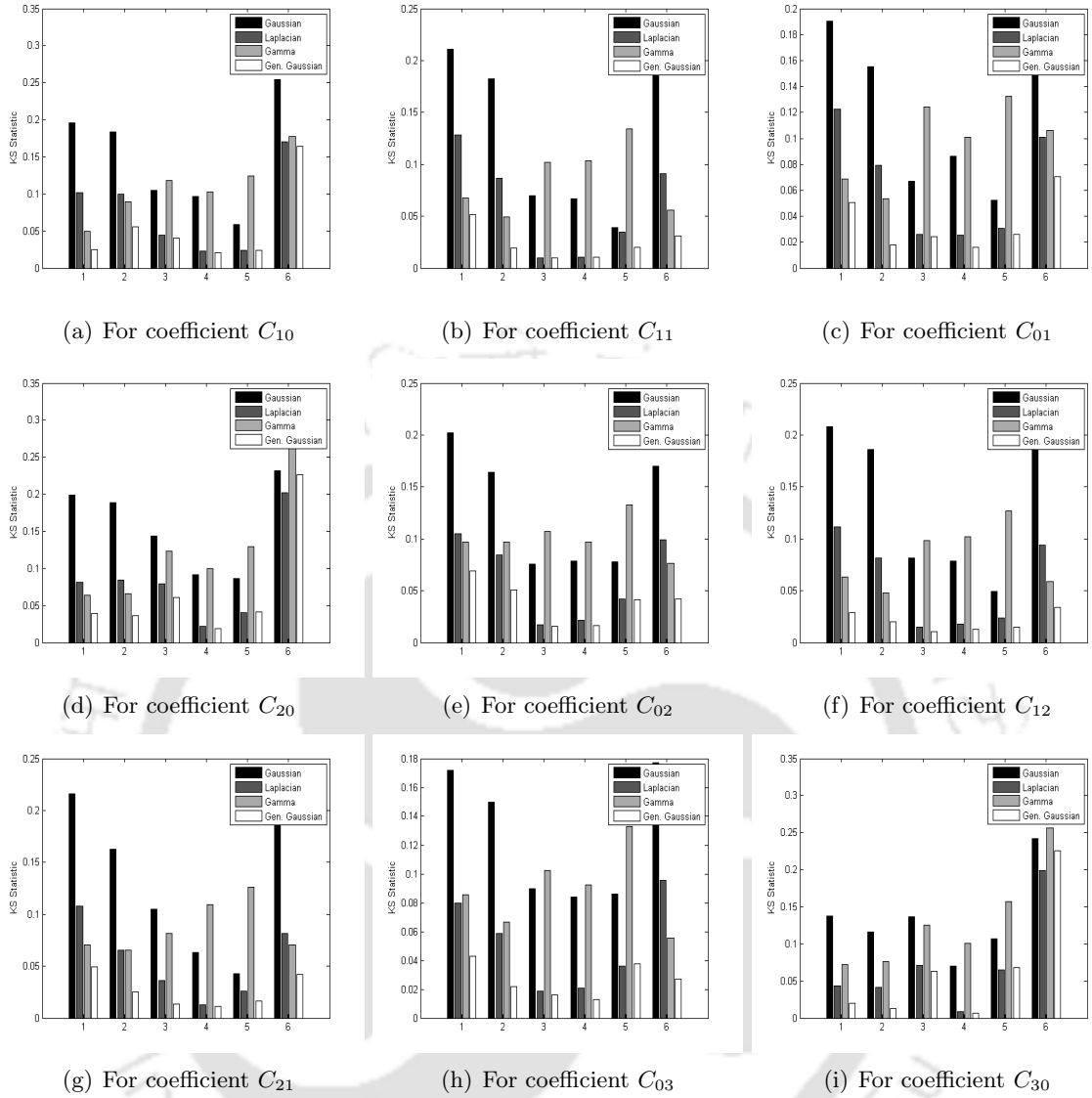

(a) For coefficient C_{10} (b) For coefficient C_{11} (c) For coefficient C_{01}

(d) For coefficient C_{20} (e) For coefficient C_{02} (f) For coefficient C_{12}

(g) For coefficient C_{21} (h) For coefficient C_{03} (i) For coefficient C_{30}

Fig. 3.2: KS test statistic for LOT (M=8) coefficients C_{10}, C_{11}, C_{01}, C_{20}, C_{02}, C_{12}, C_{21}, C_{03} and C_{30} (1=Lena, 2=Barbara, 3=Mandrill, 4=Bridge, 5=Aerial, 6=Couple)

KS test results

- **For LOT (M=8)**: In Fig. 3.2, coefficients C_{10}, C_{01}, C_{02}, C_{12} and C_{21} show the smallest KS statistic for the Generalized Gaussian distribution in all the tested images. Coefficient C_{11} also shows the smallest Generalized Gaussian KS statistic for most of the test images except for Mandrill and Bridge where Laplacian KS statistic is the smallest. For coefficient C_{20}, Laplacian KS statistic is the smallest only for Aerial and Couple images and for the rest Generalized Gaussian KS statistic is the smallest. For C_{03}, except for Aerial image where

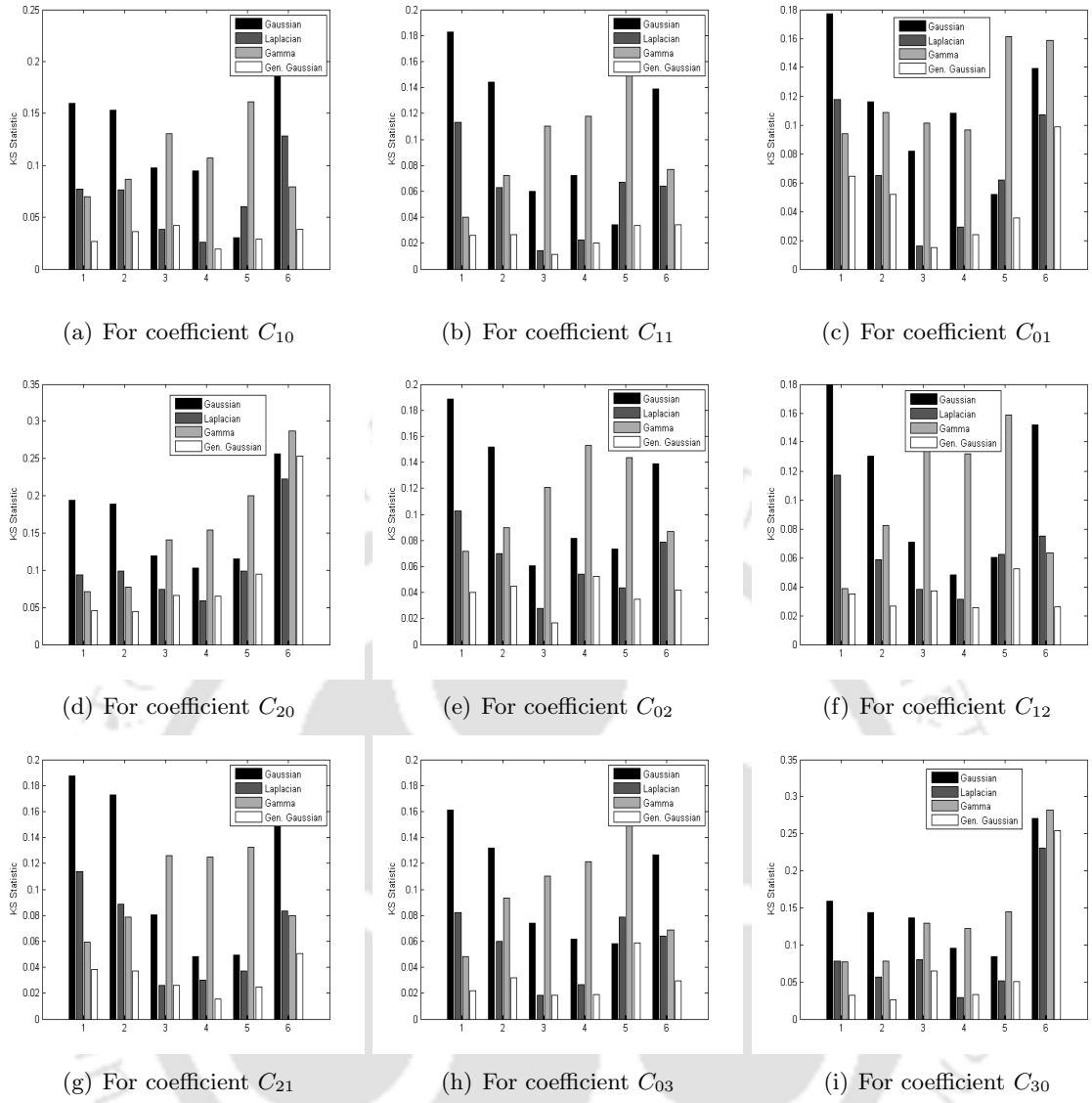

(a) For coefficient C_{10} (b) For coefficient C_{11} (c) For coefficient C_{01}

(d) For coefficient C_{20} (e) For coefficient C_{02} (f) For coefficient C_{12}

(g) For coefficient C_{21} (h) For coefficient C_{03} (i) For coefficient C_{30}

Fig. 3.3: KS test statistic for LOT (M=16) coefficients C_{10}, C_{11}, C_{01}, C_{20}, C_{02}, C_{12}, C_{21}, C_{03} and C_{30} (1=Lena, 2=Barbara, 3=Mandrill, 4=Bridge, 5=Aerial, 6=Couple)

Laplacian KS statistic is the smallest, for all others Generalized Gaussian KS statistic is the smallest. However for the coefficient C_{30}, except for Aerial and Couple, Generalized Gaussian KS statistic is the smallest.

- **For LOT (M=16)**: Coefficients C_{11}, C_{01}, C_{02} and C_{12} in Fig. 3.3 show the smallest Generalized Gaussian KS statistic for all the test images. Coefficient C_{10} shows Laplacian KS statistic as the minimum for Mandrill image and for the rest Generalized Gaussian KS statistic is the minimum. Coefficient C_{20} shows the minimum Laplacian KS statistic for Bridge and Couple images and for all others the Generalized Gaussian KS statistic is the minimum. For coefficient C_{21}, only the Mandrill image has the smallest Laplacian KS statistic. For coefficient C_{30},

the Bridge and Couple images show the smallest Laplacian KS statistic, and for other images Generalized Gaussian KS statistic is the smallest. For the Aerial image, coefficient C_{03} show the smallest KS statistic for Gaussian distribution and for the others Generalized Gaussian KS statistic is the smallest.

- **For LBT (M=8)**: Fig. 3.4 shows that Coefficients C_{10}, C_{01}, C_{12} and C_{21} have the smallest KS statistic for Generalized Gaussian distribution for all the test images. Coefficient C_{11} for the Mandrill image shows smallest KS statistic in the case of the Laplacian distribution and coefficient C_{20} for the Aerial and Couple images shows the minimum KS statistic for the Laplacian distribution and for the rest of the images the KS statistic is smallest for the Generalized Gaussian distribution. Coefficients C_{02} and C_{03} exhibit the smallest KS statistic for Laplacian distribution in case of Mandrill image and for the rest, KS statistic for Generalized Gaussian is the smallest. Coefficient C_{30} shows the smallest KS statistic in case of Laplacian for Bridge and Couple images and for all other images KS statistic for Generalized Gaussian is the minimum.

- **For LBT (M=16)**: Fig. 3.5 shows that for coefficients C_{02} and C_{21}, the KS statistic is minimum in case of the Generalized Gaussian for all test images. Coefficients C_{10}, C_{01} and C_{12} show the minimum KS statistic in case of the Laplacian distribution for Mandrill image and coefficient C_{30} also shows minimum KS statistic for the Laplacian distribution in case of Mandrill and Couple images. For all other images KS statistic for the Generalized Gaussian is the minimum. Coefficient C_{20} exhibits smallest KS statistic for the Laplacian distribution in case of Bridge and Couple images and for the rest KS statistic is minimum for the Generalized Gaussian distribution. However, coefficients C_{11} and C_{03} shows minimum KS statistic for the Gaussian distribution and for all other images the KS statistic for the Generalized Gaussian is the minimum.

Chi-Square test results

The results for Chi-square test are provided in Tables 3.3 - 3.26.

- **For LOT(M=8)**: Coefficients C_{10}, C_{11}, C_{01}, C_{20}, C_{21} and C_{03} for Lena image shows smallest χ^2 statistic for the Generalized Gaussian distribution among all the model distributions and coefficients C_{02}, C_{12} and C_{30} shows smallest χ^2 statistic for the Gamma distribution. For the

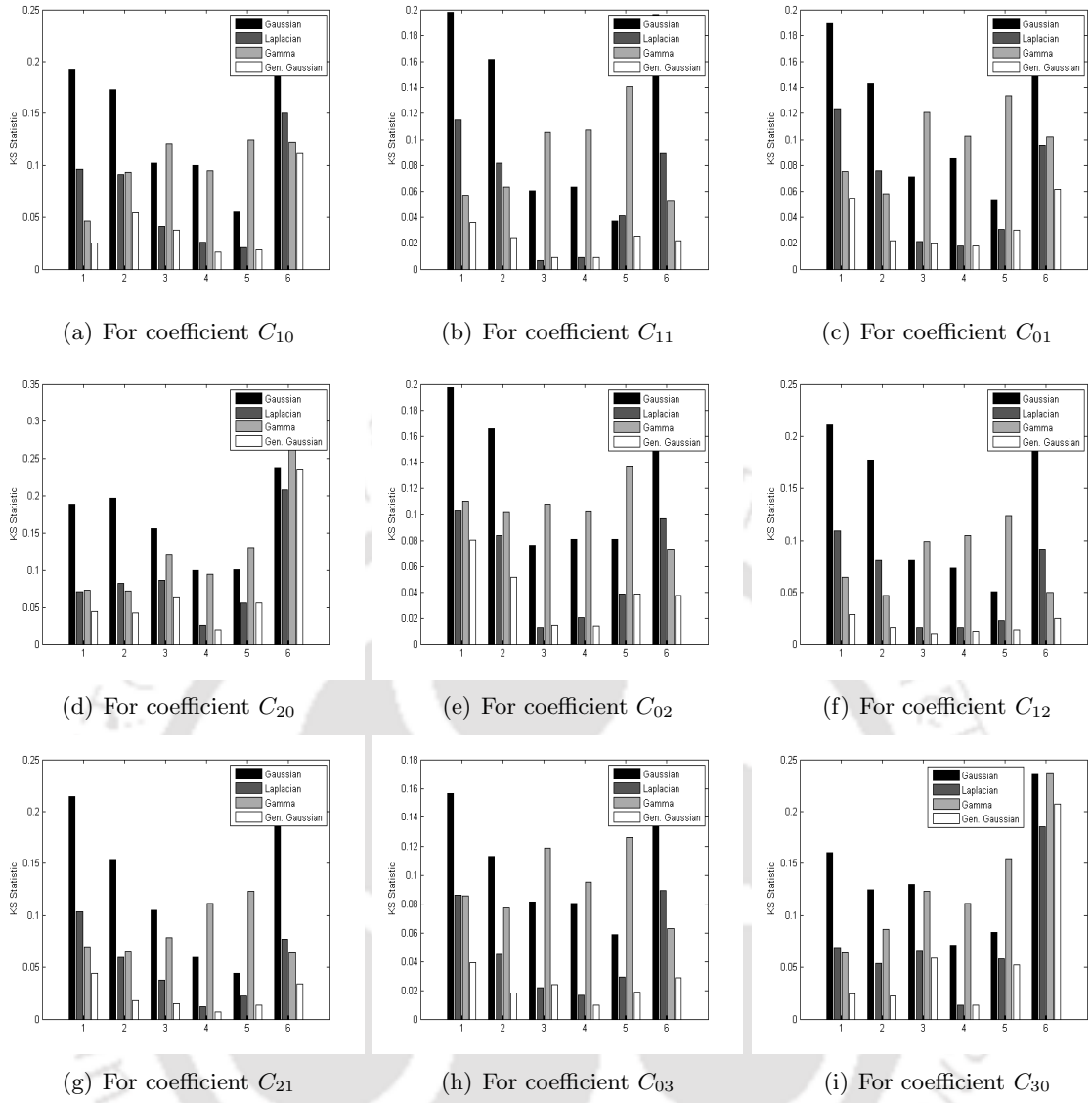

(a) For coefficient C_{10} (b) For coefficient C_{11} (c) For coefficient C_{01}

(d) For coefficient C_{20} (e) For coefficient C_{02} (f) For coefficient C_{12}

(g) For coefficient C_{21} (h) For coefficient C_{03} (i) For coefficient C_{30}

Fig. 3.4: KS test statistic for LBT (M=8) coefficients C_{10}, C_{11}, C_{01}, C_{20}, C_{02}, C_{12}, C_{21}, C_{03} and C_{30} (1=Lena, 2=Barbara, 3=Mandrill, 4=Bridge, 5=Aerial, 6=Couple)

Barbara image 8 of 9 distributions shows smallest χ^2 statistic for the Generalized Gaussian distribution and only coefficient C_{20} shows smallest χ^2 statistic for the Gamma distribution. For Mandrill image also 7 out of 9 coefficients show smallest χ^2 statistic for the Generalized Gaussian distribution and only coefficients C_{20} and C_{30} shows smallest χ^2 statistic for Gamma case. For Bridge image all the 9 tested coefficients show smallest χ^2 statistic for the Generalized Gaussian distribution. Aerial image shows smallest χ^2 statistic in case of the Generalized Gaussian distribution for 8 of 9 tested coefficients. Only coefficient C_{02} shows smallest χ^2 statistic for the Laplacian distribution among all the model distributions. However for the Couple image, 5 of 9 coefficients show smallest χ^2 statistic for the Gamma distribution and coefficient C_{01} shows smallest and same χ^2 statistic for the Generalized Gaussian and the Gamma distri-

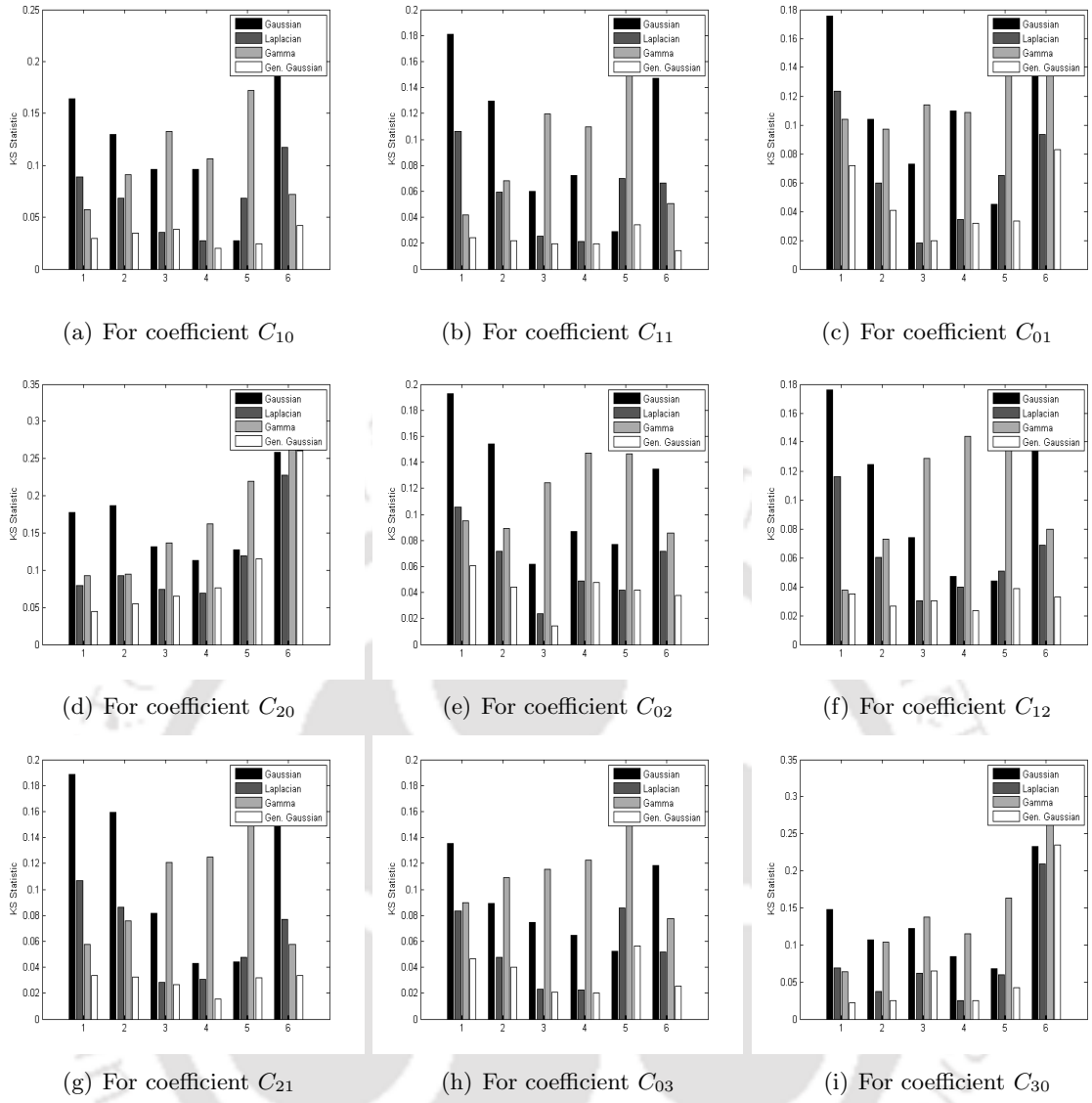

(a) For coefficient C_{10} (b) For coefficient C_{11} (c) For coefficient C_{01}

(d) For coefficient C_{20} (e) For coefficient C_{02} (f) For coefficient C_{12}

(g) For coefficient C_{21} (h) For coefficient C_{03} (i) For coefficient C_{30}

Fig. 3.5: KS test statistic for LBT (M=16) coefficients C_{10}, C_{11}, C_{01}, C_{20}, C_{02}, C_{12}, C_{21}, C_{03} and C_{30} (1=Lena, 2=Barbara, 3=Mandrill, 4=Bridge, 5=Aerial, 6=Couple)

butions. Coefficients C_{10}, C_{11} and C_{12} show smallest χ^2 statistic for the Generalized Gaussian distribution in case of Couple image.

- For **LOT (M=16)**: For Lena image, the coefficients C_{11}, C_{20}, C_{21}, C_{03} and C_{30} show smallest χ^2 statistic for the Generalized Gaussian distribution among all the model distributions. Coefficient C_{10} shows the smallest for Gamma and the Generalized Gaussian distributions. Coefficients C_{01}, C_{02} and C_{12} show smallest χ^2 statistic for the Gamma distribution. For Barbara image 8 of 9 coefficients show smallest χ^2 statistic for the Generalized Gaussian distribution and only C_{21} shows the smallest χ^2 statistic for Gamma distribution. Mandrill image shows minimum and the same χ^2 statistic for the Laplacian and Generalized Gaussian distributions in

case of coefficients C_{11}, C_{21} and C_{03}. Coefficients C_{12} and C_{30} shows minimum χ^2 statistic for the Laplacian and Gamma distributions respectively. Coefficients C_{10}, C_{01}, C_{20} and C_{02} show minimum χ^2 statistic for the Generalized Gaussian distribution in case of Mandrill image. For Bridge image, the 6 of 9 coefficients show minimum χ^2 statistic for the Generalized Gaussian distribution and the coefficient C_{02} shows minimum and same χ^2 statistic for the Laplacian and Generalized Gaussian distribution. Only coefficients C_{11} and C_{12} show minimum χ^2 statistic for the Laplacian case. For Aerial image, 6 of 9 coefficients exhibit smallest χ^2 statistic for the Generalized Gaussian distribution. Coefficients C_{10} and C_{12} shows the minimum and equal χ^2 statistic for the Gaussian and Generalized Gaussian distributions and for the Laplacian and Generalized Gaussian distributions respectively. Only coefficient C_{20} shows minimum χ^2 statistic in case of the Laplacian for Aerial image. 7 of 9 coefficients for the Couple image show smallest χ^2 statistic for the Generalized Gaussian distribution and Coefficients C_{01} and C_{20} show smallest χ^2 statistic for the Gamma distribution.

- **For LBT (M=8)**: For Lena image, 7 of 9 coefficients show smallest χ^2 statistic for the Generalized Gaussian distribution among all the model distributions. Only coefficients C_{03} and C_{30} show smallest χ^2 statistic in case of the Gamma distribution among all the model distributions. For Barbara image, 6 of 9 tested coefficients show smallest χ^2 statistic for the Generalized Gaussian distribution among all the model distributions. Only coefficients C_{10}, C_{01} and C_{20} show smallest χ^2 statistic for the Gamma distributions among all the model distributions. Coefficients C_{10}, C_{11}, C_{20}, C_{02}, C_{12}, C_{21} and C_{03} for Mandrill image show smallest χ^2 statistic for the Generalized Gaussian distribution. Only coefficient C_{01} shows the smallest χ^2 statistic for the Laplacian case and the coefficient C_{30} shows the smallest χ^2 statistic for the Gamma distribution among all the model distributions. For Bridge image, 7 of 9 coefficients show smallest χ^2 statistic for the Generalized Gaussian case among all the model distributions. However coefficients C_{11} and C_{30} shows same χ^2 statistic for the Laplacian and Generalized Gaussian distributions which is minimum among all the model distributions. For Aerial image, 6 of 9 coefficients shows smallest χ^2 statistic for the Generalized Gaussian distribution among all the model distributions. Only coefficients C_{02}, C_{03} and C_{30} show smallest χ^2 statistic for the Laplacian case. For Couple image, 4 of 9 coefficients show smallest χ^2 statistic for the Generalized Gaussian case among all the model distributions and coefficient C_{03} shows the same χ^2 statistic for the Gamma and Generalized Gaussian case which is the smallest among all the model distributions. However coefficients C_{01}, C_{20}, C_{02} and C_{21} shows

smallest χ^2 statistic for the Gamma distribution for Couple image.

- **For LBT (M=16)**: Coefficients C_{10}, C_{11}, C_{01}, C_{20}, C_{02}, C_{12}, C_{03} and C_{30} for Lena image shows smallest χ^2 statistic for the Gamma distribution and coefficient C_{21} shows smallest χ^2 statistic for the Generalized Gaussian distribution among all the model distributions. Coefficients C_{10}, C_{11}, C_{01}, C_{20}, C_{02}, C_{12}, C_{03} and C_{30} for Barbara image show the smallest χ^2 statistic for the Generalized Gaussian distribution and coefficient C_{21} shows the smallest χ^2 statistic for the Gamma distribution among all the model distributions. For Mandrill image, coefficients C_{10}, C_{01}, C_{20}, C_{12}, C_{03} and C_{30} show the smallest χ^2 statistic for the Generalized Gaussian distribution among all the model distributions and coefficient C_{11} exhibits the smallest χ^2 statistic for the Laplacian distribution. Coefficients C_{02} and C_{21} shows smallest and same χ^2 statistic for the Laplacian and Generalized Gaussian distribution for Mandrill image. For Bridge image, coefficient C_{02} shows the smallest and the same χ^2 statistic for Laplacian and the Generalized Gaussian distribution. Coefficients C_{10}, C_{01}, C_{20}, C_{12}, C_{21} and C_{30} show smallest χ^2 statistic for the Generalized Gaussian distribution. Coefficients C_{11} and C_{03} show smallest χ^2 statistic for the Laplacian case for Bridge image. In Aerial image, the coefficients C_{11}, C_{01}, C_{21}, C_{03} and C_{30} show the smallest χ^2 statistic for the Generalized Gaussian distribution. Coefficient C_{10} shows the minimum and also same χ^2 statistic for the Gaussian and Generalized Gaussian distributions. Coefficients C_{20}, C_{02} and C_{12} show smallest χ^2 statistic for the Laplacian case. For Couple image, 6 of 9 coefficients show the smallest χ^2 statistic for the Generalized Gaussian distribution among all the model distributions. Only coefficients C_{11}, C_{01} and C_{20} shows smallest χ^2 statistic for the Gamma distribution.

The experimental results show that no single distribution provides the smallest KS and χ^2 statistic for all the tested AC coefficients of block LOT and LBT of different test images. The Generalized Gaussian distribution however provides the smallest KS and χ^2 statistic for the majority of the significant AC coefficients of the tested images. Fig. 3.6 - 3.9 shows the empirical pdf of the block LT coefficients along with the fitted Gaussian, Laplacian, Gamma and Generalized Gaussian pdfs. From Fig. 3.6 - 3.9 as well as from the values of the KS and Chi-square statistics, it is clear that the Generalized Gaussian distribution provides a better fit to the empirical distribution as compared to the Gaussian, Laplacian and Gamma distribution.

Table. 3.3: χ^2 statistics for a few block LOT (M=8) coefficients of Lena image.

	Gaussian	Laplacian	Gamma	Gen. Gaussian
C_{10}	1.77x10^7	5876	54	**15**
C_{11}	446713	2307	66	**15**
C_{01}	1856825	1578	25	**22**
C_{20}	3.53x10^{13}	107612	117	**44**
C_{02}	4.60x10^7	4518	**49**	53
C_{12}	4.42x10^7	8664	**11**	12
C_{21}	1.88x10^7	15356	66	**62**
C_{03}	2.63x10^6	1008	29	**8**
C_{30}	1.59x10^{12}	5617	**36**	44

Table. 3.4: χ^2 statistics for a few block LOT (M=8) coefficients of Barbara image.

	Gaussian	Laplacian	Gamma	Gen. Gaussian
C_{10}	2.62x10^5	1366	25	**7**
C_{11}	25526	1164	26	**4**
C_{01}	1645	365	10	**9**
C_{20}	2.98x10^7	5208	**34**	43
C_{02}	7798	343	10498	**20**
C_{12}	2.72x10^5	2740	65	**14**
C_{21}	4.78x10^6	1226	23	**4**
C_{03}	6.89x10^9	2742	20	**7**
C_{30}	1194	107	109	**5**

Table. 3.5: χ^2 statistics for a few block LOT (M=8) coefficients of Mandrill image.

	Gaussian	Laplacian	Gamma	Gen. Gaussian
C_{10}	15429	186	359	**79**
C_{11}	1470	6	529	**6**
C_{01}	2907	9	395	**16**
C_{20}	9.93x10^5	1205	**106**	121
C_{02}	53312	20	306	**10**
C_{12}	13243	21	231	**6**
C_{21}	2.90x10^5	55	152	**8**
C_{03}	1.85x10^7	64	100	**20**
C_{30}	87999	527	**38**	90

Table. 3.6: χ^2 statistics for a few block LOT (M=8) coefficients of Bridge image.

	Gaussian	Laplacian	Gamma	Gen. Gaussian
C_{10}	23879	140	237	**57**
C_{11}	10896	6	393	**5**
C_{01}	2.19x10^5	54	167	**12**
C_{20}	51332	88	241	**36**
C_{02}	1698	25	351	**20**
C_{12}	28458	17	325	**12**
C_{21}	2359	4	433	**3**
C_{03}	69320	29	201	**6**
C_{30}	1124	8	131	**7**

Table. 3.7: χ^2 statistics for a few block LOT (M=8) coefficients of Aerial image.

	Gaussian	Laplacian	Gamma	Gen. Gaussian
C_{10}	86	14	217	**8**
C_{11}	24	37	264	**9**
C_{01}	91	13	183	**11**
C_{20}	3.73x10^5	42	142	**34**
C_{02}	274	**11**	165	12
C_{12}	68	13	186	**5**
C_{21}	41	18	269	**3**
C_{03}	5838	20	124	**18**
C_{30}	2.21x10^6	194	201	**130**

Table. 3.8: χ^2 statistics for a few block LOT (M=8) coefficients of Couple image.

	Gaussian	Laplacian	Gamma	Gen. Gaussian
C_{10}	2.08x10^7	4.54x10^5	579	**375**
C_{11}	3.42x10^{13}	4.16x10^5	167	**30**
C_{01}	1.29x10^7	603	**6**	**6**
C_{20}	2.09x10^{11}	9.57x10^5	**680**	1065
C_{02}	7.46x10^6	409	**2**	24
C_{12}	9.31x$10^1$4	3.22x10^5	131	**20**
C_{21}	4750	1393	**2**	16
C_{03}	1.40x10^9	543	**10**	15
C_{30}	7.07x10^7	6667	**203**	221

Table. 3.9: χ^2 statistics for a few block LOT (M=16) coefficients of Lena image.

	Gaussian	Laplacian	Gamma	Gen. Gaussian
C_{10}	2.61x10^5	250	**7**	**7**
C_{11}	2436	396	58	**20**
C_{01}	1441	219	**19**	29
C_{20}	2.71x10^5	740	41	**33**
C_{02}	1.44x10^5	338	**7**	18
C_{12}	5.01x10^5	482	**19**	25
C_{21}	1.72x10^4	673	25	**7**
C_{03}	2270	226	12	**7**
C_{30}	2.29x10^8	493	11	**10**

Table. 3.10: χ^2 statistics for a few block LOT (M=16) coefficients of Barbara image.

	Gaussian	Laplacian	Gamma	Gen. Gaussian
C_{10}	2945	112	57	**18**
C_{11}	5512	45	31	**13**
C_{01}	410	58	29	**15**
C_{20}	2.13x10^7	993	31	**16**
C_{02}	2.86x10^7	416	12	**7**
C_{12}	4637	64	17	**15**
C_{21}	5.41x10^8	426	**11**	13
C_{03}	79491	92	15	**13**
C_{30}	1.27x10^{11}	1151	22	**13**

Table. 3.11: χ^2 statistics for a few block LOT (M=16) coefficients of Mandrill image.

	Gaussian	Laplacian	Gamma	Gen. Gaussian
C_{10}	38102	24	54	**15**
C_{11}	2804	**4**	129	**4**
C_{01}	7672	11	88	**7**
C_{20}	1054	66	77	**25**
C_{02}	92	6	152	**5**
C_{12}	1.39x10^6	**15**	55	16
C_{21}	124	**7**	86	**7**
C_{03}	354	**2**	108	**2**
C_{30}	1.31x10^4	203	**35**	38

Table. 3.12: χ^2 statistics for a few block LOT (M=16) coefficients of Bridge image.

	Gaussian	Laplacian	Gamma	Gen. Gaussian
C_{10}	2099	19	91	**12**
C_{11}	3.24x10^4	**18**	143	20
C_{01}	2.08x10^4	84	39	**15**
C_{20}	486	53	133	**43**
C_{02}	4152	**27**	166	**27**
C_{12}	295	**7**	122	9
C_{21}	51	14	267	**2**
C_{03}	247	5	179	**3**
C_{30}	1979	13	83	**7**

Table. 3.13: χ^2 statistics for a few block LOT (M=16) coefficients of Aerial image.

	Gaussian	Laplacian	Gamma	Gen. Gaussian
C_{10}	**10**	28	151	**10**
C_{11}	25	21	129	**15**
C_{01}	24	26	132	**18**
C_{20}	116	**35**	91	37
C_{02}	27	14	84	**12**
C_{12}	31	**14**	88	**14**
C_{21}	11	10	98	**4**
C_{03}	92	16	92	**12**
C_{30}	45	12	79	**11**

Table. 3.14: χ^2 statistics for a few block LOT (M=16) coefficients of Couple image

	Gaussian	Laplacian	Gamma	Gen. Gaussian
C_{10}	1.62x10^4	3955	153	**90**
C_{11}	7842	208	8	**7**
C_{01}	651	129	**17**	63
C_{20}	2.13x10^6	1.79x10^4	**308**	469
C_{02}	1048	74	42	**33**
C_{12}	1.86x10^8	188	15	**6**
C_{21}	8.96x10^9	27640	94	**50**
C_{03}	619	43	33	**21**
C_{30}	1.09x10^6	1.19x10^4	699	**652**

Table. 3.15: χ^2 statistics for a few block LBT (M=8) coefficients of Lena image.

	Gaussian	Laplacian	Gamma	Gen. Gaussian
C_{10}	1.65x10^9	9903	117	**47**
C_{11}	1.07x10^7	3252	78	**57**
C_{01}	5.34x10^7	1154	82	**70**
C_{20}	1.03x10^{13}	4.33x10^4	87	**61**
C_{02}	9.97x10^9	1.02x10^4	254	**158**
C_{12}	3.43x10^9	1.12x10^4	92	**42**
C_{21}	5.27x10^9	2.39x10^4	233	**100**
C_{03}	1.08x10^{11}	368	**28**	43
C_{30}	1.67x10^6	845	**48**	58

Table. 3.16: χ^2 statistics for a few block LBT (M=8) coefficients of Barbara image.

	Gaussian	Laplacian	Gamma	Gen. Gaussian
C_{10}	8.29x10^9	2133	**56**	66
C_{11}	1.30x10^6	726	26	**24**
C_{01}	1.21x10^4	464	**19**	37
C_{20}	5.76x10^{13}	1.87x10^5	**112**	129
C_{02}	1.19x10^9	861	276	**121**
C_{12}	2.31x10^{10}	7571	101	**26**
C_{21}	2.06x10^{12}	3938	131	**31**
C_{03}	2.41x10^{10}	382	86	**16**
C_{30}	1.15x10^4	174	55	**25**

Table. 3.17: χ^2 statistics for a few block LBT (M=8) coefficients of Mandrill image.

	Gaussian	Laplacian	Gamma	Gen. Gaussian
C_{10}	1.24x10^4	189	266	**104**
C_{11}	623	9	550	**7**
C_{01}	7919	**13**	404	17
C_{20}	1.27x10^7	3014	228	**163**
C_{02}	40131	29	275	**14**
C_{12}	7012	17	239	**5**
C_{21}	9.27x10^4	57	176	**10**
C_{03}	6.91x10^6	37	203	**27**
C_{30}	5.27x10^4	456	**52**	78

Table. 3.18: χ^2 statistics for a few block LBT (M=8) coefficients of Bridge image.

	Gaussian	Laplacian	Gamma	Gen. Gaussian
C_{10}	1.93x10^4	184	244	**53**
C_{11}	2.10x10^4	**9**	353	**9**
C_{01}	3.15x10^5	63	177	**14**
C_{20}	1.60x10^5	164	218	**63**
C_{02}	2287	25	372	**20**
C_{12}	9310	24	294	**19**
C_{21}	3392	6	474	**4**
C_{03}	6099	16	270	**3**
C_{30}	6312	**24**	507	**24**

Table. 3.19: χ^2 statistics for a few block LBT (M=8) coefficients of Aerial image.

	Gaussian	Laplacian	Gamma	Gen. Gaussian
C_{10}	69	22	249	**15**
C_{11}	20	48	306	**12**
C_{01}	57	18	259	**8**
C_{20}	1.84x10^6	88	131	**52**
C_{02}	586	**19**	180	20
C_{12}	100	10	201	**2**
C_{21}	42	20	228	**8**
C_{03}	3228	**12**	91	13
C_{30}	8.33x10^4	**62**	248	77

Table. 3.20: χ^2 statistics for a few block LBT (M=8) coefficients of Couple image.

	Gaussian	Laplacian	Gamma	Gen. Gaussian
C_{10}	1.85x10^6	1.36x10^5	484	**205**
C_{11}	3.72x10^{13}	3.69x10^5	152	**20**
C_{01}	1.34x10^6	497	**4**	5
C_{20}	3.90x10^9	1.26x10^5	**782**	1261
C_{02}	2.52x10^5	306	**7**	36
C_{12}	3.64x10^{12}	5.39x10^4	103	**15**
C_{21}	1.19x10^{13}	5.48x10^5	**56**	88
C_{03}	1.10x10^4	376	**19**	**19**
C_{30}	3.66x10^8	1.75x10^4	1159	**1025**

Table. 3.21: χ^2 statistics for a few block LBT (M=16) coefficients of Lena image.

	Gaussian	Laplacian	Gamma	Gen. Gaussian
C_{10}	4.03x10^4	236	**8**	12
C_{11}	3672	315	**15**	17
C_{01}	750	201	**52**	82
C_{20}	1.03x10^6	431	**37**	41
C_{02}	2.95x10^5	431	**8**	18
C_{12}	1.64x10^4	173	**9**	20
C_{21}	7723	620	23	**7**
C_{03}	791	104	**48**	53
C_{30}	4068	139	**15**	28

Table. 3.22: χ^2 statistics for a few block LBT (M=16) coefficients of Barbara image.

	Gaussian	Laplacian	Gamma	Gen. Gaussian
C_{10}	1534	92	16	**12**
C_{11}	644	66	21	**18**
C_{01}	327	44	70	**32**
C_{20}	1.15x10^7	764	34	**27**
C_{02}	1.81x10^8	722	17	**14**
C_{12}	1.59x10^5	64	6	**2**
C_{21}	9.75x10^8	386	**10**	12
C_{03}	742	22	87	**15**
C_{30}	2267	21	39	**3**

Table. 3.23: χ^2 statistics for a few block LBT (M=16) coefficients of Mandrill image.

	Gaussian	Laplacian	Gamma	Gen. Gaussian
C_{10}	3111	29	79	**26**
C_{11}	2813	**9**	163	12
C_{01}	1528	10	69	**7**
C_{20}	2350	106	103	**39**
C_{02}	123	**8**	151	**8**
C_{12}	1.54x10^5	9	79	**8**
C_{21}	124	**13**	138	**13**
C_{03}	655	11	156	**10**
C_{30}	23848	250	132	**80**

Table. 3.24: χ^2 statistics for a few block LBT (M=16) coefficients of Bridge image.

	Gaussian	Laplacian	Gamma	Gen. Gaussian
C_{10}	9715	24	105	**14**
C_{11}	1616	**9**	157	10
C_{01}	1.29x10^4	61	29	**13**
C_{20}	785	79	201	**67**
C_{02}	3319	**24**	174	**24**
C_{12}	199	13	188	**10**
C_{21}	54	21	290	**3**
C_{03}	3142	**9**	146	11
C_{30}	1699	24	107	**17**

Table. 3.25: χ^2 statistics for a few block LBT (M=16) coefficients of Aerial image.

	Gaussian	Laplacian	Gamma	Gen. Gaussian
C_{10}	**5**	30	163	**5**
C_{11}	18	22	119	**14**
C_{01}	14	20	129	**9**
C_{20}	157	**49**	105	51
C_{02}	51	**14**	77	17
C_{12}	41	**12**	91	15
C_{21}	18	7	86	**5**
C_{03}	37	23	113	**15**
C_{30}	17	10	84	**5**

Table. 3.26: χ^2 statistics for a few block LBT (M=16) coefficients of Couple image.

	Gaussian	Laplacian	Gamma	Gen. Gaussian
C_{10}	1.09x10^4	1493	103	**95**
C_{11}	8176	139	**7**	13
C_{01}	892	118	**10**	33
C_{20}	2.71x10^6	1.97x10^4	**236**	437
C_{02}	820	54	38	**18**
C_{12}	1.33x10^7	118	15	**11**
C_{21}	1.45x10^{10}	1.62x10^4	84	**43**
C_{03}	968	46	44	**12**
C_{30}	3.24x10^6	7929	675	**530**

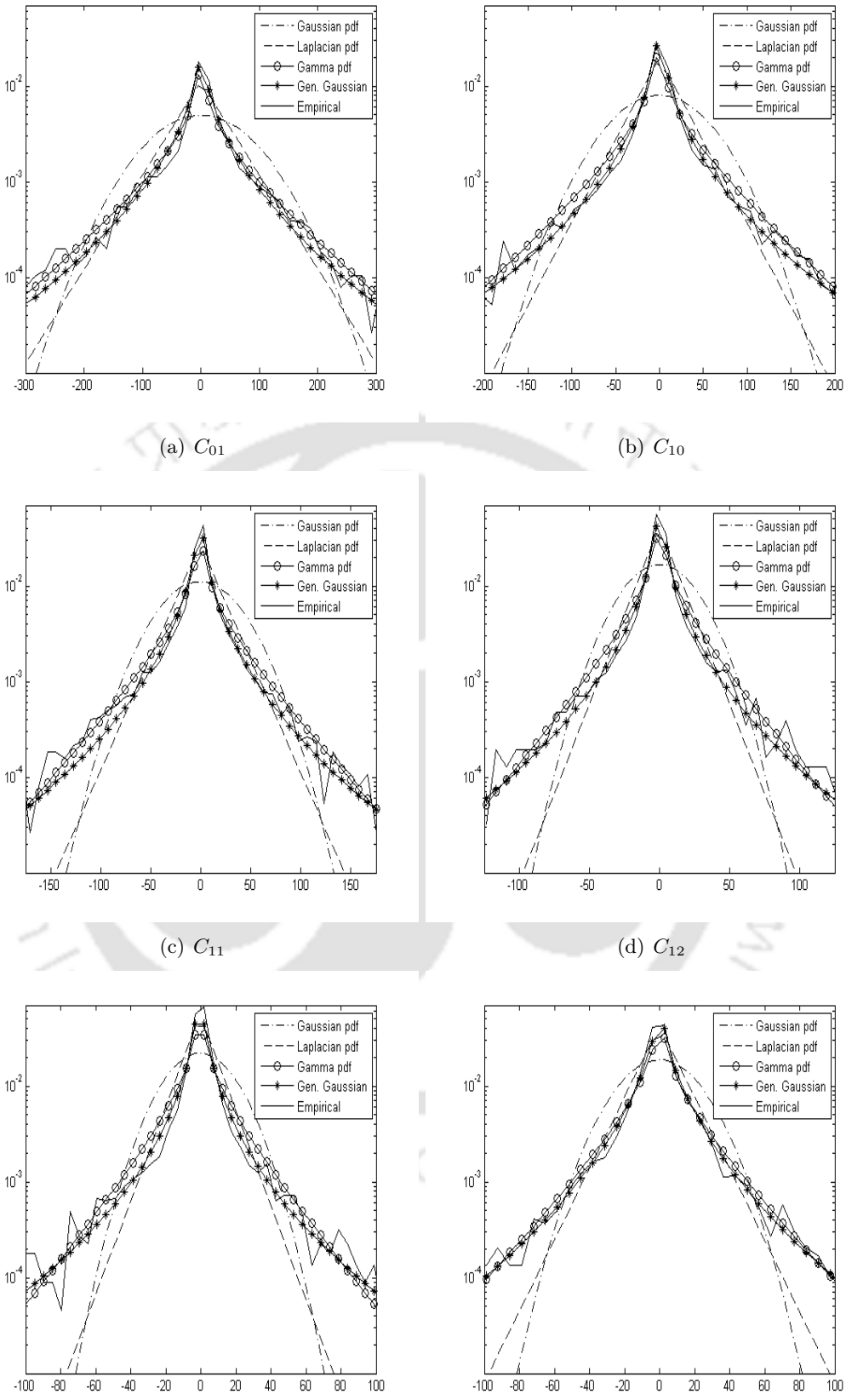

(a) C_{01} (b) C_{10}

(c) C_{11} (d) C_{12}

(e) C_{21} (f) C_{03}

Fig. 3.6: Logarithmic histograms of the block LOT (M=8) coefficients for Lena image and the best Gaussian, Laplacian, Gamma, Generalized Gaussian pdfs fitted to this histogram in log domain.

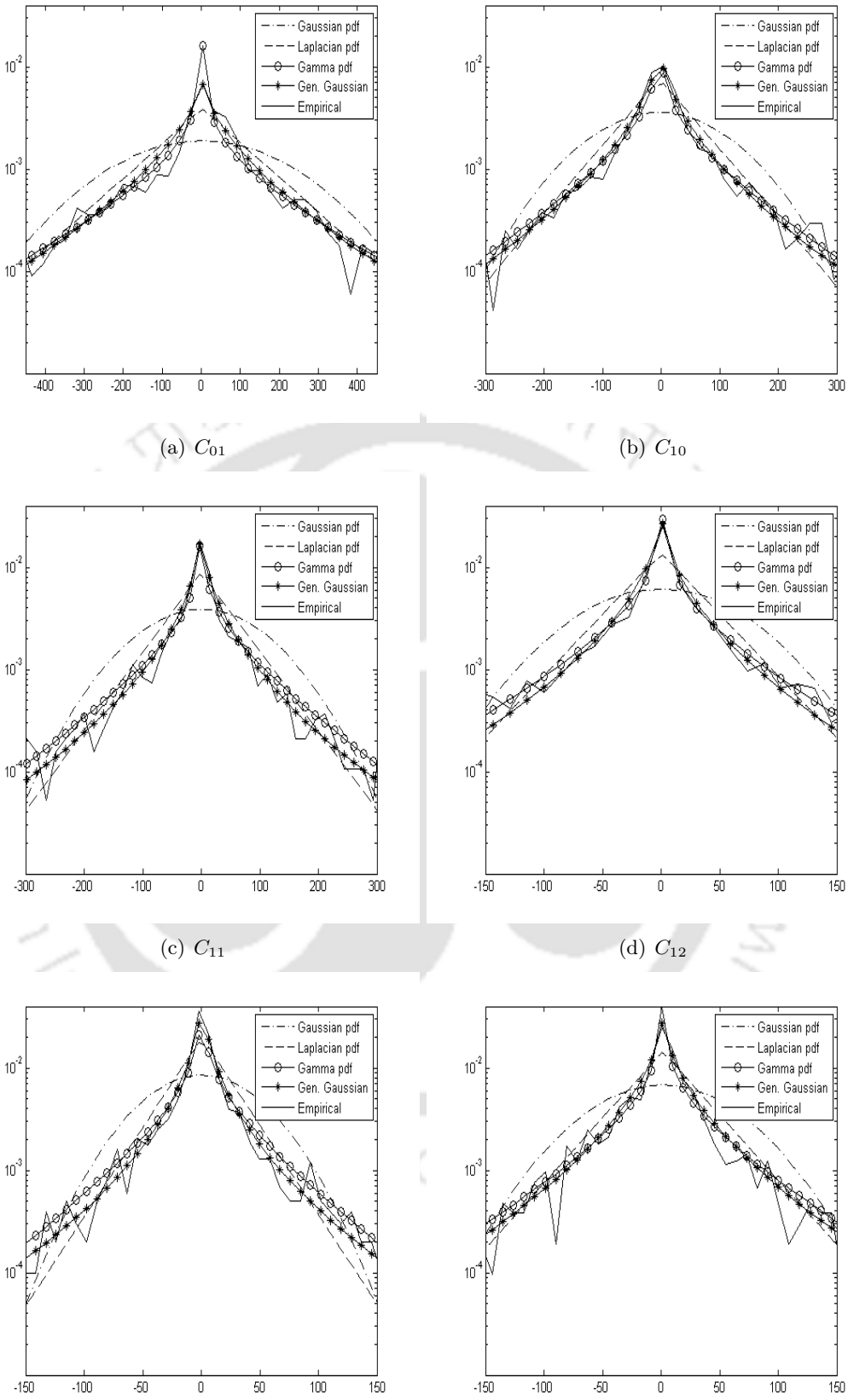

(a) C_{01} (b) C_{10}

(c) C_{11} (d) C_{12}

(e) C_{21} (f) C_{03}

Fig. 3.7: Logarithmic histograms of the block LOT (M=16) coefficients for Lena image and the best Gaussian, Laplacian, Gamma, Generalized Gaussian pdfs fitted to this histogram in log domain

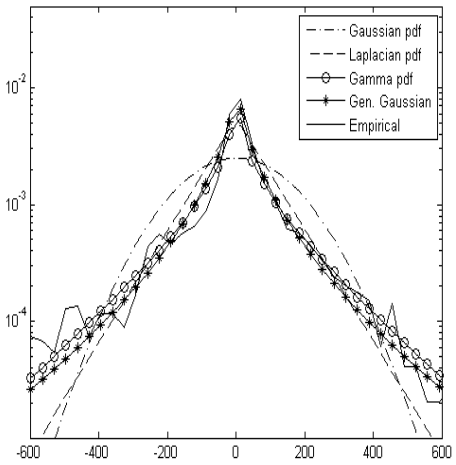

(a) C_{01}

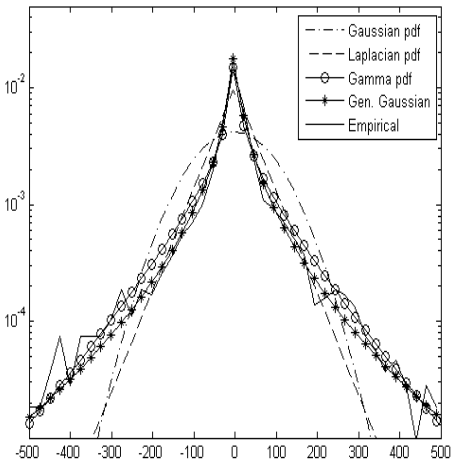

(b) C_{10}

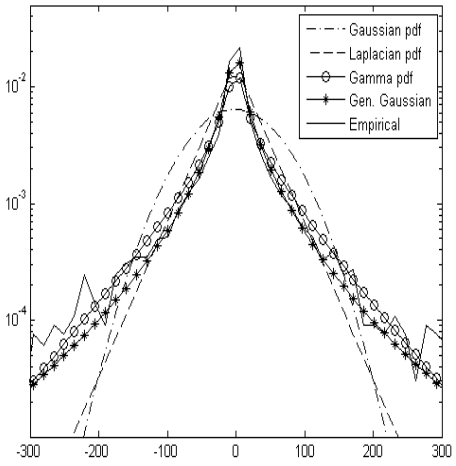

(c) C_{11}

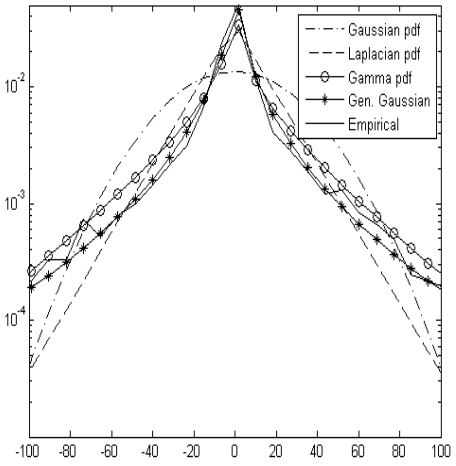

(d) C_{12}

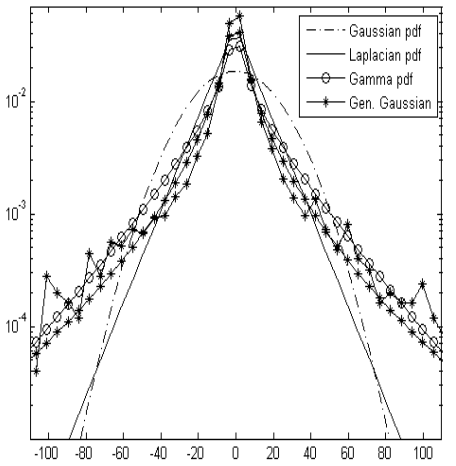

(e) C_{21}

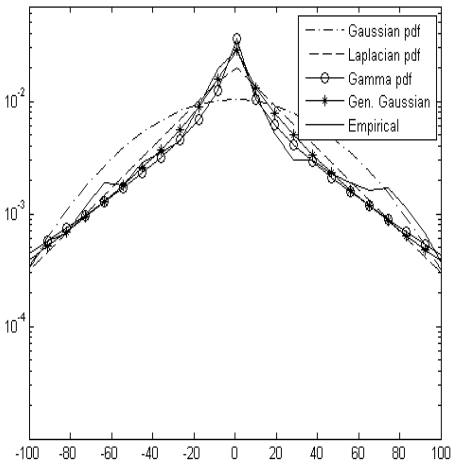

(f) C_{03}

Fig. 3.8: Logarithmic histograms of the block LBT (M=8) coefficients for Lena image and the best Gaussian, Laplacian, Gamma, Generalized Gaussian pdfs fitted to this histogram in log domain.

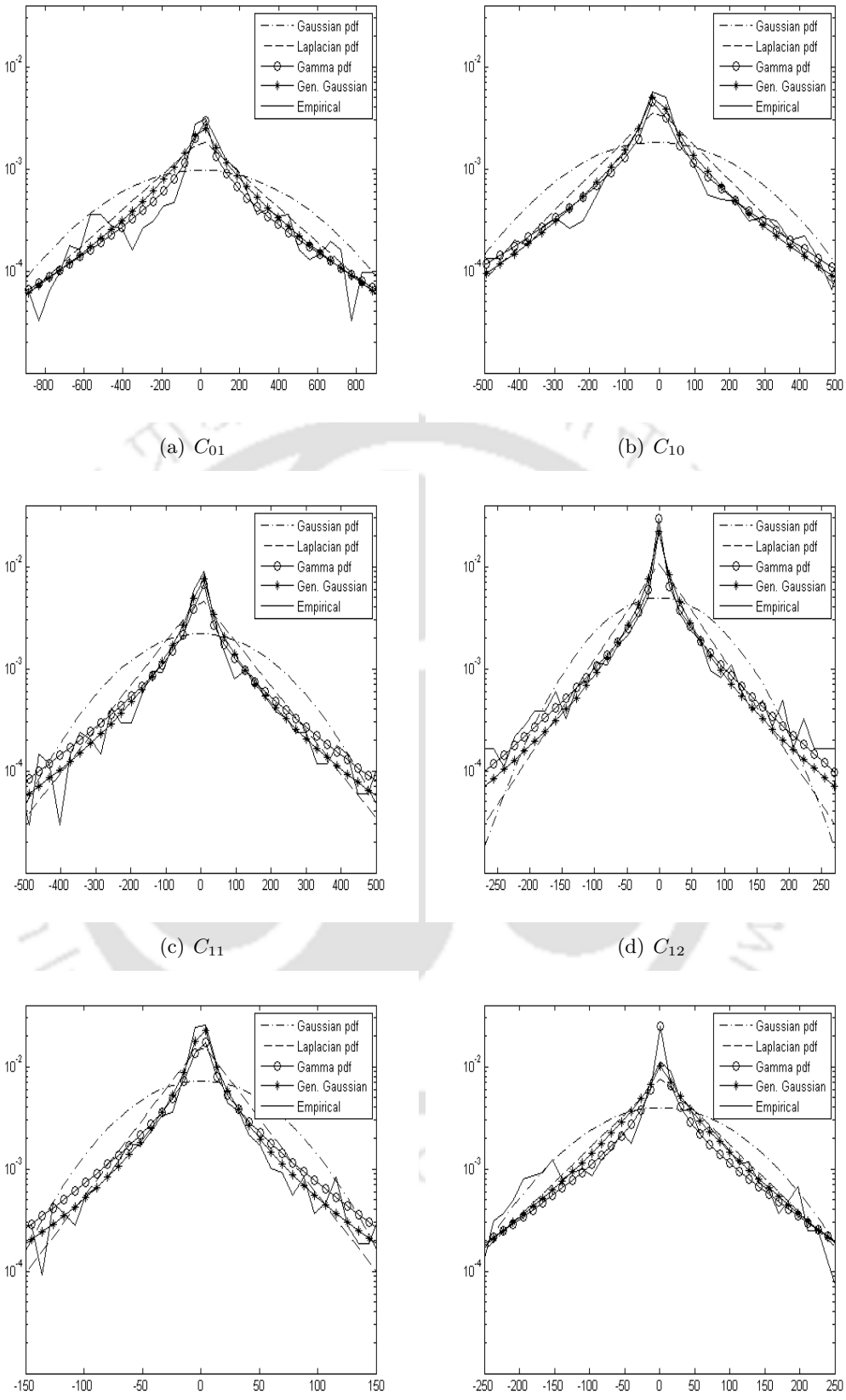

(a) C_{01} (b) C_{10}

(c) C_{11} (d) C_{12}

(e) C_{21} (f) C_{03}

Fig. 3.9: Logarithmic histograms of the block LBT (M=16) coefficients for Lena image and the best Gaussian, Laplacian, Gamma, Generalized Gaussian pdfs fitted to this histogram in log domain.

3.2.5 Concluding Remarks

In this section, we perform the KS and Chi-square goodness of fit tests to determine a suitable statistical distribution that best approximates the block LOT and LBT coefficients of natural images. The experimental results indicate that no single distribution can be used to model the distributions of all AC coefficients for all natural images. However the distribution of a majority of the significant AC coefficients can be modeled by the Generalized Gaussian distribution. The knowledge of the statistical distribution of lapped orthogonal transform and lapped biorthogonal transform coefficients helps in the design of optimal quantizers that may lead to minimum distortion and hence achieve optimal coding efficiency.

3.3 Modeling of Dyadic Rearranged Orthogonal Lapped Transform Coefficients of Natural Images

As discussed in Chapter 2, the LT coefficients can be rearranged in an octave-like representation and the dyadic rearranged LT coefficients can be modeled in a way similar to wavelet coefficients. In [47, 49], authors applied the zero tree quantizer on the rearranged LT coefficients for image compression achieving a performance comparable to that of relevant wavelet based image compression schemes. The octave-like representation of orthogonal LT coefficients is efficiently used in image denoising applications. Since the natural images generally comprise of some homogeneous regions and some important detailed information like edges and structures, the homogeneous regions usually results in coefficients which are very small in magnitude near to zero and the edge information are likely to result in a small number of large magnitude coefficients. Therefore, the non Gaussian statistics in the LT domain is quite expected as in wavelet coefficients. The previously published LT based image denoising schemes [18, 19, 64, 85] have assumed the coefficients to be non Gaussian, sharp peak with heavy tails and considered non Gaussian Bivariate, Laplacian mixture and Gaussian mixture models as probable distributions. The LT based image denoising schemes have shown encouraging performance when compared to wavelet based image denoising schemes. Further the LT based schemes are very good in preserving textural information. However no studies have been reported on the performance of Gaussian and different non Gaussian pdfs in modeling the dyadic rearranged LT coefficients. Such a study is very important in developing efficient algorithms for denoising and compression of natural images. In this section, we carry out an extensive study on the

appropriateness of different pdfs in modeling the dyadic rearranged LT coefficients. We perform KS test considering Gaussian, Laplacian, Gamma, Generalized Gaussian and symmetric normal inverse Gaussian distributions as probable models. In literature, KS test has been used in determination of most suitable prior distribution in modeling the wavelet coefficients of log-transformed reflectivity of medical ultrasound images [8] and also of natural images [7]. In our study, we follow the same test procedure.

3.3.1 Parameter Estimation

For Gaussian, Laplacian and Gamma pdfs, the same parameter estimation techniques discussed in Section 3.2.3 are used. The Generalized Gaussian pdf parameters can be estimated using either the Maximum Likelihood (ML) method ((3.11) and (3.13)) or the moment based methods [15, 74]. We use the moment-based method of [74] to estimate the parameters since this can be easily extended to images corrupted by additive white Gaussian noise [75].

Estimation of Shape Parameter of Generalized Gaussian Distribution Using Moment Based Method

The Generalized Gaussian pdf is given by (3.9) as discussed in the previous section. The root of the equation (3.11) gives the ML estimate $\widehat{\beta}$. The estimate of $\widehat{\alpha}$ for a known estimate of $\widehat{\beta}$ is given by (3.13).

The mean (μ), the scale parameter (α), and the shape parameter (β) are required to define the Generalized Gaussian pdf (3.9). The mean of the given data is estimated using the following expression:

$$\widehat{\mu}_X = \frac{1}{N}\sum_{i=1}^{N} x_i \tag{3.16}$$

and the variance of the given data is estimated by using

$$\widehat{\sigma}_X^2 = \frac{1}{N}\sum_{i=1}^{N} (x_i - \widehat{\mu}_X)^2 \tag{3.17}$$

where x_i with i=1,.....N, is the subband data and N is the total number of samples in the given subband. The relation between the variance (σ_X^2), the mean of the absolute values ($E\left[|X|\right]$)

and the shape parameter (β) of a Generalized Gaussian pdf is given by [74]:

$$F(\beta) = \frac{\sigma_X^2}{E^2[|X|]} = \frac{\Gamma\left(\frac{1}{\beta}\right)\Gamma\left(\frac{3}{\beta}\right)}{\Gamma^2\left(\frac{2}{\beta}\right)} \tag{3.18}$$

where $\Gamma(.)$ denotes the Gamma function. The estimate for the modified mean of the absolute value is given by

$$\widehat{E}[|X|] = \left(\frac{1}{N}\right)\sum_{i=1}^{N}|x_i - \widehat{\mu}_X| \tag{3.19}$$

The parameter β is estimated by solving

$$\widehat{\beta} = F^{-1}(\xi) \tag{3.20}$$

where the ratio ξ is given by

$$\xi = \frac{\widehat{\sigma}_X^2}{E^2[|X|]} \tag{3.21}$$

Once β is estimated, α can be determined using (3.15).

Symmetric Normal Inverse Gaussian (SNIG) probability density function

The symmetric normal inverse Gaussian pdf has been used in modeling the wavelet coefficients of log transformed reflectivity of medical ultrasound images [8] and of natural images [7] as well. The symmetric normal inverse Gaussian pdf parameters can be estimated using either the moment based method or ML method [56]. The ML method provides more accurate estimation of parameters compared to the moment based method. Since in this section the parameter estimation of Generalized Gaussian pdf is carried out using moment based method, for the sake of fair comparison in KS goodness of fit test, we estimate the parameters of SNIG pdf using moment based method.

The symmetric normal inverse Gaussian pdf is given by [29, 56]

$$f_X(x) = \frac{\alpha_s \delta K_1\left(\alpha_s\sqrt{\delta^2+(x-\mu)^2}\right)}{\pi\sqrt{\delta^2+(x-\mu)^2}} e^{(\delta\sqrt{\alpha_s^2-\beta_s^2}+\beta_s(x-\mu))} \tag{3.22}$$

where K_1 is the modified Bessel function of the second kind of order 1, α_s is the parameter that controls the steepness of the distribution, β_s is the asymmetry parameter, μ is the location parameter and δ is the scale parameter.

Given the sample mean (m), sample variance (v), sample kurtosis (k_s) and sample skewness (s),

the parameters α_s, β_s, μ and δ can be estimated using the following equations [56]:

$$\alpha_s = \sqrt{\frac{3k_s - 4s^2 - 9}{v(k_s - \frac{5}{3}s^2 - 3)^2}} \tag{3.23}$$

$$\beta_s = \frac{s}{\sqrt{v}\left(k_s - \frac{5}{3}s^2 - 3\right)} \tag{3.24}$$

$$\mu = m - \frac{3s\sqrt{v}}{3k_s - 4s^2 - 9} \tag{3.25}$$

$$\delta = 3^{\frac{3}{2}} \frac{\sqrt{v(k_s - \frac{5}{3}s^2 - 3)}}{3k_s - 4s^2 - 9} \tag{3.26}$$

for, $v > 0, k_s > 0$ and $s^2 < \left(\frac{3}{5}\right) k_s$.

3.3.2 Experimental Results

We use Lena, Barbara, Mandrill, Bridge, Aerial and Couple images in this section. The LOT coefficients are first rearranged into octave -like structure and then KS goodness of fit test is performed on all the detail subbands. The experiments are performed for LOT (M=8) and LOT (M=16). Note that LOT (M=8) coefficients can be rearranged into 3 level octave-like structure and LOT (M=16) coefficients can be rearranged into 4 level octave-like structure. The KS test results for LOT(M=8) and LOT(M=16) for Lena, Barbara, Mandrill, Bridge, Aerial and Couple images are shown in Tables 3.27 - 3.32 and Tables 3.33 - 3.38 respectively.

- **LOT (M=8)**: For Lena image 5 of 9 subbands show smallest KS statistic for Generalized Gaussian distribution. The LH1, HL1 and HH1 subbands show smallest KS statistic for Laplacian distribution. Only HL2 subband show smallest KS statistic for SNIG distribution. For Barbara image 7 of 9 subbands show smallest KS statistic for Generalized Gaussian distribution. Only HL1 and HL2 subbands show smallest KS statistic for Laplacian and SNIG distributions respectively. For Mandrill image also 7 of 9 subbands show smallest KS statistic for Generalized Gaussian distribution. Only LH2 and HH3 subband show minimum KS statistic for Laplacian distribution. For Bridge image 6 of 9 subbands show smallest KS statistic for Generalized Gaussian distribution. The HL2, HL3 and HH3 subbands show minimum KS statistic for Laplacian distribution. For the Couple image, 5 of 9 subbands show smallest KS statistic for Generalized Gaussian distribution.The LH1, HL2 and HH2 subands show minimum KS static for SNIG distribution. Only HL3 subband show smallest KS statistic for Laplacian

distribution. For the Aerial image, 6 of 9 subbands show smallest KS statistic for Generalized Gaussian distribution. Only LH1 and HL2 subbands show smallest KS statistic for Laplacian distribution. The HH1 subband show smallest KS statistic for SNIG distribution and subband HL3 show smallest KS statistic for both Laplacian and Generalized Gaussian distributions.

- **LOT (M=16)**: For Lena image 7 of 12 subbands show smallest KS statistic for Generalized Gaussian distribution. The LH1, HL2 and HH2 subbands show minimum KS statistic for SNIG distribution. However, HL3 and HH4 show minimum KS statistic for Laplacian and Gamma distribution respectively. For Barbara 8 of 12 subbands show minimum KS statistic for Generalized Gaussian distribution. The subbands LH1, HH2 and HL3 show minimum KS statistic for SNIG distribution. Only HH1 subband show minimum KS statistic for Laplacian distribution. For Mandrill also 8 of 12 subbands show smallest KS statistic for Generalized Gaussian distribution. Only LH2, LH3, LH4 and HL4 subbands show minimum KS statistic for Laplacian distribution. 9 of 12 subbands for Bridge image show smallest KS statistic for Generalized Gaussian distribution. The HL2 and HL3 subbands show minimum KS statistic for Laplacian and SNIG distributions respectively. However LH4 subband show smallest KS statistic for both Laplacian and Generalized Gaussian distributions. For Couple image 8 of 12 subbands show smallest KS statistic for Generalized Gaussian distribution. The subbands LH1, HH1 and HH2 show minimum KS statistic for SNIG distribution. However HL3 subband show minimum KS statistic for Gamma distribution. 9 of 12 subbands for Aerial image show smallest KS statistic for Generalized Gaussian distribution. Only LH1, HH1 and HL2 subbands show smallest KS statistic for SNIG distribution.

The results indicate that no particular distribution provides the smallest KS statistic for all the subbands for all the images. However, the Generalized Gaussian distribution shows the minimum KS statistic for most of the subbands. Fig. 3.10-3.11 show the empirical pdf of the dyadic rearranged subband LOT coefficients along with the fitted Gaussian, Laplacian, Gamma, Generalized Gaussian and SNIG pdfs. From Fig. 3.10-3.11 as well as from the values of the KS statistic, it is clear that the Generalized Gaussian distribution provides a better fit to the empirical distribution than that achieved by the Gaussian, Laplacian, Gamma and SNIG pdf.

Table. 3.27: KS statistics for dyadic rearranged LOT (M=8) coefficients in different subbands of Lena image.

Level		LH	HL	HH
1	Gaussian	0.1369	0.0846	0.0565
	Laplacian	**0.0358**	**0.0150**	**0.0220**
	Gamma	0.0834	0.1025	0.1198
	Gen. Gaussian	0.0465	0.0283	0.0233
	SNIG	0.0438	0.0449	0.0493
2	Gaussian	0.1953	0.1709	0.1895
	Laplacian	0.0931	0.0596	0.0793
	Gamma	0.0576	0.1161	0.0682
	Gen. Gaussian	**0.0356**	0.0879	**0.0500**
	SNIG	0.0802	**0.0209**	0.0540
3	Gaussian	0.1905	0.1957	0.2112
	Laplacian	0.1224	0.1017	0.1282
	Gamma	0.0688	0.0495	0.0675
	Gen. Gaussian	**0.0584**	**0.0229**	**0.0474**
	SNIG	0.1204	0.1080	0.1420

Table. 3.28: KS statistics for dyadic rearranged LOT (M=8) coefficients in different subbands of Barbara image.

Level		LH	HL	HH
1	Gaussian	0.2682	0.1483	0.1874
	Laplacian	0.1295	**0.0386**	0.0556
	Gamma	0.1216	0.0750	0.0607
	Gen. Gaussian	**0.0647**	0.0476	**0.0529**
	SNIG	0.1079	0.0548	0.0628
2	Gaussian	0.1684	0.1510	0.2185
	Laplacian	0.0727	0.0504	0.1084
	Gamma	0.0907	0.0870	0.0730
	Gen. Gaussian	**0.0579**	0.0499	**0.0358**
	SNIG	0.0653	**0.0205**	0.1003
3	Gaussian	0.1555	0.1835	0.1824
	Laplacian	0.0793	0.0994	0.0865
	Gamma	0.0534	0.0900	0.0492
	Gen. Gaussian	**0.0292**	**0.0569**	**0.0244**
	SNIG	0.1064	0.0857	0.0806

Table. 3.29: KS statistics for dyadic rearranged LOT (M=8) coefficients in different subbands of Mandrill image.

Level		LH	HL	HH
1	Gaussian	0.1031	0.1232	0.0861
	Laplacian	0.0233	0.0447	0.0149
	Gamma	0.0874	0.0700	0.0932
	Gen. Gaussian	**0.0192**	**0.0103**	**0.0117**
	SNIG	0.0204	0.0568	0.0214
2	Gaussian	0.0869	0.1190	0.0973
	Laplacian	**0.0180**	0.0420	0.0247
	Gamma	0.1050	0.0791	0.0901
	Gen. Gaussian	0.0206	**0.0150**	**0.0144**
	SNIG	0.0279	0.0530	0.0337
3	Gaussian	0.0668	0.1044	0.0698
	Laplacian	0.0262	0.0445	**0.0097**
	Gamma	0.1241	0.1186	0.1017
	Gen. Gaussian	**0.0246**	**0.0400**	0.0117
	SNIG	0.0270	0.0647	0.0384

Table. 3.30: KS statistics for dyadic rearranged LOT (M=8) coefficients in different subbands of Bridge image.

Level		LH	HL	HH
1	Gaussian	0.0979	0.0857	0.0861
	Laplacian	0.0278	0.0148	0.0178
	Gamma	0.0821	0.0908	0.0901
	Gen. Gaussian	**0.0078**	**0.0095**	**0.0069**
	SNIG	0.0350	0.0194	0.0394
2	Gaussian	0.0819	0.0827	0.0736
	Laplacian	0.0172	**0.0145**	0.0095
	Gamma	0.0918	0.1050	0.0965
	Gen. Gaussian	**0.0075**	0.0233	**0.0043**
	SNIG	0.0381	0.0204	0.0311
3	Gaussian	0.0861	0.0972	0.0666
	Laplacian	0.0252	**0.0233**	**0.0103**
	Gamma	0.1011	0.1027	0.1038
	Gen. Gaussian	**0.0180**	0.0262	0.0108
	SNIG	0.0305	0.0308	0.0227

Table. 3.31: KS statistics for dyadic rearranged LOT (M=8) coefficients in different subbands of Couple image.

Level		LH	HL	HH
1	Gaussian	0.2223	0.2416	0.2229
	Laplacian	0.0876	0.0954	0.0762
	Gamma	0.0797	0.0972	0.0916
	Gen. Gaussian	0.0692	**0.0417**	**0.0561**
	SNIG	**0.0180**	0.0693	0.0666
2	Gaussian	0.1856	0.2409	0.1891
	Laplacian	0.0959	0.1595	0.0682
	Gamma	0.0993	0.1986	0.0712
	Gen. Gaussian	**0.0710**	0.1993	0.0636
	SNIG	0.0942	**0.1322**	**0.0247**
3	Gaussian	0.1666	0.2548	0.1942
	Laplacian	0.1007	**0.1703**	0.0909
	Gamma	0.1062	0.1774	0.0557
	Gen. Gaussian	**0.0678**	0.1771	**0.0400**
	SNIG	0.0949	0.2738	0.0653

Table. 3.32: KS statistics for dyadic rearranged LOT (M=8) coefficients in different subbands of Aerial image.

Level		LH	HL	HH
1	Gaussian	0.0787	0.0792	0.0600
	Laplacian	**0.0113**	0.0254	0.0146
	Gamma	0.1027	0.1020	0.1125
	Gen. Gaussian	0.0155	**0.0120**	0.0133
	SNIG	0.0121	0.0495	**0.0103**
2	Gaussian	0.0690	0.0779	0.0387
	Laplacian	0.0144	**0.0142**	0.0288
	Gamma	0.1130	0.1080	0.1283
	Gen. Gaussian	**0.0138**	0.0256	**0.0099**
	SNIG	0.0233	0.0253	0.0120
3	Gaussian	0.0523	0.0593	0.0389
	Laplacian	0.0307	**0.0244**	0.0347
	Gamma	0.1322	0.1247	0.1345
	Gen. Gaussian	**0.0269**	**0.0244**	**0.0199**
	SNIG	0.0317	0.0455	0.0235

Table. 3.33: KS statistics for dyadic rearranged LOT (M=16) coefficients in different subbands of Lena image.

Level		LH	HL	HH
1	Gaussian	0.1287	0.0760	0.0478
	Laplacian	0.0328	0.0292	0.0242
	Gamma	0.0853	0.1076	0.1227
	Gen. Gaussian	0.0418	**0.0144**	**0.0204**
	SNIG	**0.0310**	0.0486	0.0489
2	Gaussian	0.1944	0.1742	0.1764
	Laplacian	0.0888	0.0628	0.0667
	Gamma	0.0560	0.0686	0.0615
	Gen. Gaussian	**0.0364**	0.0442	0.0400
	SNIG	0.0861	**0.0292**	**0.0299**
3	Gaussian	0.1665	0.1621	0.2071
	Laplacian	0.0870	**0.0743**	0.1241
	Gamma	0.0983	0.1367	0.0837
	Gen. Gaussian	**0.0608**	0.0939	**0.0615**
	SNIG	0.1062	0.0746	0.1094
4	Gaussian	0.1769	0.1597	0.1830
	Laplacian	0.1176	0.0772	0.1132
	Gamma	0.0937	0.0698	**0.0403**
	Gen. Gaussian	**0.0780**	**0.0261**	0.0404
	SNIG	0.1218	0.1025	0.1479

Table. 3.34: KS statistics for dyadic rearranged LOT (M=16) coefficients in different subbands of Barbara image.

Level		LH	HL	HH
1	Gaussian	0.2721	0.1345	0.1800
	Laplacian	0.1256	0.0462	**0.0486**
	Gamma	0.1257	0.0800	0.0626
	Gen. Gaussian	0.0705	**0.0294**	0.0573
	SNIG	**0.0501**	0.1146	0.0813
2	Gaussian	0.1744	0.1539	0.2235
	Laplacian	0.0696	0.0493	0.0949
	Gamma	0.0489	0.0625	0.0778
	Gen. Gaussian	**0.0273**	**0.0328**	0.0503
	SNIG	0.0469	0.0736	**0.0485**
3	Gaussian	0.1396	0.1533	0.1947
	Laplacian	0.0473	0.0580	0.0820
	Gamma	0.0785	0.0781	0.0609
	Gen. Gaussian	**0.0321**	0.0398	**0.0520**
	SNIG	0.0455	**0.0390**	0.0527
4	Gaussian	0.1163	0.1533	0.1441
	Laplacian	0.0650	0.0763	0.0628
	Gamma	0.1089	0.0867	0.0722
	Gen. Gaussian	**0.0513**	**0.0350**	**0.0279**
	SNIG	0.0792	0.0966	0.0867

Table. 3.35: KS statistics for dyadic rearranged LOT (M=16) coefficients in different subbands of Mandrill image.

Level		LH	HL	HH
1	Gaussian	0.1006	0.1255	0.0879
	Laplacian	0.0221	0.0475	0.0159
	Gamma	0.0864	0.0760	0.0919
	Gen. Gaussian	**0.0166**	**0.0167**	**0.0113**
	SNIG	0.0174	0.0525	0.0208
2	Gaussian	0.0823	0.1145	0.0983
	Laplacian	**0.0124**	0.0404	0.0251
	Gamma	0.0973	0.0878	0.0885
	Gen. Gaussian	0.0134	**0.0198**	**0.0106**
	SNIG	0.0216	0.0505	0.0350
3	Gaussian	0.0652	0.0959	0.0803
	Laplacian	**0.0223**	0.0254	0.0187
	Gamma	0.1221	0.1027	0.0982
	Gen. Gaussian	0.0223	**0.0250**	**0.0143**
	SNIG	0.0251	0.0370	0.0427
4	Gaussian	0.0819	0.0975	0.0602
	Laplacian	**0.0159**	**0.0381**	0.0143
	Gamma	0.1012	0.1308	0.1103
	Gen. Gaussian	0.0177	0.0430	**0.0121**
	SNIG	0.0300	0.0517	0.0281

Table. 3.36: KS statistics for dyadic rearranged LOT (M=16) coefficients in different subbands of Bridge image.

Level		LH	HL	HH
1	Gaussian	0.0895	0.0759	0.0755
	Laplacian	0.0201	0.0084	0.0105
	Gamma	0.0894	0.0962	0.0971
	Gen. Gaussian	**0.0077**	**0.0080**	**0.0055**
	SNIG	0.0336	0.0189	0.0299
2	Gaussian	0.0718	0.0736	0.0682
	Laplacian	0.0084	**0.0091**	0.0087
	Gamma	0.1006	0.1035	0.1059
	Gen. Gaussian	**0.0074**	0.0190	**0.0084**
	SNIG	0.0292	0.0274	0.0294
3	Gaussian	0.0666	0.0942	0.0484
	Laplacian	0.0200	0.0298	0.0194
	Gamma	0.1194	0.1226	0.1199
	Gen. Gaussian	**0.0135**	0.0413	**0.0102**
	SNIG	0.0196	**0.0258**	0.0173
4	Gaussian	0.1080	0.0946	0.0721
	Laplacian	**0.0291**	0.0256	0.0225
	Gamma	0.0964	0.1072	0.1180
	Gen. Gaussian	**0.0291**	**0.0210**	0.0249
	SNIG	0.0562	0.0465	**0.0208**

Table. 3.37: KS statistics for dyadic rearranged LOT (M=16) coefficients in different subbands of Couple image.

Level		LH	HL	HH
1	Gaussian	0.2021	0.2373	0.2108
	Laplacian	0.0744	0.0926	0.0579
	Gamma	0.0635	0.0930	0.0807
	Gen. Gaussian	0.0518	**0.0421**	0.0713
	SNIG	**0.0186**	0.0613	**0.0498**
2	Gaussian	0.1776	0.2028	0.1721
	Laplacian	0.0871	0.0883	0.0595
	Gamma	0.0521	0.0599	0.0656
	Gen. Gaussian	**0.0250**	**0.0323**	0.0500
	SNIG	0.0818	0.1085	**0.0102**
3	Gaussian	0.1386	0.2333	0.1720
	Laplacian	0.0706	0.1085	0.0698
	Gamma	0.1131	**0.1040**	0.0558
	Gen. Gaussian	**0.0593**	0.1109	**0.0304**
	SNIG	0.0918	0.1166	0.0596
4	Gaussian	0.1394	0.2255	0.1388
	Laplacian	0.1070	0.1285	0.0642
	Gamma	0.1588	0.0795	0.0770
	Gen. Gaussian	**0.0970**	**0.0399**	**0.0342**
	SNIG	0.0983	0.1576	0.0826

Table. 3.38: KS statistics for dyadic rearranged LOT (M=16) coefficients in different subbands of Aerial image.

Level		LH	HL	HH
1	Gaussian	0.0804	0.0837	0.0592
	Laplacian	0.0131	0.0389	0.0146
	Gamma	0.1029	0.1112	0.1139
	Gen. Gaussian	0.0184	**0.0197**	0.0124
	SNIG	**0.0100**	0.0693	**0.0077**
2	Gaussian	0.0491	0.0758	0.0312
	Laplacian	0.0279	0.0290	0.0262
	Gamma	0.1284	0.1251	0.1305
	Gen. Gaussian	**0.0139**	0.0366	**0.0119**
	SNIG	0.0169	**0.0218**	0.0123
3	Gaussian	0.0520	0.0839	0.0351
	Laplacian	0.0316	0.0418	0.0458
	Gamma	0.1321	0.1308	0.1371
	Gen. Gaussian	**0.0225**	**0.0405**	**0.0188**
	SNIG	0.0243	0.0484	0.0216
4	Gaussian	0.0519	0.0306	0.0343
	Laplacian	0.0617	0.0605	0.0667
	Gamma	0.1615	0.1615	0.1692
	Gen. Gaussian	**0.0354**	**0.0296**	**0.0314**
	SNIG	0.0368	0.0299	0.0322

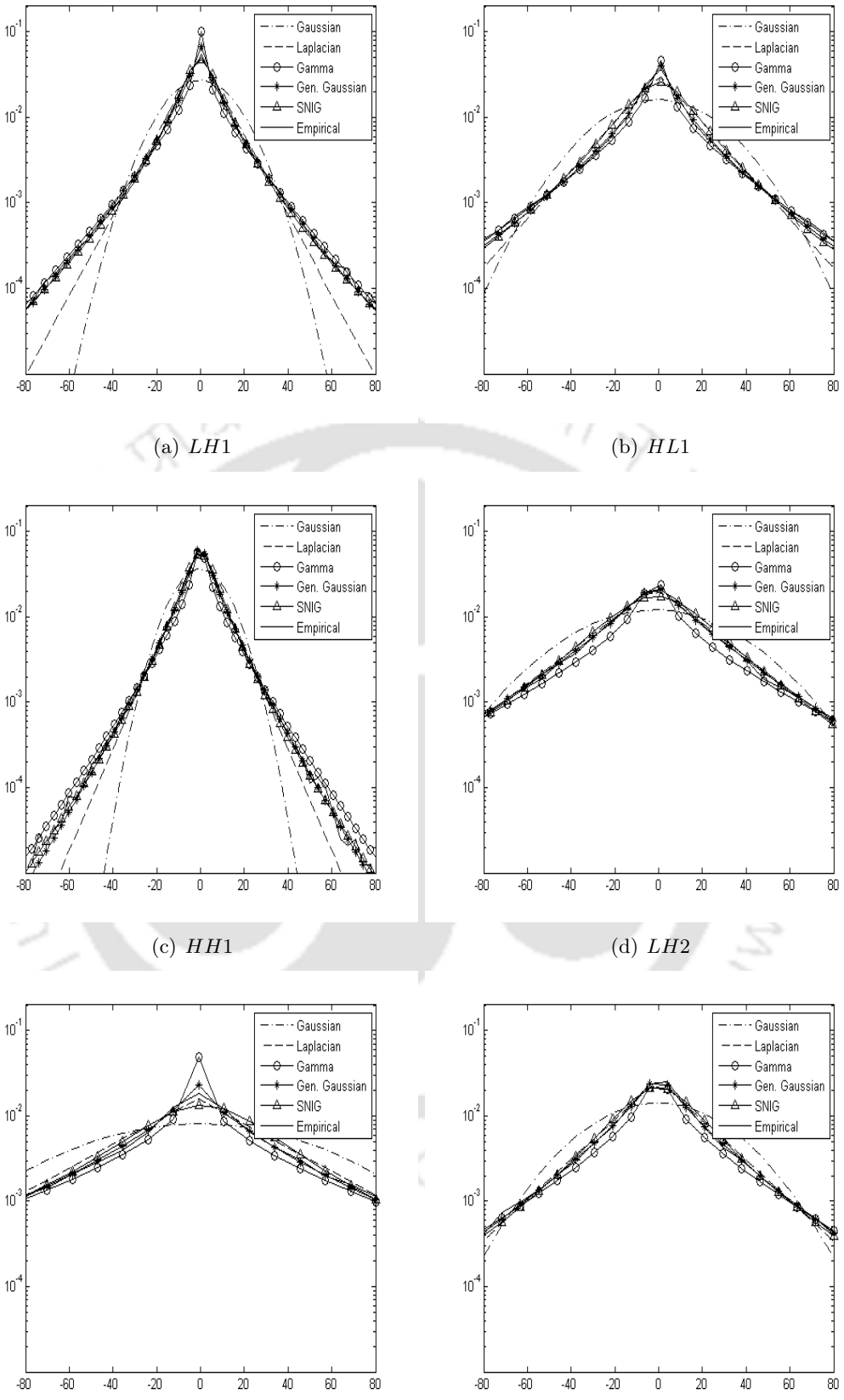

(a) $LH1$ (b) $HL1$

(c) $HH1$ (d) $LH2$

(e) $HL2$ (f) $HH2$

Fig. 3.10: Logarithmic histograms of the dyadic remapped LOT (M=8) coefficients for Mandrill image and the best Gaussian, Laplacian, Gamma, Generalized Gaussian, SNIG pdfs fitted to this histogram in log domain.

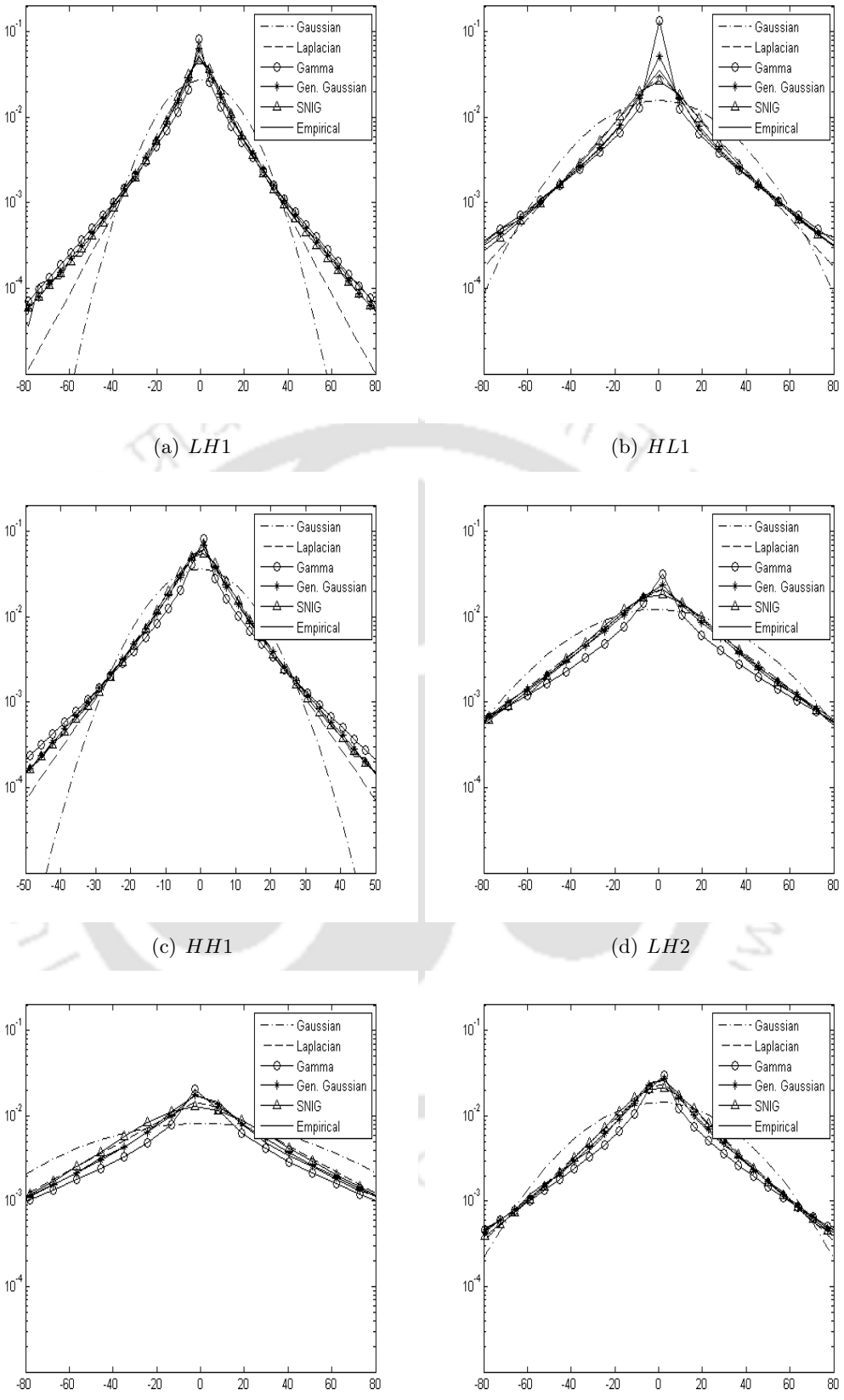

(a) $LH1$ (b) $HL1$

(c) $HH1$ (d) $LH2$

(e) $HL2$ (f) $HH2$

Fig. 3.11: Logarithmic histograms of the dyadic remapped LOT (M=16) coefficients for Mandrill image and the best Gaussian, Laplacian, Gamma, Generalized Gaussian, SNIG pdfs fitted to this histogram in log domain.

3.3.3 Concluding Remarks

The LT coefficients when rearranged into octave-like representation can be modeled in a way similar to wavelet coefficients. The rearranged LT coefficients when used in applications like image compression, denoising, deblocking etc. can perform at par with relevant wavelet transform based methods. In this paper, an extensive comparative study on the performance of Gaussian and several non-Gaussian pdfs in modeling of rearranged orthogonal LT coefficients in different subbands has been performed. The Gaussian, Laplacian, Gamma, Generalized Gaussian and SNIG pdfs are considered in our experiments. Based on KS goodness of fit test, we show that most of the subband coefficients for most of the natural images can be better modeled by Generalized Gaussian pdf. The knowledge of appropriate statistical distribution helps in developing more efficient algorithms for compression and denoising applications.

Chapter 4

Image Denoising in Lapped Transform Domain

Images are often contaminated by noise during acquisition, processing, storage and transmission. Noise reduction is therefore an important task since noise affects the quality of the image and makes post processing operations like compression and segmentation quite difficult. The main aim of denoising is to suppress the noise while preserving the signal features as much as possible. The early techniques of image denoising in spatial domain blur the edges. Due to the sparseness property of the wavelet transform, there has been a good amount of work carried out in the field of image denoising in the wavelet domain [7, 12, 16, 21, 23, 26, 38, 40, 41, 51, 61, 72, 75]. However, the discrete wavelet transforms do not perform well in capturing the directional information in natural images. The preservation of textures is highly important in almost all image processing applications. Lapped Transform (LT) based image denoising schemes have shown good potential and are very competitive with wavelet based denoising algorithms [18, 19, 64, 85]. It was observed that the LTs are very good in preserving oscillatory components present in natural images such as textures [18, 19]. In the literature, only non Gaussian bivariate model [85], hidden Markov tree [18] and global Laplacian mixture models [64] were investigated in relation to LT domain image denoising.

We have shown in the previous chapter that the Generalized Gaussian distribution best models the dyadic remapped LT coefficients. In this chapter, we therefore investigate the image denoising performance of LT using Generalized Gaussian distribution. We propose to use a Bayesian MMSE estimator to reduce the noise. The Bayesian MMSE estimator is developed based on modeling the global distribution of the dyadic rearranged LT coefficients by the Generalized Gaussian distribution. We further investigate the image denoising performance of LT using local Gaussian and local Laplacian distribution models.

This chapter is organized as follows: a brief introduction to various image denoising schemes is presented in Section 4.1. In Section 4.2, a LT based image denoising algorithm based on Generalized Gaussian prior is presented along with experimental results. In Section 4.3, we extend the local Wiener filtering concept to LT domain and then propose an efficient doubly local Wiener filtering framework in the same domain. Experimental results are also provided in the same section. Section 4.4 describes a LT based image denoising scheme where the subband rearranged LT coefficients are modeled using Laplace probability density function with local variance. A *maximum a posteriori* (MAP) estimator using the Laplace probability density function with local variance is used for the estimation of noise free LT coefficients. The simulation results are also presented in the same section.

4.1 Introduction

We consider digital images corrupted by additive zero mean white Gaussian noise. In the past several years, considerable work has been reported on orthogonal wavelet based image denoising techniques [7, 12, 16, 21, 23, 26, 38, 40, 41, 51, 61, 72, 75]. The thresholding based image denoising schemes [12,16] have shown good performance in reducing the noise effectively. Some of these methods employ local pdf and use separate thresholds for each coefficient in a subband. These schemes have shown very good results among the various thresholding based image denoising schemes.

In some approaches [7, 51, 75] the wavelet coefficients of the noise free image are modeled by a particular pdf assuming the coefficients to be independent identically distributed. A Bayesian estimator like the minimum mean square error (MMSE) estimator or maximum a posteriori (MAP) estimator is developed using this pdf and this estimation is used to denoise the noisy transformed coefficients. Many wavelet based image denoising schemes use the dependencies among the wavelet coefficients. Some of these methods [21,26,40,41,51] use linear minimum mean square error (LMMSE) estimator to reduce the noise assuming the local distribution of the transformed coefficients to be Gaussian. This approach exploits the intrascale dependencies and has shown good results in the literature.

Image denoising methods that exploit the interscale dependencies and hybrid intrascale and interscale dependencies among the wavelet coefficients have also been reported in the literature [7, 18, 72]. The wavelet domain hidden Markov tree model (HMT) was proposed in [68] where the interscale dependencies were exploited in image denoising.

Recently, a few approaches using lapped transform based image denoising have been proposed

[18, 19, 64, 85]. The motivation for image denoising in lapped transform domain is that the lapped transforms have good energy compaction and are robust to oversmoothing. The lapped transforms are also orthogonal transforms. Thus signal and noise statistics can be modeled precisely in the lapped transform domain. Since the lapped transforms are block transforms, the lapped orthogonal transform (LOT) [45] coefficients are first rearranged into an octave-like decomposition form [18, 19, 49, 82, 85]. Then the statistics of the rearranged lapped orthogonal transform coefficients in a subband are modeled in a way similar to that in wavelet coefficients. In [85], Yang et al., formulated a maximum a posteriori estimation problem and used non Gaussian bivariate model to reduce the compression artifacts and the additive white gaussian noise in images. In [18], Duval et al. extended the hidden Markov tree model to lapped orthogonal transform domain (LOT-HMT). Duval et al. [19] further improved the results of LOT-HMT denoising by combining it with a redundant decomposition. Raghvendra et al. [64] modeled the LT coefficients using a mixture of Laplace distributions that does not make use of local parameters.

4.2 Lapped Transform based Image Denoising with the Generalized Gaussian prior

Since LTs are block transforms, the orthogonal LT coefficients are first rearranged in an octave-like representation and the rearranged LT coefficients are then modeled using a non Gaussian pdf. The histogram plots of the finest subbands of the Lena and Boat images are shown in Fig. 4.1(a) and 4.1(b). The distributions have a sharp peak around zero and extended tails at both sides of the peak. This indicates that the orthogonal LT is very sparse and the majority of the orthogonal LT coefficients are close to zero. The kurtosis of the distributions shown in Fig. 4.1(a) and 4.1(b) are found to be 17.43 and 26.94 respectively which are much larger than 3 (the kurtosis for a Gaussian pdf). The histogram plot of the finest subbands of all the natural images used in our experiments show distributions with sharp peaks around zero and heavy tails. The marginal distributions of real world images in the LT domain are highly non Gaussian. The Generalized Gaussian distribution has been used by many authors to model the image wavelet coefficients. The SNIG distribution has also been used to model the heavy tailed image wavelet coefficients. In [7], Symmetrical Normal Inverse Gaussian pdf is shown to be more appropriate than the Generalized Gaussian pdf for modeling the image wavelet coefficients based on the KS goodness of fit test.

For noise free natural images, the histograms of the rearranged LOT coefficients in a subband

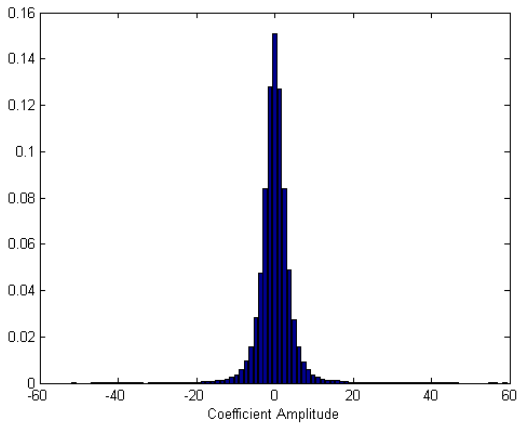

(a) For Lena image

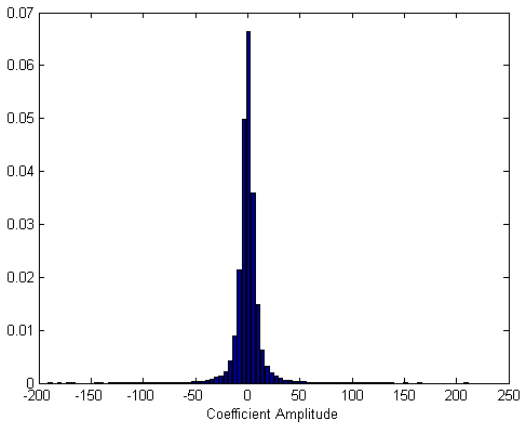

(b) For Boat image

Fig. 4.1: Marginal statistics of finest subband of two images. The kurtosis of the two distributions are measured at 17.43 and 26.94 for (a) and (b) respectively, showing that the coefficients are highly non Gaussian.

are typically non Gaussian sharply peaked around zero with heavy tails. In chapter 3, we have shown that the Generalized Gaussian distribution is a suitable model for describing the statistics of rearranged LOT coefficients in a subband. Based on this finding, we propose a LT based image denoising technique using a Bayesian estimator based on modeling the global distribution of the rearranged LOT coefficients using a Generalized Gaussian pdf.

We assume that the image is corrupted by additive zero mean Gaussian noise with variance σ_n^2. The orthogonal LT coefficients of the noisy image are given by

$$y(k) = x(k) + n(k) \tag{4.1}$$

where *x(k)* denotes the clean LT coefficients and *n(k)* is the additive zero mean white Gaussian noise.

The Generalized Gaussian prior can be expressed as

$$f_X(x) = \frac{\beta}{2\alpha\Gamma\left(\frac{1}{\beta}\right)} \exp - \left(\frac{|x|}{\alpha}\right)^{\beta} \tag{4.2}$$

where α is the scale parameter, β is the shape parameter and $\Gamma(.)$ is the Gamma function given by

$$\Gamma(z) = \int_0^{\infty} e^{-t} t^{z-1} dt, z > 0 \tag{4.3}$$

For the special cases $\beta = 2$ or $\beta = 1$, the Generalized Gaussian pdf becomes a Gaussian or a Laplacian pdf respectively. The Generalized Gaussian model is a popular model used in various

image processing tasks; many authors call it as Generalized Laplacian model. The parameters of Generalized Gaussian distribution α and β can be calculated from the histogram of noise free LOT coefficients. Let σ_x^2 be the sample variance and κ_x be the kurtosis of the histogram of a noise free image, then we have [75]

$$\sigma_x^2 = \frac{\alpha^2 \Gamma\left(\frac{3}{\beta}\right)}{\Gamma\left(\frac{1}{\beta}\right)} \tag{4.4}$$

$$\kappa_x = \frac{\Gamma\left(\frac{1}{\beta}\right)\Gamma\left(\frac{5}{\beta}\right)}{\Gamma^2\left(\frac{3}{\beta}\right)} \tag{4.5}$$

Since the histogram of the noise free LOT coefficients of an image is not available, the parameters of the Generalized Gaussian model is estimated from the noisy LOT coefficients. For the noisy image LOT coefficients contaminated by additive gaussian noise, the variance σ_y^2 and the fourth moment $M4_y$ is given as [75]

$$\sigma_y^2 = \sigma_n^2 + \frac{\alpha^2 \Gamma\left(\frac{3}{\beta}\right)}{\Gamma\left(\frac{1}{\beta}\right)} \tag{4.6}$$

$$M4_y = 3\sigma_n^4 + \frac{6\sigma_n^2 \alpha^2 \Gamma\left(\frac{3}{\beta}\right)}{\Gamma\left(\frac{1}{\beta}\right)} + \frac{\alpha^4 \Gamma\left(\frac{5}{\beta}\right)}{\Gamma\left(\frac{1}{\beta}\right)} \tag{4.7}$$

where σ_n^2 is the noise variance. The noise variance is estimated from the noisy LT coefficients, employing a robust median estimator that uses the LT coefficients in the finest scale as described in [17]:

$$\widehat{\sigma}_n^2 = \frac{Median\left(|y(m,n)|\right)}{0.6745}, y(m,n) \in HH_1 \tag{4.8}$$

Once σ_n^2 is estimated, α and β are then estimated solving (4.6) and (4.7). Fig. 4.2(a), 4.3(a) and 4.4(a) show the rearranged LOT coefficients in a particular subband of clean Lena, Mandrill and Bridge images respectively. Fig. 4.2(b), 4.3(b) and 4.4(b) show the histogram of rearranged LOT coefficients of subband shown in Fig. 4.2(a), 4.3(a) and 4.4(a) respectively. Fig. 4.2(c), 4.3(c) and 4.4(c) show the Generalized Gaussian model estimated from Fig. 4.2(b), 4.3(b) and 4.4(b) respectively. Fig. 4.2(d), 4.3(d) and 4.4(d) show the rearranged LOT coefficients in a particular subband of noisy Lena, Mandrill and Bridge image respectively. Fig. 4.2(e), 4.3(e) and 4.4(e) show the histogram of rearranged LOT coefficients of subband shown in Fig. 4.2(d), 4.3(d) and 4.4(d) respectively. Fig. 4.2(f), 4.3(f) and 4.4(f) show the Generalized Gaussian model estimated from Fig. 4.2(e), 4.3(e) and 4.4(e) respectively.

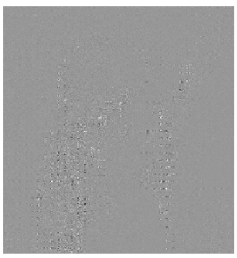

(a) Noise free Horizontal subband (1st level)

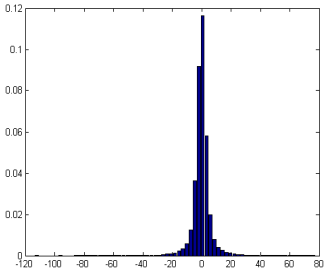

(b) Histogram of (a)

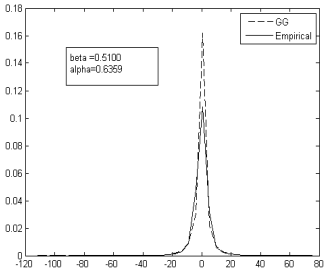

(c) GG model estimated from (b)

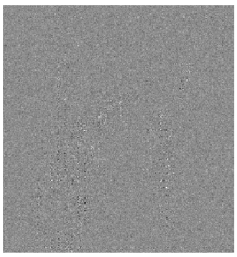

(d) Noisy Horizontal subband (1st level)

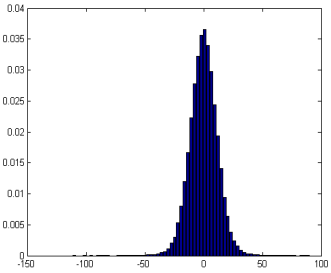

(e) Histogram of (d)

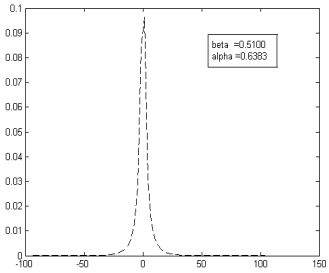

(f) GG model estimated from (e)

Fig. 4.2: Generalized Gaussian prior for dyadic rearranged LOT coefficients in a subband for Lena image and estimation of its parameters

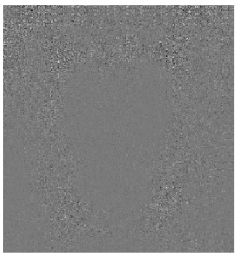

(a) Noise free Diagonal subband (1st level)

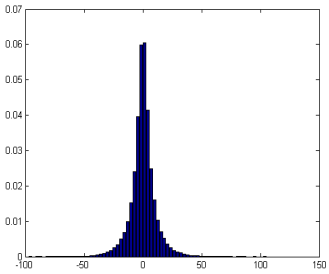

(b) Histogram of (a)

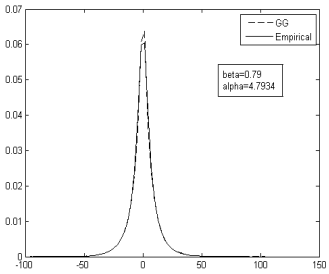

(c) GG model estimated from (b)

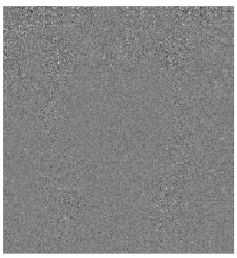

(d) Noisy Horizontal subband (1st level)

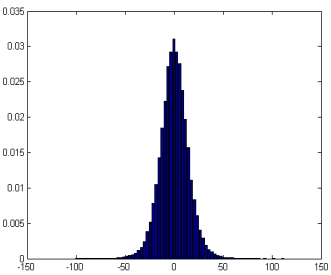

(e) Histogram of (d)

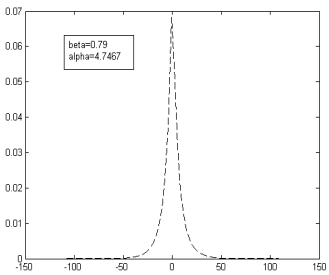

(f) GG model estimated from (e)

Fig. 4.3: Generalized Gaussian prior for dyadic rearranged LOT coefficients in a subband for Mandrill image and estimation of its parameters

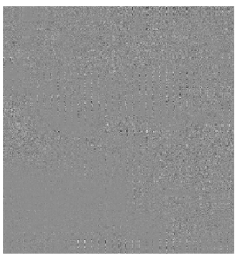

(a) Noise free Vertical subband (1st level)

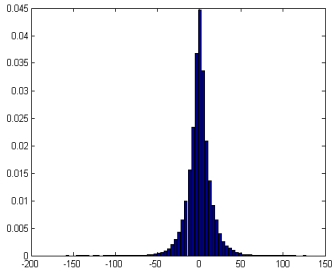

(b) Histogram of (a)

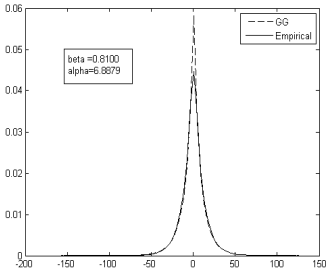

(c) GG model estimated from (b)

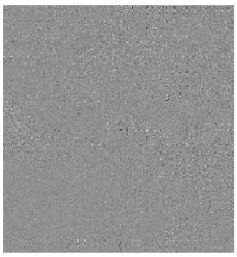

(d) Noisy Vertical subband (1st level)

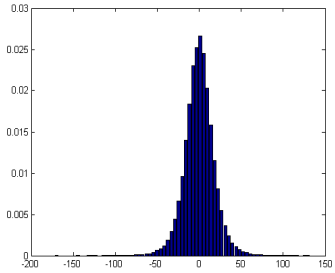

(e) Histogram of (d)

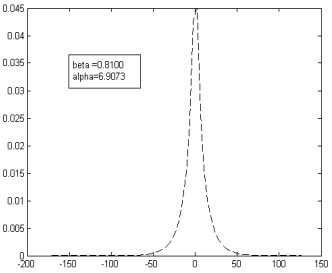

(f) GG model estimated from (e)

Fig. 4.4: Generalized Gaussian prior for dyadic rearranged LOT coefficients in a subband for Bridge image and estimation of its parameters

4.2.1 Bayesian MMSE Estimate

To provide an estimate $\widehat{x}$ from the noisy coefficients, a Bayesian MMSE estimator using $\widehat{\alpha}$ and $\widehat{\beta}$ is used. The Bayesian estimate is obtained by minimizing the Bayes risk function and can be expressed as [37]

$$\widehat{x}(y) = \arg\,.\min_{\widehat{x}} \int C\left[\widehat{x}(y), x\right] P_{x|y}(x|y)dx \tag{4.9}$$

where the right hand side of (4.9) is the cost averaged over $P_{x|y}\left(x|y\right)$ and $C(.)$ is the cost function. By using the squared error cost function $(\widehat{x}(y) - x)^2$ for $C\left[\widehat{x}(y), x\right]$ in (4.9), an MMSE estimator is obtained. Since the MMSE estimator is a conditional mean of x given y, the resulting Bayesian estimator can be expressed as

$$\widehat{x}(y) = \int x P_{x|y}(x|y)dx \tag{4.10}$$

Using Bayes theorem, (4.10) can be written as

$$\widehat{x}(y) = \frac{\int x P_n(y-x) P_x(x)dx}{\int P_n(y-x) P_x(x)dx} \tag{4.11}$$

where P_n denotes the probability density function of the noise, and P_x the prior probability density function of the image. For the Generalized Gaussian prior, (4.11) does not have a closed form expression and hence the solution is obtained numerically using a method given in [6]. Equation (4.11) can also be written as [6]

$$\widehat{x}(y) = \frac{P_n(y) * G(x)}{P_n(y) * P_x(x)} \tag{4.12}$$

where $G(x) = xP_x(x)$ and $*$ represents the convolution operator. For each subband, the Bayesian estimates of the coefficients are obtained using the following steps [6]:

1. If y_{min} and y_{max} respectively denote the minimum and the maximum values of y in a subband, then we have q as

$$q = \frac{y_{\max} - y_{\min}}{C_b} \tag{4.13}$$

where C_b is an integer.

2. Compute the values of $\tilde{y}_{p_s}$ given as

$$\tilde{y}_{p_s} = y_{p\min} + p_s q \tag{4.14}$$

where $y_{p\min} = y_{\min} + \frac{q}{2}$ and $p_s = 0, 1, ..., C_b - 1$.

3. Compute the vector $n_y = \left[n_y^1, n_y^2, ..., n_y^{p_s}\right]$, where $n_y^{p_s} = P_n(y)\,\big|_{y=\tilde{y}_{p_s}}$.

4. Compute the values $x_y = \left[x_y^1, x_y^2, ..., x_y^{p_s}\right]$, where $x_y^{p_s} = P_x(x)|_{x=\tilde{y}_{p_s}}$.

5. Obtain the vector $G_y = \left[G^1, G^2, ...G^{p_s}\right]$, where $G^{p_s} = G(x)\,\big|_{x=\tilde{y}_{p_s}}$.

6. Compute the vector $\tilde{x} = [\tilde{x}_1, \tilde{x}_2, ..., \tilde{x}_{p_s}]$, using $\tilde{x} = {}^{(G_y * n_y)}\!\not/_{(x_y * n_y)}$ where $\not/$ represents element wise division.

7. Obtain the Bayesian estimate $\widehat{x}$ using the spline interpolation method and the value of $\tilde{x}_{p_s}$.

4.2.2 Experimental Results

We select six of the most popular test images in our experiments which are Lena, Barbara, Mandrill, Boat, Bridge and Fingerprint. The chosen test images contains a variety of textures and complex patterns. We use the Peak Signal to Noise Ratio (PSNR) as the objective measure to evaluate the

denoising performance. PSNR is defined by the following expression:

$$PSNR = 10 \log_{10} \frac{255^2}{MSE} \tag{4.15}$$

where *MSE* is the normalized mean square difference between the original image and the reconstructed image.

$$MSE = \frac{1}{R_0 C_0} \sum_{i=1}^{R_0} \sum_{j=1}^{C_0} (x_{i,j} - \hat{x}_{i,j})^2 \tag{4.16}$$

where R_0 and C_0 are the number of rows and columns of the image.

The performance of our proposed image denoising method based on the Generalized Gaussian prior is compared with a recent wavelet based image denoising scheme which uses symmetrical normal inverse Gaussian prior [7]. The authors in [7], based on KS goodness of fit test, found symmetrical normal inverse Gaussian (SNIG) distribution to be more appropriate distribution for modeling the image wavelet coefficients. They developed a Bayesian MMSE estimator based on modeling the global distribution of the wavelet coefficients with the SNIG pdf and used it to obtain a set of approximately noise-free coefficients that are used to obtain the signal variances. We compare our PSNR results with their results which are obtained using Bayesian MMSE estimator only. We also compare our results with Bayes-shrink [12], hidden markov tree (HMT) based method [14], Ref. [71] and a well known locally adaptive Bishrink [72] algorithm as shown in Table 4.1. The methods discussed in [71] and [7] have reported results only for Lena, Barbara and Boat images, therefore we compare our results with [71] and [7] methods only for these three images. We call the proposed LT domain image denoising method using Generalized Gaussian prior as LOT-GG. Experimental results show that the proposed LOT-GG scheme outperforms the methods discussed in [14], [12], [71] and [7] for all the test images. However, the LOT-GG scheme outperforms [72] only for Barbara, Mandrill, Bridge and Fingerprint images and underperforms for Lena and Boat images by a small margin. Fig 4.5 show visual results obtained using Bayes-shrink [12], Bi-shrink [72] and LOT-GG algorithm for Barbara image. It can be seen from these figures that the proposed method provides images that are of better visual quality than that of Bayes-shrink [12] method and comparable to that of Bi-shrink method [72].

Table 4.2 show the PSNR comparison between the proposed LOT-GG method and two previously published results on LT based image denoising. The results show that the LOT-GG algorithm outperforms the LOT domain HMT based method [18] and a LOT domain method which uses the

Laplacian mixture distribution to model the global distribution of LT coefficients [64].

The wavelet domain method using a Bayesian estimator based on modeling the global distribution of the coefficients using Generalized Gaussian prior is referred to as WT-GG method. We used an orthogonal wavelet transform with four levels of decomposition and Daubechies length-8 wavelet for the implementation of WT-GG algorithm. In Table 4.3, we compare the LOT-GG and WT-GG algorithms in terms of PSNR. The results indicate that the LOT-GG outperforms WT-GG consistently with a good margin in terms of PSNR. Fig. 4.6 show visual results obtained using Bi-shrink [72], WT-GG and LOT-GG algorithms for Bridge image. It can be observed that the proposed method provides denoised images that are of improved visual quality and comparable to that of Bi-shrink method [72].

4.2.3 Concluding Remarks

In chapter 3, based on KS goodness of fit test, Generalized Gaussian distribution was found to be most appropriate statistical distribution for modeling the dyadic rearranged LT coefficients in a subband. This chapter proposed a LT based image denoising technique using a Bayesian estimator based on modeling the global distribution of the rearranged LT coefficients using a Generalized Gaussian pdf. The proposed method outperforms several well known wavelet based image denoising schemes including a scheme which uses a Bayesian estimator based on modeling the global distribution of the wavelet coefficients using a SNIG pdf. The SNIG pdf was demonstrated to be most appropriate pdf for modeling the wavelet transform coefficients [7]. The proposed method based on Generalized Gaussian prior also consistently outperforms the WT-GG which clearly indicates that this prior is highly suitable in modeling the global distribution of remapped LOT coefficients.

Table. 4.1: PSNR (in dB) comparison between proposed LT domain image denoising algorithm using Generalized Gaussian prior and several wavelet based image denoising algorithms

	Lena (512x512)			
σ_n	10	15	20	25
Noisy	28.15	24.62	22.12	20.18
Ref. [7]	33.89	32.01	30.71	29.75
Bayes-shrink [12]	31.10	28.72	27.12	25.90
HMT [14]	33.84	31.76	30.39	29.24
Ref. [71]	33.94	32.06	30.73	29.81
Bi-shrink [72]	**34.34**	**32.42**	**30.98**	**29.96**
LOT-GG (M=8)	33.92	31.95	30.58	29.59
LOT-GG (M=16)	33.96	32.07	30.76	29.78
	Barbara (512x512)			
σ_n	10	15	20	25
Noisy	28.13	24.62	22.11	20.17
Ref. [7]	31.84	29.49	27.89	26.70
Bayes-shrink [12]	33.23	31.20	29.95	28.99
HMT [14]	31.36	29.23	27.80	25.99
Ref. [71]	31.13	28.71	27.25	25.97
Bi-shrink [72]	32.13	29.78	28.24	27.03
LOT-GG (M=8)	32.44	30.10	28.54	27.33
LOT-GG (M=16)	**32.70**	**30.49**	**28.93**	**27.85**
	Boat (512x512)			
σ_n	10	15	20	25
Noisy	28.13	24.61	22.11	20.17
Ref. [7]	32.16	30.22	28.83	27.82
Bayes-shrink [12]	31.89	29.76	28.33	27.25
HMT [14]	32.28	30.31	28.84	27.68
Ref. [71]	32.25	30.25	28.93	27.91
Bi-shrink [72]	32.41	**30.50**	**29.10**	**28.04**
LOT-GG (M=8)	**32.47**	30.35	28.91	27.85
LOT-GG (M=16)	32.43	30.32	28.98	27.93
	Mandrill (512x512)			
σ_n	10	15	20	25
Noisy	28.13	24.61	22.11	20.17
Bayes-shrink [12]	29.52	26.84	25.19	24.01
Bi-shrink [72]	28.73	26.71	25.27	24.19
LOT-GG (M=8)	**29.86**	27.29	25.66	24.55
LOT-GG (M=16)	29.82	**27.31**	**25.71**	**24.58**
	Bridge (512x512)			
σ_n	10	15	20	25
Noisy	28.13	24.61	22.11	20.17
Bayes-shrink [12]	30.00	27.52	25.96	24.91
Bi-shrink [72]	29.63	27.48	26.06	25.08
LOT-GG (M=8)	**30.26**	**27.92**	26.50	25.49
LOT-GG (M=16)	30.25	27.91	**26.51**	**25.51**
	Fingerprint (512x512)			
σ_n	10	15	20	25
Noisy	28.13	24.61	22.11	20.17
Bayes-shrink [12]	30.98	28.73	27.21	26.09
Bi-shrink [72]	30.89	28.57	27.06	25.94
LOT-GG (M=8)	31.73	29.45	27.91	26.73
LOT-GG (M=16)	**31.94**	**29.73**	**28.18**	**27.06**

Table. 4.2: PSNR (in dB) comparison between LT based proposed denoising algorithm using Generalized Gaussian prior and two existing LT domain image denoising algorithms

	Lena (512x512)				Barbara (512x512)			
σ_n	7.7	15.5	23.1	33.1	7.7	15.5	23.1	33.1
Noisy	30.42	24.33	20.88	17.72	30.39	24.34	20.85	17.76
[18]	33.80	29.60	27.20	24.90	33.30	29.10	26.60	24.20
[64]	35.00	31.70	29.80	28.20	33.70	29.70	27.60	25.70
LOT-GG (M=8)	35.24	31.81	29.97	28.25	34.03	29.95	27.77	25.93
LOT-GG (M=16)	**35.25**	**31.89**	**30.14**	**28.55**	**34.23**	**30.31**	**28.19**	**26.48**

Table. 4.3: PSNR (in dB) comparison between proposed LOT-GG and wavelet based DWT-GG image denoising scheme for various images.

	Lena (512x512)			
σ_n	10	15	20	25
Noisy	28.14	24.62	22.11	20.24
DWT-GG	33.60	31.62	30.31	29.28
LOT-GG (M=8)	33.92	31.95	30.58	29.59
LOT-GG (M=16)	**33.96**	**32.07**	**30.76**	**29.78**
	Barbara (512x512)			
σ_n	10	15	20	25
DWT-GG	31.33	28.86	27.27	26.12
LOT-GG (M=8)	32.44	30.10	28.54	27.33
LOT-GG (M=16)	**32.70**	**30.49**	**28.93**	**27.85**
	Boat (512x512)			
σ_n	10	15	20	25
DWT-GG	32.21	30.08	28.68	27.62
LOT-GG (M=8)	**32.47**	**30.35**	28.91	27.85
LOT-GG (M=16)	32.43	30.32	**28.98**	**27.93**
	Mandrill (512x512)			
σ_n	10	15	20	25
DWT-GG	29.69	27.08	25.45	24.31
LOT-GG (M=8)	**29.86**	27.29	25.66	24.55
LOT-GG (M=16)	29.82	**27.31**	**25.71**	**24.58**
	Bridge (512x512)			
σ_n	10	15	20	25
DWT-GG	30.17	27.79	26.34	25.30
LOT-GG (M=8)	**30.26**	**27.92**	26.50	25.49
LOT-GG (M=16)	30.25	27.91	**26.51**	**25.51**
	Fingerprint (512x512)			
σ_n	10	15	20	25
DWT-GG	31.36	29.11	27.56	26.41
LOT-GG (M=8)	31.73	29.45	27.91	26.73
LOT-GG (M=16)	**31.94**	**29.73**	**28.18**	**27.06**

(a) Original Barbara image

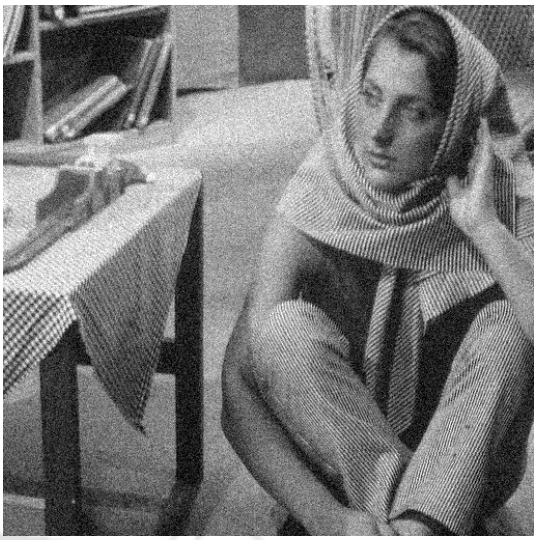

(b) Noisy Barbara image (σ_n=20)(PSNR=22.11 dB)

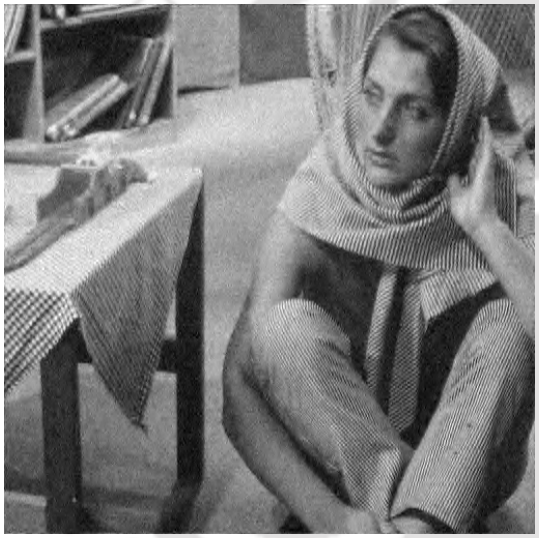

(c) Bayes-shrink [12](PSNR=27.12 dB)

(d) Bi-shrink [72](PNSR=28.24 dB)

(e) Denoised using LOT-GG (M=8) (PSNR=28.55 dB)

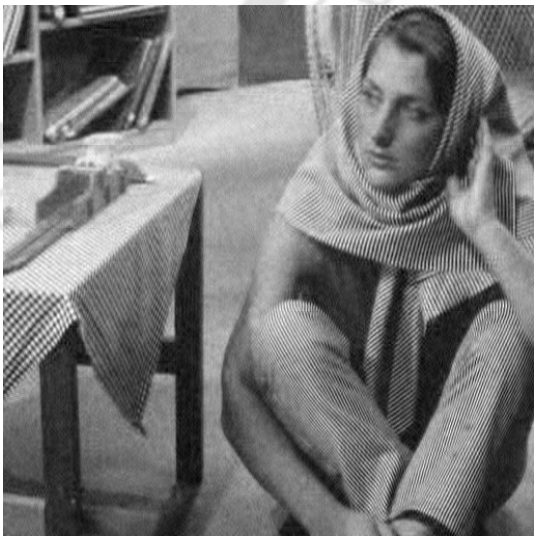

(f) Denoised using LOT-GG (M=16)(PSNR=28.95)

Fig. 4.5: Denoised images of Barbara using proposed denoising scheme based on Generalized Gaussian prior in LT domain.

(a) Original Bridge image

(b) Noisy Bridge image (σ_n=20)(PSNR=22.22)

(c) Bi-shrink [72](PSNR=26.06 dB)

(d) DWT-GG (PSNR=26.35 dB)

(e) Denoised using LOT-GG (M=8) (PSNR=26.50 dB)

(f) Denoised using LOT-GG (M=16)(PSNR=26.51 dB)

Fig. 4.6: Visual results comparison between images denoised by Bi-shrink [72], DWT-GG and LOT-GG algorithms.

4.3 Local Wiener Filtering in Lapped Transform Domain

In this section, we investigate the performance of local Wiener filtering in the LT domain. Among the various approaches in wavelet based image denoising methods, one popular class of approach is to use the linear minimum mean square error estimator [7, 21, 26, 38, 40, 41, 51] to restore the noisy wavelet image coefficients. These methods assume the local distribution of the wavelet coefficients to be Gaussian with spatially varying variance. These methods are popular due to their good denoising performance and low computational complexity. Further the doubly local Wiener filtering approach in the wavelet domain [40, 41] has shown very good results when compared to many other wavelet based image denoising schemes. In this section, we first extend the local Wiener filtering concept to LT domain. Motivated by the results of local Wiener filtering in the LT domain, we next propose a doubly local Wiener filtering framework in the LT domain. The main objective here is to extend the local Wiener filtering concept to the LT domain and to design a simple low complexity doubly local Wiener filtering framework in the same domain. The local Wiener filter gives optimal performance

Table. 4.4: Average values of Skewness and Kurtosis for different Subbands of Dyadic Rearranged LOT Coefficients for Lena, Barbara and Mandrill test images

Image	Neighborhood	Subbands								
		LH1	HL1	HH1	LH2	HL2	HH2	LH3	HL3	HH3
Lena	3x3	0.3535	0.8372	0.2281	-1.862	0.7239	-0.8908	0.4934	0.3051	1.2134
		3.1342	3.5158	2.5160	4.4896	2.6419	2.8619	2.4222	2.3131	3.3659
	5x5	0.8275	0.7484	0.1729	0.6920	0.6956	-1.4508	0.9435	0.8639	0.6137
		5.9982	6.4932	4.5891	7.2069	4.0035	4.9221	4.8327	6.2303	5.4446
	7x7	1.6863	0.5357	0.1304	0.2668	-0.9660	-0.8530	0.0326	0.5922	0.9600
		10.6247	8.0605	11.3366	9.2748	9.6368	6.7358	4.8580	7.1505	6.5846
Barbara	3x3	-1.1482	0.4139	1.1984	-2.0741	-2.0762	-0.3954	-0.0564	0.3857	-0.0507
		2.6407	2.6620	2.5994	5.8296	6.0071	3.2485	3.7227	2.8462	2.9792
	5x5	0.0389	-0.6546	-0.4016	-0.9158	-3.5096	-0.7606	1.6405	-0.6030	0.7073
		4.7223	4.5463	5.6443	5.7045	16.2097	4.9404	5.7568	5.3757	5.3297
	7x7	0.3261	-0.4974	-2.0076	-1.0925	-3.7380	-1.0943	2.1975	-1.0638	0.4505
		5.3807	5.2573	13.7229	7.2753	17.4262	11.2610	8.2301	6.4646	6.7556
Mandrill	3x3	-1.7251	-0.0510	-0.6517	0.1846	-0.9325	-2.1835	1.2578	1.1008	-0.0488
		4.5570	3.8218	2.5896	2.9907	4.8098	6.2336	3.1036	2.6088	3.6444
	5x5	-0.9042	-0.3822	-0.1715	-0.1958	-1.7006	-2.5061	0.6481	1.6890	-0.2789
		5.5738	4.7076	4.1815	4.4542	13.0904	8.1920	5.3140	5.2113	4.8176
	7x7	-0.8221	-2.6409	-0.3815	-2.4146	-1.4952	-0.8888	-0.6299	2.1567	-0.5451
		5.4468	22.8289	5.6217	10.4310	12.4511	8.1798	6.5280	7.7059	9.4547

when both the signal and the noise are Gaussian distributed [37]. In Table 4.4, we determine the

average skewness and kurtosis values of different subbands of dyadic remapped LOT coefficients of the test images Lena, Barbara and Mandrill using 3x3, 5x5 and 7x7 neighborhoods. For a Gaussian distribution, the skewness value (which tells about the symmetry of the distribution) is 0 and the kurtosis value (which tells about the peakedness) is 3. It can be observed from Table 4.4 that the deviation of the average value of the skewness from the actual value of 0 is minimum for 3x3 window size for all the three images and the average value of the kurtosis that deviates from 3 is also minimum for 3x3 window size. Therefore, we approximate the local distribution of the dyadic remapped LT coefficients by a Gaussian distribution and consider a 3x3 window for describing the local distribution of the coefficients in a subband. We assume the local distribution of the coefficients to be independent identically distributed Gaussian with zero mean and spatially varying variance. The local Wiener filtering in LT domain is performed in two major steps. First, the estimation of variance for each LT coefficient is carried out using the observed noisy coefficients in a local neighborhood and then the LT coefficients of signal are estimated.

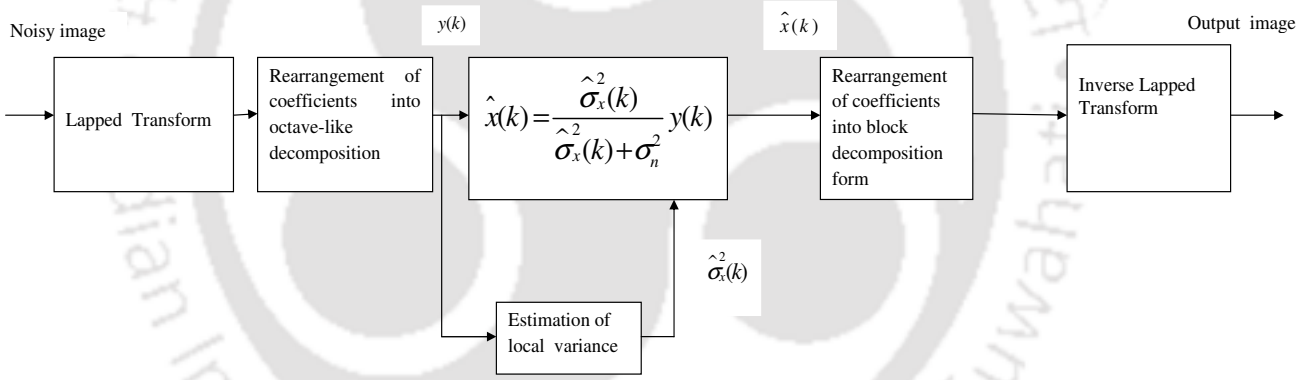

Fig. 4.7: Block diagram of the proposed image denoising method based on local Wiener filtering in the LT domain

For each noisy LT coefficient, an estimate of $\sigma_x^2(k)$ is formed based on its local neighborhood $\mathrm{Z}(k)$. In this paper, we use a square window $\mathrm{Z}(k)$ centered at $y(k)$. The correlation between variances of neighboring coefficients is assumed to be high and hence $\sigma^2(j) \approx \sigma^2(k)$ for all $j \in \mathrm{Z}(k)$. Then the approximate maximum likelihood (ML) estimator for $\sigma_x^2(k)$ is computed as [51]

$$\hat{\sigma}_x^2(k) = \max\left(0, \frac{1}{G}\sum_{j\in \mathrm{Z}(k)} y^2(j) - \sigma_n^2\right) \tag{4.17}$$

where G is the number of coefficients in $\mathrm{Z}(k)$. Using the exponential prior $f_\sigma(\sigma_x^2) = \lambda e^{-\lambda\sigma_x^2}$, the

approximate *maximum a posteriori* (MAP) estimator of $\sigma_x^2(k)$ is given as [51]

$$\hat{\sigma}_x^2(k) = \max\left(0, \frac{G}{4\lambda}\left[-1 + \sqrt{1 + \frac{8\lambda}{G^2}\sum_{j\in \mathrm{Z}(k)} y^2(j)}\right] - \sigma_n^2\right) \tag{4.18}$$

The parameter λ is required to be estimated for each subband of rearranged LT coefficients and was set equal to the inverse of the standard deviation of the rearranged LT coefficients that were initially denoised using (4.17) and the local Wiener filter estimate. The local Wiener filter estimate of the clean coefficients $x(k)$ is given as [51]

$$\hat{x}(k) = \frac{\hat{\sigma}_x^2}{\hat{\sigma}_x^2 + \sigma_n^2} y(k) \tag{4.19}$$

where σ_n^2 is estimated using (4.8). The local Wiener filtering in LOT domain that uses (4.17) for estimation of variance is referred to as LOT-LWF-ML algorithm. The same filter when it uses (4.18) for estimation of variance is called LOT-LWF-MAP algorithm.

4.3.1 Doubly Local Wiener Filtering in Lapped Transform Domain

The accuracy of variance estimation from the noisy coefficients greatly affects the performance of (4.17). A more accurate estimation of variance can be obtained from the coefficients of a *pilot image* where the *pilot image* is the denoised signal obtained by hard thresholding [26,38]. Shui [40] proposed a doubly local Wiener filtering in the wavelet domain using elliptic directional windows. The main idea in [40] is to obtain an approximately clean signal from one local Wiener filter where the variance is estimated from the observed noisy wavelet coefficients in a local neighborhood and then using the approximate signal as a *pilot image* in the second local Wiener filter to obtain a more accurate estimation of variance.

We investigated the performance of a single local Wiener filter in LT domain (LOT-LWF-ML/MAP). The results (Table 4.5) are discussed in Section 4.3.2. Motivated by the encouraging performance of the single local Wiener filter in the LT domain, we propose to extend this concept to formulate a doubly local Wiener filter in the LT domain. Fig. 4.8 shows the block diagram of the proposed framework for a doubly local Wiener filtering in the LT domain. The first local Wiener filter is performed in Lapped Transform-1 (LT1) domain using (4.19), to produce an approximately noise free image which is then used as a *pilot image* in the second Wiener filter. The local variance estimation is performed using (4.17). The second local Wiener filter in Lapped Transform-2 (LT2)

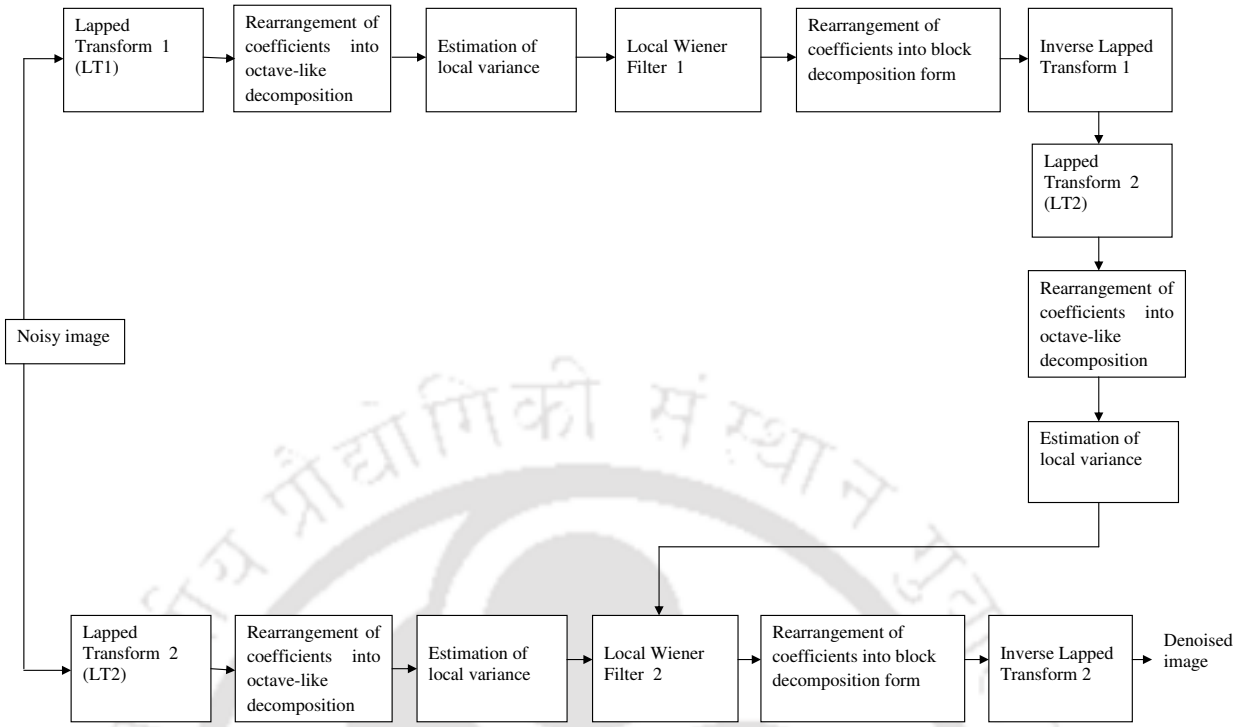

Fig. 4.8: Block diagram of the proposed doubly local Wiener filtering framework in LT domain

domain makes use of the following equation to restore the noisy lapped transform coefficients.

$$\hat{x}(k) = \frac{\hat{\sigma}_{xp}^2(k)}{\hat{\sigma}_{xp}^2(k) + \sigma_n^2} y_{LT2}(k) \tag{4.20}$$

where $y_{LT2}(k)$ are the LT coefficients of the actual noisy image in LT2 domain and $\hat{\sigma}_{xp}^2(k)$ is the signal variance estimated from the pilot image in LT2 domain. The signal variance $\hat{\sigma}_{xp}^2(k)$ is estimated using the following equation

$$\hat{\sigma}_{xp}^2(k) = \max\left(0, \frac{1}{M} \sum_{j \in \mathrm{Z}(k)} \tilde{C}^2(j)\right) \tag{4.21}$$

where $\tilde{C}^2(j)$ is the LT coefficients of the *pilot image* in the LT2 domain. We call the proposed doubly local Wiener filter in LT domain as LTDLWF algorithm.

In [40, 41], the authors demonstrated that the denoising performance can be further improved if two different wavelet bases are used in the wavelet based doubly local Wiener filtering scheme. We study the effect of using five different combinations of LT1 and LT2 pairs on the denoising performance of LTDLWF algorithm for Lena image as shown in Table 4.9. Since LOT(M=8) and

LOT(M=16) or LBT(M=8) and LBT(M=16) show quite different objective and subjective results, they may be used as LT1 and LT2 pairs in the proposed framework shown in Fig. 4.8. Table 4.9 show that the combination of LOT (M=8) as LT1 and LOT (M=16) as LT2 is the best combination and hence used in the proposed LTDLWF algorithm.

4.3.2 Experimental Results

We use center square shaped window of size 3x3 in the proposed algorithms to find the estimates for σ_x^2. Table 4.5 shows the peak signal to noise ratio (PSNR) comparison between the local Wiener filtering algorithms in LT domain and the local Wiener filtering algorithms in wavelet domain. The results show that the local Wiener filtering algorithms in LT domain outperforms wavelet domain LAWMAP and LAWML [51] algorithms in terms of PSNR, for almost all the test images. The LOT based local Wiener filtering schemes show good PSNR improvement for Barbara and Fingerprint images. For Boat image the LOT based local Wiener filtering schemes underperforms the wavelet domain LAWMAP [51] slightly by 0.03-0.1 dB.

Table. 4.5: PSNR (dB) comparison between wavelet domain local Wiener filtering and LT domain Wiener filtering schemes for Lena, Barbara, Fingerprint, Mandrill, Boat and Bridge images.

	Lena (512x512)			
σ_n	10	15	20	25
LAWML(5x5) [51]	34.12	31.93	30.38	29.18
LAWMAP(5x5) [51]	34.28	32.32	30.89	29.92
LOT-LWF-ML (M=8)	34.06	31.92	30.36	29.13
LOT-LWF-ML (M=16)	34.22	32.17	30.69	29.59
LOT-LWF-MAP (M=8)	34.24	32.36	31.01	29.89
LOT-LWF-MAP (M=16)	**34.30**	**32.38**	**31.09**	**30.14**
	Barbara (512x512)			
σ_n	10	15	20	25
LAWML(5x5) [51]	32.51	30.07	28.38	27.09
LAWMAP(5x5) [51]	32.51	30.17	28.57	27.37
LOT-LWF-ML (M=8)	32.56	30.15	28.49	27.18
LOT-LWF-ML (M=16)	32.85	30.48	28.84	27.61
LOT-LWF-MAP (M=8)	32.64	30.29	28.67	27.47
LOT-LWF-MAP (M=16)	**32.90**	**30.66**	**29.09**	**27.97**
	Fingerprint (512x512)			
σ_n	10	15	20	25
LAWML(5x5) [51]	31.30	28.97	27.36	26.15
LAWMAP(5x5) [51]	31.35	29.06	27.55	26.38
LOT-LWF-ML (M=8)	31.43	29.15	27.55	26.35
LOT-LWF-ML (M=16)	31.74	29.42	27.86	26.65
LOT-LWF-MAP (M=8)	31.44	29.26	27.81	26.70
LOT-LWF-MAP (M=16)	**31.76**	**29.50**	**27.91**	**26.78**
	Mandrill (512x512)			
σ_n	10	15	20	25
LAWML(5x5) [51]	30.20	27.64	25.99	24.77
LAWMAP(5x5) [51]	30.17	27.64	25.99	24.84
LOT-LWF-ML (M=8)	30.15	27.63	25.97	24.79
LOT-LWF-ML (M=16)	**30.22**	27.67	26.10	24.84
LOT-LWF-MAP (M=8)	30.15	27.64	25.99	24.83
LOT-LWF-MAP (M=16)	30.21	**27.69**	**26.08**	**24.93**
	Boat (512x512)			
σ_n	10	15	20	25
LAWML(5x5) [51]	32.50	30.36	28.86	27.67
LAWMAP(5x5) [51]	**32.59**	**30.56**	**29.21**	28.09
LOT-LWF-ML (M=8)	32.46	30.28	28.81	27.59
LOT-LWF-ML (M=16)	32.49	30.38	28.91	27.84
LOT-LWF-MAP (M=8)	32.55	30.47	29.10	28.02
LOT-LWF-MAP (M=16)	32.56	30.50	29.16	**28.12**
	Bridge (512x512)			
σ_n	10	15	20	25
LAWML(5x5) [51]	30.54	**28.09**	26.51	25.36
LAWMAP(5x5) [51]	**30.56**	**28.09**	26.56	25.50
LOT-LWF-ML (M=8)	30.46	28.02	26.49	25.36
LOT-LWF-ML (M=16)	30.47	**28.09**	**26.63**	**25.51**
LOT-LWF-MAP (M=8)	30.48	28.04	26.53	25.47
LOT-LWF-MAP (M=16)	30.48	28.05	26.57	25.49

Table 4.6 shows PSNR comparison between Wavelet HMT [14], Contourlet HMT [60], Contourlet Wiener [92], LAWML, LAWMAP, LOT-LWF-ML and LOT-LWF-MAP image denoising algorithms for Lena and Barbara images. Results in Table 4.6 indicate that the proposed LOT-LWF-MAP algorithm outperforms all other algorithms in terms of PSNR. Further, it outperforms the Contourlet domain algorithms by a good margin. The results also indicate that LOT-LWF-MAP algorithm outperforms LAWML and LAWMAP consistently even at high noise levels. Fig. 4.9 show the visual results of Bridge image for LAWMAP and LOT-LWF-MAP (M=16) algorithms. It can be seen from Fig. 4.9 that the proposed method provides images that are of better visual quality than that of LAWMAP method. Table 4.7 show the PSNR comparison between the doubly local Wiener

Table. 4.6: PSNR (in dB) comparison between Contourlet HMT [60], Contourlet Wiener [92] and proposed image denoising scheme based on local Wiener filtering in LT domain

	Lena (512x512)			Barbara (512x512)		
σ_n	30	40	50	30	40	50
Noisy	18.88	16.53	14.63	18.72	16.38	14.48
Wavelet HMT [14]	28.35	27.21	25.89	25.11	24.94	23.71
Contourlet HMT [60]	28.18	27.00	26.04	25.27	24.79	23.74
Contourlet Wiener [92]	28.77	27.47	26.46	26.34	25.04	24.11
LAWML [51]	28.11	26.45	25.18	26.13	24.57	23.42
LAWMAP [51]	29.09	27.85	26.87	26.45	25.13	24.11
LOT-LWF-ML (M=16)	28.17	26.54	25.34	26.55	24.99	23.71
LOT-LWF-MAP (M=16)	**29.28**	**28.00**	**27.03**	**27.04**	**25.72**	**24.67**

filtering in LT domain and various wavelet (orthogonal DWT) based image denoising schemes at different noise levels. Based on the observations given in Table 4.9, we use LOT (M=8) as LT1 and LOT (M=16) as LT2 in the proposed LTDLWF algorithm. The LTDLWF algorithm outperforms several wavelet based image denoising methods as shown in Table 4.7. The LTDLWF algorithm outperforms the well known Gaussian scale mixture (GSM) [61] based method for most of the images like Barbara, Fingerprint, Mandrill and Bridge. For Lena and Boat images, LTDLWF algorithm is slightly inferior to GSM based scheme. The LTDLWF algorithm also outperforms the wavelet based method discussed in [7] for the Barbara, Fingerprint, Mandrill and Bridge images. For Lena and Boat images, the LTDLWF algorithm performs very close to the method discussed in [7]. Further, the proposed LTDLWF algorithm outperforms the wavelet based doubly local Wiener filtering algorithms for the highly textured Barbara image and underperforms for Lena image. It is to be noted that LTDLWF algorithm uses simple 5x5 square windows to estimate the local variances whereas the wavelet domain methods discussed in [40, 41] uses complicated block adaptive windows to estimate the local variances. The LTDLWF algorithm shows very good visual results when compared to the

wavelet domain image denoising schemes. Fig. 4.10 shows the visual results of Barbara image for LTDLWF algorithm. The proposed LTDLWF algorithm provides images that are of improved visual quality than that of Bi-shrink [72] algorithm.

Table 4.8 show the PSNR comparison between the proposed LT domain image denoising schemes based on local Wiener filtering and two previously published results on LT based image denoising. The results show that the proposed local Wiener filtering algorithm consistently outperform the LT domain HMT based method [18] and the LT based method [64] which uses Laplacian mixture distribution to model the global distribution of LT coefficients.

Table. 4.7: PSNR (in dB) comparison between proposed doubly local Wiener filtering in LT domain and several wavelet based image denoising algorithms

	Lena (512x512)				Barbara (512x512)			
σ_n	10	15	20	25	10	15	20	25
LAWML(5x5) [51]	34.12	31.93	30.38	29.18	32.51	30.07	28.38	27.09
LAWMAP(5x5) [51]	34.28	32.32	30.89	29.92	32.51	30.17	28.57	27.37
Ref. [38]	34.50	-	-	30.10	32.90	-	-	27.80
Bi-shrink [72]	34.34	32.42	30.98	29.96	32.13	29.78	28.24	27.03
Arb. Win [21]	34.50	32.50	31.1	30.00	32.70	30.30	28.70	27.50
LCHMM [23]	34.50	32.50	31.20	30.10	33.10	30.80	29.20	28.00
DLWFDW [40]	34.70	32.80	31.50	30.40	33.20	30.90	29.20	28.10
Ref. [41]	**34.92**	**33.04**	**31.71**	**30.66**	**33.39**	31.03	29.43	28.23
GSM [61]	34.66	32.77	31.43	30.39	33.13	30.68	29.03	27.83
Ref. [7]	34.70	32.80	31.42	30.39	33.18	30.83	29.20	27.98
LTDLWF	34.52	32.64	31.31	30.27	33.27	31.03	29.52	28.41
	Fingerprint (512x512)				Mandrill (512x512)			
σ_n	10	15	20	25	10	15	20	25
LAWML(5x5) [51]	31.30	28.97	27.36	26.15	30.20	27.64	25.99	24.77
LAWMAP(5x5) [51]	31.35	29.06	27.55	26.38	30.17	27.64	25.99	24.84
Bi-shrink [72]	30.89	28.57	27.06	25.94	28.73	26.71	25.27	24.19
GSM [61]	31.36	29.04	27.56	26.38	29.91	27.39	25.76	24.59
Ref. [7]	31.75	29.54	28.04	26.91	29.61	27.37	25.87	24.70
LTDLWF	**31.89**	**29.64**	**28.15**	**26.94**	**30.24**	**27.77**	**26.20**	**25.01**
	Boat (512x512)				Bridge (512x512)			
σ_n	10	15	20	25	10	15	20	25
LAWML(5x5) [51]	32.50	30.36	28.86	27.67	30.54	28.09	26.51	25.36
LAWMAP(5x5) [51]	32.59	30.56	29.21	28.12	30.56	28.09	26.56	25.50
Bi-shrink [72]	32.41	30.50	29.10	28.04	29.63	27.48	26.06	25.08
GSM [61]	**32.84**	30.83	29.42	28.36	30.29	27.83	26.35	25.33
Ref. [7]	32.76	**30.83**	**29.47**	**28.42**	30.30	28.02	26.55	25.54
LTDLWF	32.75	30.72	29.36	28.32	**30.55**	**28.14**	**26.66**	**25.64**

Table. 4.8: PSNR (in dB) comparison between local Wiener filtering algorithms in LT domain and two existing LT domain image denoising algorithms

	Lena (512x512)				Barbara (512x512)			
σ_n	7.7	15.5	23.1	33.1	7.7	15.5	23.1	33.1
Noisy	30.42	24.33	20.88	17.72	30.39	24.34	20.85	17.76
[18]	33.80	29.60	27.20	24.90	33.30	29.10	26.60	24.20
[64]	35.00	31.70	29.80	28.20	33.70	29.70	27.60	25.70
LOT-LWF-ML (M=8)	35.41	31.74	29.55	27.49	34.10	29.94	27.66	25.56
LOT-LWF-ML (M=16)	35.52	31.95	29.95	28.07	34.24	30.15	27.96	26.13
LOT-LWF-MAP (M=8)	35.51	32.19	30.28	28.63	34.17	30.09	27.88	25.97
LOT-LWF-MAP (M=16)	35.55	32.28	30.39	28.82	34.39	30.43	28.35	26.52
LTDLWF	**35.77**	**32.49**	**30.65**	**28.98**	**34.77**	**30.91**	**28.78**	**27.04**

Table. 4.9: Performance Comparison (in terms of PSNR) for different combinations of LT1 and LT2 for Lena image corresponding to LTDLWF algorithm

σ_n	10	15	20	25
LOT(M=8)-LOT(M=16)	**34.55**	**32.66**	**31.34**	**30.34**
LOT(M=16)-LOT(M=8)	34.46	32.49	31.21	30.11
LOT(M=8)-LOT(M=8)	34.31	32.39	31.04	29.91
LOT(M=16)-LOT(M=16)	34.39	32.48	31.16	30.20

4.3.3 Concluding Remarks

In this section we considered a local Wiener filtering scheme in LOT domain and a doubly local Wiener filtering framework in the same domain. The low complexity local Wiener filtering in LOT domain outperforms the local Wiener filtering in wavelet transform domain. The encouraging performance of local Wiener filtering in LT domain motivated us to propose a doubly local Wiener filtering framework in the same domain. The proposed doubly local Wiener filtering scheme in LT domain significantly improves the single local Wiener filtering performance both in terms of PSNR and visual quality. The doubly local Wiener filtering in LT domain outperforms several well known wavelet based image denoising methods. As compared to wavelet based doubly local Wiener filter that uses complex elliptic directional windows, the proposed LTDLWF algorithm with simple square shaped windows show comparable performance for the highly textured Barbara image.

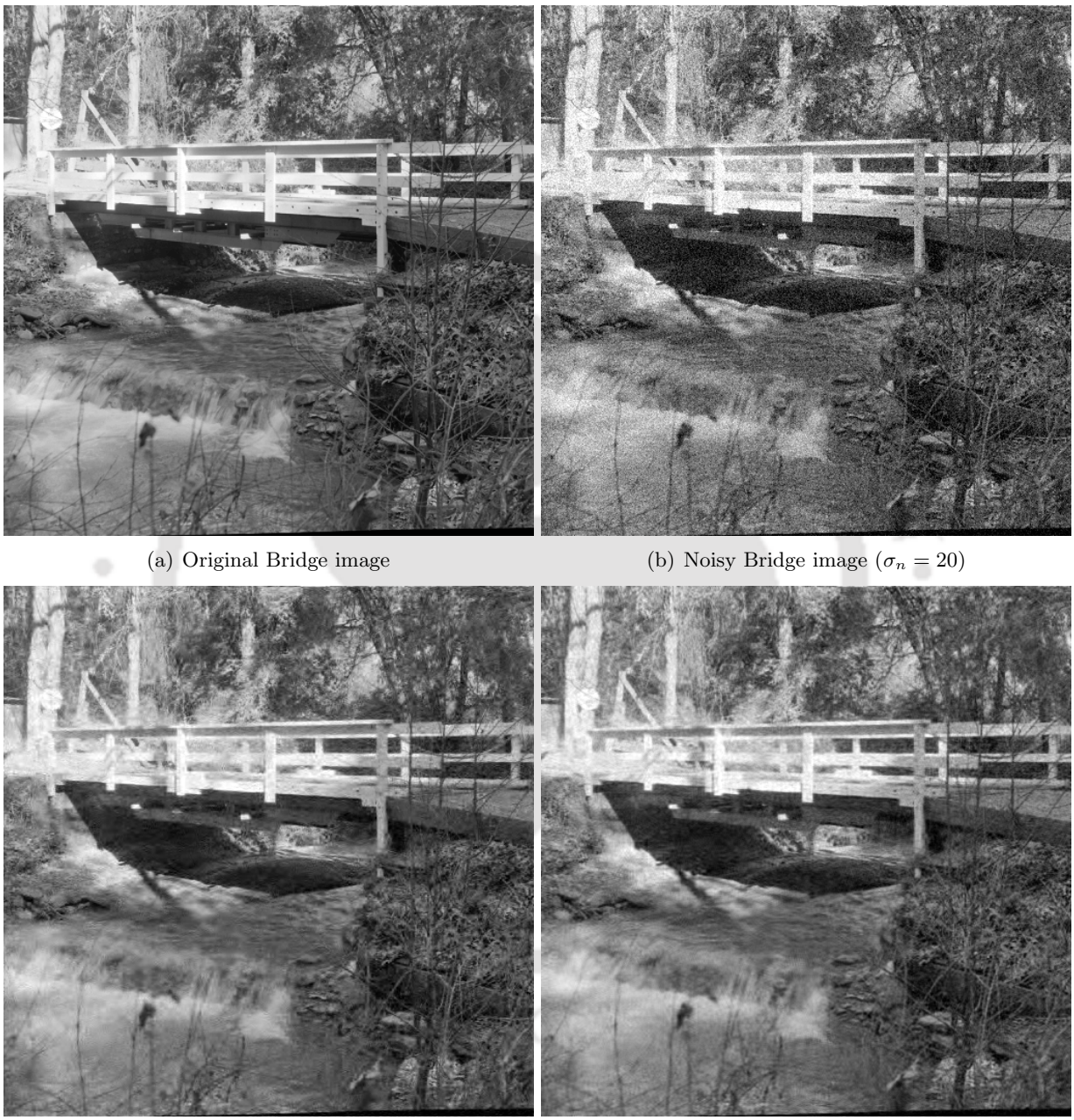

(a) Original Bridge image

(b) Noisy Bridge image ($\sigma_n = 20$)

(c) Denoised using LAWMAP [51] technique

(d) Denoised using LOT-LWF-MAP (M=16) technique

Fig. 4.9: Denoised image of Bridge using LAWMAP and LOT-LWF-MAP algorithms

(a) Original Barbara image

(b) Noisy Barbara image ($\sigma_n = 20$)

(c) Denoised using Bi-shrink [72] technique

(d) Denoised using LOT-LWF-ML (M=16) technique

(e) Denoised using LOT-LWF-MAP (M=16) technique

(f) Denoised using LTDLWF technique

Fig. 4.10: Denoised images of Barbara using local Wiener filtering algorithms in LT domain and Bi-Shrink method [72]

4.4 Image Denoising Based on Laplace Distribution with Local Parameters in Lapped Transform Domain

In this section, we investigate the image denoising performance of LT based on local Laplace prior, and propose to model the rearranged LT coefficients in a subband using the Laplace probability density function (pdf) with local variance. This simple distribution is well able to model the locality and the heavy tailed property of lapped transform coefficients. A *maximum a posteriori* (MAP) estimator using the Laplace probability density function (pdf) with local variance is used for the estimation of noise free lapped transform coefficients.

Many wavelet based image denoising schemes [21, 23, 38, 51] assume local distribution of the transform coefficients to be Gaussian with spatially varying variance and employ linear minimum mean square error (MMSE) estimator locally to restore the noisy coefficients. In [24, 53, 62], the Laplace prior has been used for the statistical modeling of wavelet transform coefficients. Recently, the local Laplace prior has been used for modeling of Steerable Pyramid coefficients [62]. Fig. 4.11(a), 4.12(a) and 4.13(a) respectively show the histogram of a specific subband of rearranged LOT coefficients for Fingerprint, Mandrill and Bridge images. It is observed that the histogram of the coefficients in a subband of rearranged LOT coefficients has a sharp peak around zero with its tails decaying to zero at a much slower rate as compared to the Gaussian pdf. The same figures also indicate that Laplace distribution better fits the histogram of coefficients. The histograms when plotted in log domain (Fig. 4.11(b), 4.12(b) and 4.13(b)) clearly brings out this point whereas Laplace pdf gives a better fit to the observations, Gaussian pdf fails at the tails. In this section,

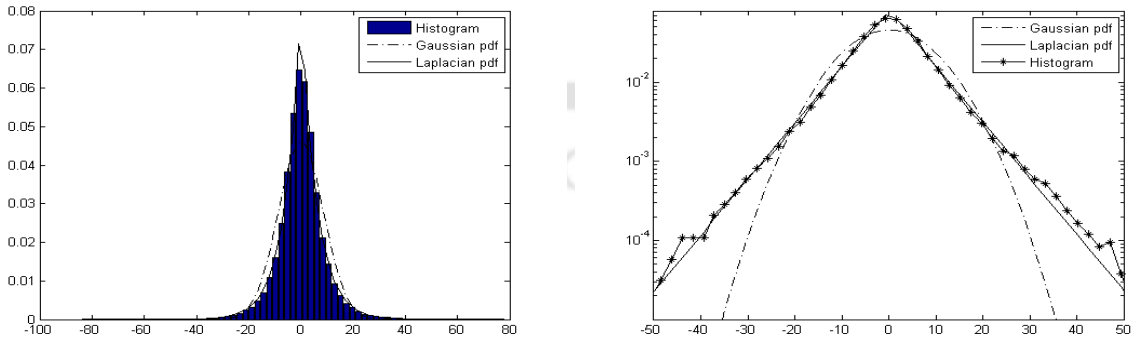

(a) (b)

Fig. 4.11: (a) The Gaussian and Laplacian pdf fitted to the histogram of the rearranged LT coefficients in a particular subband of Fingerprint (512x512) image (b) The histogram, Gaussian and Laplace pdf in the log domain.

we model the rearranged LT coefficients in a subband using Laplace pdf with local variance. The

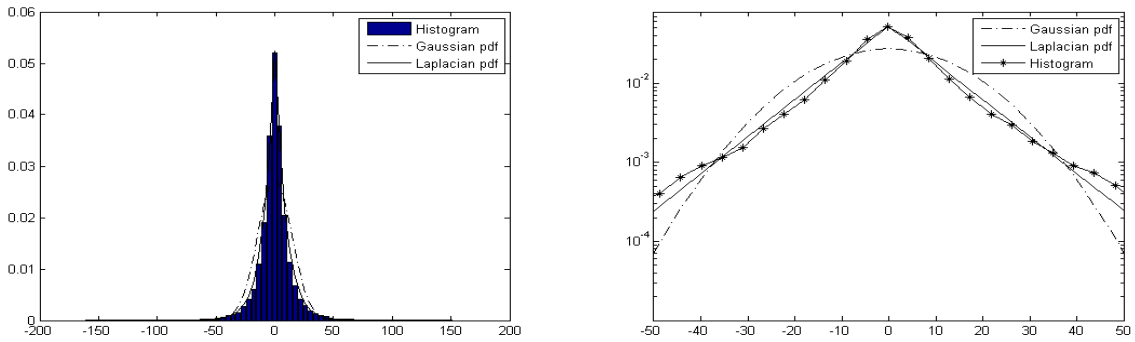

(a) (b)

Fig. 4.12: (a) The Gaussian and Laplacian pdf fitted to the histogram of the rearranged LT coefficients in a particular subband of Mandrill (512x512) image, (b) The histogram, Gaussian and Laplace pdf in the log domain.

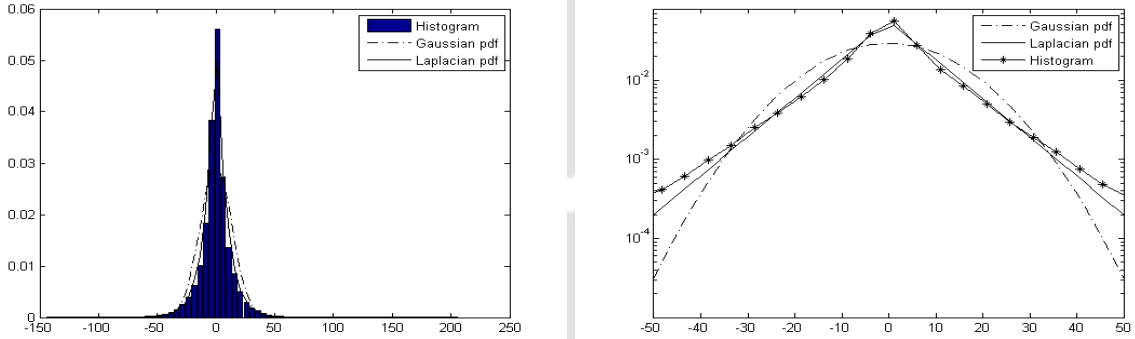

(a) (b)

Fig. 4.13: (a) The Gaussian and Laplacian pdf fitted to the histogram of the rearranged LT coefficients in a particular subband of Bridge (512x512) image, (b) The histogram, Gaussian and Laplace pdf in the log domain.

MAP estimator using this local Laplace prior is used for the estimation of noise free LT coefficients. Fig. 4.14 shows the block diagram of the proposed LT based image denoising method. We assume that the image is corrupted by additive white Gaussian noise with variance σ_n^2. The orthogonal LOT coefficients of the noisy image are given by

$$y(k) = x(k) + n(k) \tag{4.22}$$

where *x(k)* denotes the clean LT coefficients and *n(k)* is the additive white Gaussian noise. When we use a MAP estimator to estimate *x(k)* from the noisy observation *y(k)*, we have [63]

$$\hat{x}(k) = \arg\max_{x(k)} P_{x(k)|y(k)}(x(k)|y(k)) \tag{4.23}$$

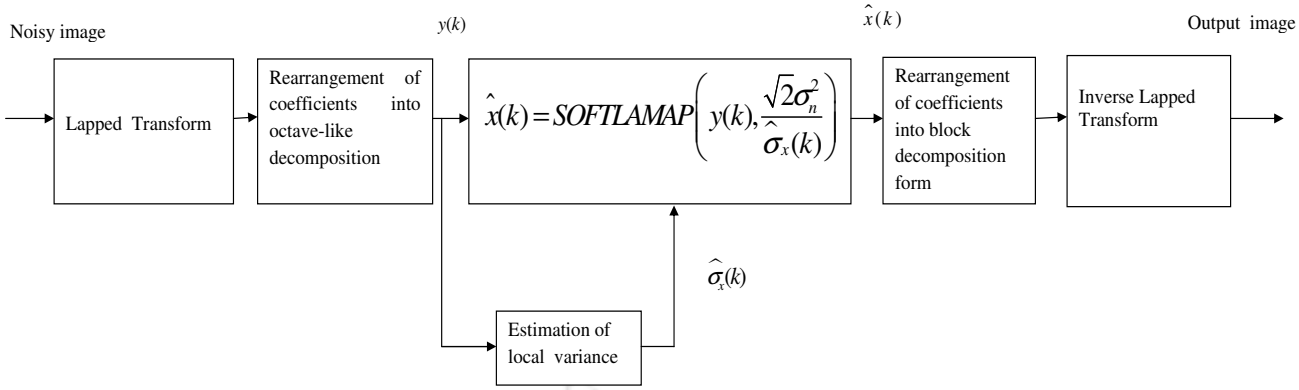

Fig. 4.14: Block diagram of the proposed LT based image denoising method based on local Laplace prior

Equation (4.23) can also be written as

$$\hat{x}(k) = \arg\max_{x(k)} \left[P_n(y(k) - x(k)) P_{x(k)}(x(k)) \right] \tag{4.24}$$

with

$$p_n(n(k)) = \frac{1}{\sqrt{2\pi}\sigma_n} \exp\left[-\frac{n^2(k)}{2\sigma_n^2} \right] \tag{4.25}$$

Substituting (4.25) in (4.24), we have

$$\hat{x}(k) = \arg\max_{x(k)} \left[-\frac{(y(k) - x(k))^2}{(2\sigma_n^2)} + f(x(k)) \right] \tag{4.26}$$

where $f(x_k) = \log\left(P_{x(k)}(x(k))\right)$. Thus, the MAP estimate of *x(k)* is achieved by setting the derivative with respect to $x(k)$ equal to zero

$$\frac{y(k) - \hat{x}(k)}{\sigma_n^2} + f'(x(k)) = 0 \tag{4.27}$$

In this section, we model the LT coefficients using Laplace pdf with local variance, thus

$$P_{x(k)}(x(k)) = \frac{1}{\sigma_x(k)\sqrt{2}} \exp\left(-\frac{\sqrt{2}\,|x(k)|}{\sigma_x(k)} \right) \tag{4.28}$$

Taking logarithm of both sides of (4.28), we have

$$f(x(k)) = -\log\left(\sigma_x(k)\sqrt{2}\right) - \frac{\sqrt{2}\,|x(k)|}{\sigma_x(k)} \tag{4.29}$$

We have

$$f'(x(k)) = -\frac{\sqrt{2}}{\sigma_x(k)} sign(x(k)) \tag{4.30}$$

So,

$$y(k) = \hat{x}(k) + \frac{\sqrt{2}\sigma_n^2}{\sigma_x(k)} sign\left(\hat{x}(k)\right) \tag{4.31}$$

The above equation can also be written as

$$\hat{x}(k) = sign(y(k)) \left(|y(k)| - \frac{\sqrt{2}\sigma_n^2}{\sigma_x(k)} \right)_+ \tag{4.32}$$

An operation $(b)_+$ may be defined as

$$(b)_+ = \begin{cases} 0, b < 0 \\ b, otherwise \end{cases} \tag{4.33}$$

We define a $SOFTLAMAP$ operator [62, 63] as

$$SOFTLAMAP(p, \eta) = sign(p)(|p| - \eta)_+ \tag{4.34}$$

Now, (4.32) can be written as

$$\hat{x}(k) = SOFTLAMAP\left(y(k), \frac{\sqrt{2}\sigma_n^2}{\sigma_x(k)} \right) \tag{4.35}$$

For each noisy LOT coefficient, an estimate of $\sigma_x^2(k)$ is formed based on its local neighborhood $\mathrm{Z}(k)$. In this paper, we use a square window $\mathrm{Z}(k)$ centered at *y(k)*. The estimate for $\sigma_x^2(k)$ is given as [51]

$$\hat{\sigma}_x^2(k) = \max\left(0, \frac{1}{G} \sum_{j \in \mathrm{Z}(k)} y^2(j) - \sigma_n^2 \right) \tag{4.36}$$

where G is the number of coefficients in $\mathrm{Z}(k)$.

4.4.1 Experimental Results

We use center square shaped window of size 5x5 in the proposed algorithm (referred to as LOT-Lap algorithm) to find the estimate of σ_x^2. Table 4.10 shows the PSNR comparison between the proposed LT based image denoising scheme based on local Laplace prior and two previously published results on LT based image denoising. The results show that the proposed LOT-Lap algorithm outperforms

the LT domain HMT based method [18] and a LT based method which uses Laplacian mixture distribution to model the global distribution of LT coefficients [64].

We call the implementation of local Laplace prior in wavelet domain as WT-Lap [62, 63, 71]. We used an orthogonal wavelet transform with four levels of decomposition and Daubechies length-8 wavelet for the implementation of WT-Lap algorithm. Table 4.11 shows the PSNR comparison

Table. 4.10: PSNR (in dB) comparison between proposed LOT [M=8] based image denoising scheme and two existing LT based image denoising schemes

	Lena (512x512)				Barbara (512x512)			
σ_n^2	Noisy	[18]	[64]	LOT-Lap	Noisy	[18]	[64]	LOT-Lap
7.7	30.42	33.80	35.0	**35.32**	30.39	33.30	33.70	**34.20**
15.5	24.33	29.60	31.70	**32.03**	24.34	29.10	29.70	**30.23**
23.1	20.88	27.20	29.80	**30.01**	20.85	26.60	27.60	**28.05**
33.1	17.72	24.90	28.20	**28.29**	17.76	24.20	25.70	**26.13**

between the proposed LOT-Lap denoising scheme and Bayes-shrink [12], LAWML [51] and WT-Lap algorithms. The results indicate that proposed scheme with local Laplace prior outperforms wavelet based Bayes-shrink and WT-Lap for almost all the test images. The PSNR improvement is especially encouraging in case of Barbara and Fingerprint images. When compared to wavelet based LAWML [51], the LOT-Lap scheme outperforms the LAWML scheme for Lena, Barbara, Boat and Fingerprint images. For Mandrill and Bridge images the LOT-Lap method does not perform well when compared with LAWML scheme. Fig. 4.15 and 4.16 show the visual results for Lena and Barbara images respectively. From these figures it can be seen that the proposed method provides images that are of good visual quality.

4.4.2 Concluding Remarks

In this section we model the rearranged LT coefficients in a subband using Laplace probability density function (pdf) with local variance. This simple distribution is able to model the locality and the heavy tailed property of lapped transform coefficients. A *maximum a posteriori* (MAP) estimator using the Laplace pdf with local variance is used for the estimation of noise free lapped transform coefficients. The proposed low complexity image denoising method outperforms two existing LT based image denoising schemes. Further this method consistently outperforms the method where the local Laplace prior is used in wavelet domain.

Table. 4.11: PSNR (in dB) comparison between proposed LOT [M=8 and M=16] based image denoising scheme and several wavelet based image denoising schemes

	Lena (512x512)			
σ_n	10	15	20	25
Bayes-shrink [12]	33.23	31.20	29.95	28.99
LAWML [51]	**34.12**	31.93	30.38	29.18
WT-Lap	34.04	32.05	30.69	29.64
LOT-Lap (M=8)	34.06	32.20	30.82	29.69
LOT-Lap (M=16)	34.09	**32.26**	**30.85**	**29.76**
	Barbara (512x512)			
σ_n	10	15	20	25
Bayes-shrink [12]	31.10	28.72	27.12	25.90
LAWML [51]	32.51	30.07	28.38	27.09
WT-Lap	32.19	29.75	28.10	26.89
LOT-Lap (M=8)	32.69	30.43	28.83	27.57
LOT-Lap (M=16)	**32.89**	**30.68**	**29.18**	**28.06**
	Boat (512x512)			
σ_n	10	15	20	25
Bayes-shrink [12]	31.89	29.76	28.33	27.25
LAWML [51]	**32.50**	**30.36**	28.86	27.67
WT-Lap	32.30	30.28	28.87	27.77
LOT-Lap (M=8)	32.38	**30.35**	**28.95**	**27.86**
LOT-Lap (M=16)	32.32	30.26	**28.94**	27.84
	Mandrill (512x512)			
σ_n	10	15	20	25
Bayes-shrink [12]	29.52	26.84	25.19	24.01
LAWML [51]	**30.20**	**27.64**	**25.99**	**24.77**
WT-Lap	29.66	27.10	25.42	24.23
LOT-Lap (M=8)	29.72	27.20	25.54	24.40
LOT-Lap (M=16)	29.72	27.21	25.58	24.43
	Bridge (512x512)			
σ_n	10	15	20	25
Bayes-shrink [12]	30.00	27.52	25.96	24.91
LAWML [51]	**30.54**	**28.09**	**26.51**	**25.36**
WT-Lap	30.05	27.59	26.03	24.97
LOT-Lap (M=8)	30.06	27.56	26.09	25.04
LOT-Lap (M=16)	29.97	27.53	26.04	25.05
	Fingerprint (512x512)			
σ_n	10	15	20	25
Bayes-shrink [12]	30.98	28.73	27.21	26.09
LAWML [51]	31.30	28.97	27.36	26.15
WT-Lap	30.77	28.55	27.02	25.86
LOT-Lap (M=8)	31.13	28.93	27.38	26.17
LOT-Lap (M=16)	**31.45**	**29.15**	**27.55**	**26.39**

(a) Original Lena image

(b) Noisy Lena image ($\sigma_n = 20$)

(c) Denoised using Proposed (M=8)

(d) Denoised using Proposed (M=16)

Fig. 4.15: Denoised images of Lena using proposed LT based denoising scheme based on local Laplace prior

(a) Original Barbara image

(b) Noisy Barbara image ($\sigma_n = 20$)

(c) Denoised using Proposed (M=8)

(d) Denoised using Proposed (M=16)

Fig. 4.16: Denoised images of Barbara using proposed LT based denoising scheme based on local Laplace prior

Chapter 5

Blocking Artifacts Reduction in Lapped Transform Domain

The block based DCT is the most important basic component of many image and video compression standards like JPEG and MPEG as its performance is close to that of Karhunen-Loeve transform (KLT) which is optimal in the mean square error sense [33]. In block DCT based image compression scheme the input image is divided into 8x8 pixel blocks and the DCT is applied to each block separately. For the minimization of distortion under a given bit allocation, more number of bits are allocated to the DC and higher energy AC coefficients while lesser number of bits are allocated to the low energy AC coefficients. At low bit rates, the main problem in block DCT based image compression schemes is that the decoded images exhibit visually annoying artifacts known as the blocking artifacts. The visually noticeable changes in the pixel values along the block boundaries is the blocking artifacts. As a result of coarse quantization, ringing artifacts is produced near strong edges due to truncation of high frequency DCT coefficients. The procedures to reduce the blocking and ringing artifacts are respectively known as deblocking and deringing procedures. Fig. 5.1(a) shows the original Lena image and Fig. 5.1(b) shows the JPEG compressed image with a quality factor (Q_f) of 6. The annoying artifacts are closely visible in the compressed image. The main challenge in image deblocking problem is to smooth out the block discontinuities without smoothening the true edges, textures and other important details in the original image.

Motivated by the encouraging image denoising performance of LTs discussed in the last chapter, we present two efficient image deblocking methods which utilize the good denoising property of LTs to reduce the blocking artifacts in LT domain for JPEG compressed images. Both methods use the octave-like rearrangement of LT coefficients discussed in Chapter 4. The first method is based on the soft thresholding of high frequency LT coefficients in different subbands using a global threshold. The

threshold is adaptive to the quantization table used during the compression process. The proposed method gives significant reduction in the mean square error level and also shows good subjective improvement over the image with blocking artifacts. The second method is based on combined LT and bilateral filtering. The local Wiener filtering concept in LT domain is used to smooth out the blocking artifacts and adaptive bilateral filtering in time domain is used to reduce the ringing artifacts. This method shows excellent objective and subjective improvements over the image with blocking and ringing artifacts and outperforms several well known state of the art image deblocking schemes both in terms of PSNR and structural similarity (SSIM) index [80] results.

Section 5.1 presents a review of several image deblocking schemes reported in the literature. Section 5.2 explains the proposed LT domain image deblocking scheme based on soft thresholding along with the experimental results. Section 5.3 describes the proposed image deblocking scheme based on combined LT and adaptive bilateral filtering along with the experimental results.

(a) (b)

Fig. 5.1: (a) Original Lena image, (b) JPEG compressed image (Q=6)

5.1 Literature Review

Many approaches have been proposed to eliminate the blocking artifacts. Reeve and Lim [65] reduced the blocking artifacts using a 3x3 Gaussian filter at the block boundaries. The main problem with this simple method is that the true edges at the block boundaries may also get blurred. Minami and Zakhor [52] proposed a method to reduce the blocking artifacts by minimizing a criterion called mean squared difference of slope (MSDS). The projection onto convex sets (POCS) algorithms [57, 86–88]

have shown good results but the main problem with the POCS methods is their iterative nature and the high computational complexity. Kim et al [39] proposed a wavelet based image deblocking method which is applied only to the neighborhood of each boundary in the wavelet transform at the first and the second scales. Their main intention was to remove the blocking component which shows stepwise discontinuities at block boundaries. They classified the block boundaries into one of the shade region, the smooth edge region and the step edge region. According to classifications the threshold values are selected adaptively. Xu et al. [84] proposed a method to reduce the blocking artifacts in discrete Hadamard transform (DHT) domain. They determine the block activities in the DHT domain to classify the smooth and coarse regions and according to the block activities the blocking artifacts are adaptively filtered. Wu et al. [81] proposed a wavelet based postprocessing technique to remove the blocking artifacts based on soft thresholding. Jang et al. [34] proposed an iterative image deblocking algorithm which uses a minimum mean square error (MMSE) filter in the wavelet domain. The MMSE filtering in wavelet domain and the projection onto a convex set of quantization constraint are performed alternately and iteratively. The methods discussed in [30, 83] use an overcomplete wavelet representation to reduce the blocking artifacts. These methods [30, 83] may not perform well for images with large portions of textures. In [42], an overcomplete wavelet based image deblocking algorithm for reducing the blocking and ringing artifacts was proposed. Their scheme exploits the fact that the block discontinuities are constrained by the dc quantization interval of the quantization table as well as the behavior of wavelet modulus maxima evolution across wavelet scales to derive appropriate threshold maps at different wavelet scales. The behavior of ringing artifacts in wavelet domain is exploited by the authors. Averbuch et al. [2] used weighted sums of pixel quartets which are symmetrically aligned to the block boundaries to suppress the blocking artifacts. The image deblocking scheme based on pointwise shape adaptive DCT (SA-DCT) [25] has shown excellent results in suppressing both blocking and ringing artifacts. Zhai et al. [89] proposed a image deblocking scheme through post filtering in shifted windows of image blocks for JPEG compressed images. In [90], Zhang et al proposed an image deblocking scheme based on adaptive bilateral filter where texture regions and block boundary discontinuities are first detected and based on that the bilateral filter parameters are selected.

5.2 Blocking Artifacts Reduction in LT Domain Based on Soft Thresholding

A simple yet effective image deblocking scheme is proposed in this section for block DCT compressed images based on the soft thresholding of high frequency rearranged LT coefficients in different sub-bands. The scheme is non linear and has very low computational complexity. We demonstrate that the optimal measured threshold has a strong relationship with the JPEG image *Quality factor* Q_f and also with the average of first 3x3 values from the quantization table. The JPEG image *Quality factor* can be computed from the quantization table which is available at the decoding end.

5.2.1 Image Enhancement Based on Soft Thresholding of LT coefficients

In the proposed image enhancement problem, the model is given as

$$y_t = x_t + \eta_t \tag{5.1}$$

where the degradation due to the quantization process is modeled as some additive noise η_t and y_t is the decompressed form of the original image x_t. The main aim of image enhancement here is to find an estimate $\widehat{x_t}(y_t)$ of the original uncompressed image through a scheme which smoothly reduces the effects of η_t on y_t, while preserving the important features of y_t as much as possible. If the distribution of η_t is Gaussian, in that case it is uncorrelated both spatially and with x_t and hence obtaining x_t from y_t becomes a statistical estimation problem. The main motive of restoration problem is to minimize the value of $\sup_{x_t \in X_t} \|\widehat{x_t}(y_t) - x_t\|$. If LOT and LOT^{-1} respectively represent the forward and inverse lapped orthogonal transform operations and the requirement is to maintain the smoothness of the original signal or in other words one want to avoid spurious oscillations, then the following condition must be satisfied [27]

$$|LOT\widehat{x_t}(y_t)| \leq |LOTx_t| \tag{5.2}$$

The estimation of original image $\widehat{x_t}(y_t)$ which satisfies the smoothing condition given in (5.2) is obtained by applying soft thresholding in the orthogonal transform domain where the threshold depends on the variance of η_t [16]. The image can be restored by the following equation

$$\widehat{x_t}(y_t) = LOT^{-1} S_{T_h}(LOTy_t) \tag{5.3}$$

where S_{T_h} is a non linear soft thresholding operator which is defined as

$$S_{T_h}(g) = sign(g)(|g| - T_h)_+ = \begin{cases} g - T_h, g > T_h \\ 0, g \leq T_h \\ g + T_h, g < -T_h \end{cases} \tag{5.4}$$

where T_h is the threshold which is estimated from the observed image. An important feature of this method is that the spurious oscillations are avoided and the important features in y_t can be preserved [16].

In the proposed problem of image enhancement, the noise η_t may be correlated spatially and also with x_t. So the statistical assumptions regarding η_t may not be valid. In spite of this, the algorithm can still be successfully applied for the reason that the orthogonal LT may whiten the data and even if η_t is correlated, $LT\eta_t$ might not be [27].

5.2.2 Proposed Soft Thresholding Algorithm

Donoho et al. [16] proposed the soft thresholding method for reducing the additive white Gaussian noise from the natural images, we use the same soft thresholding method for reducing the blocking artifacts. Fig. 5.2 shows the block diagram of the proposed scheme. The major challenge here is to

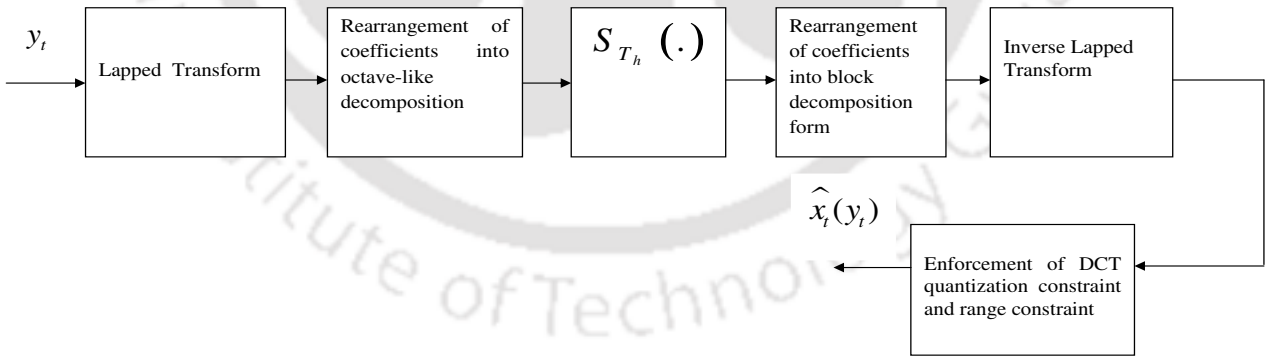

Fig. 5.2: Block diagram of the proposed soft thresholding based image deblocking scheme

determine a threshold which can effectively smooth out the blocking artifacts without blurring the image details.

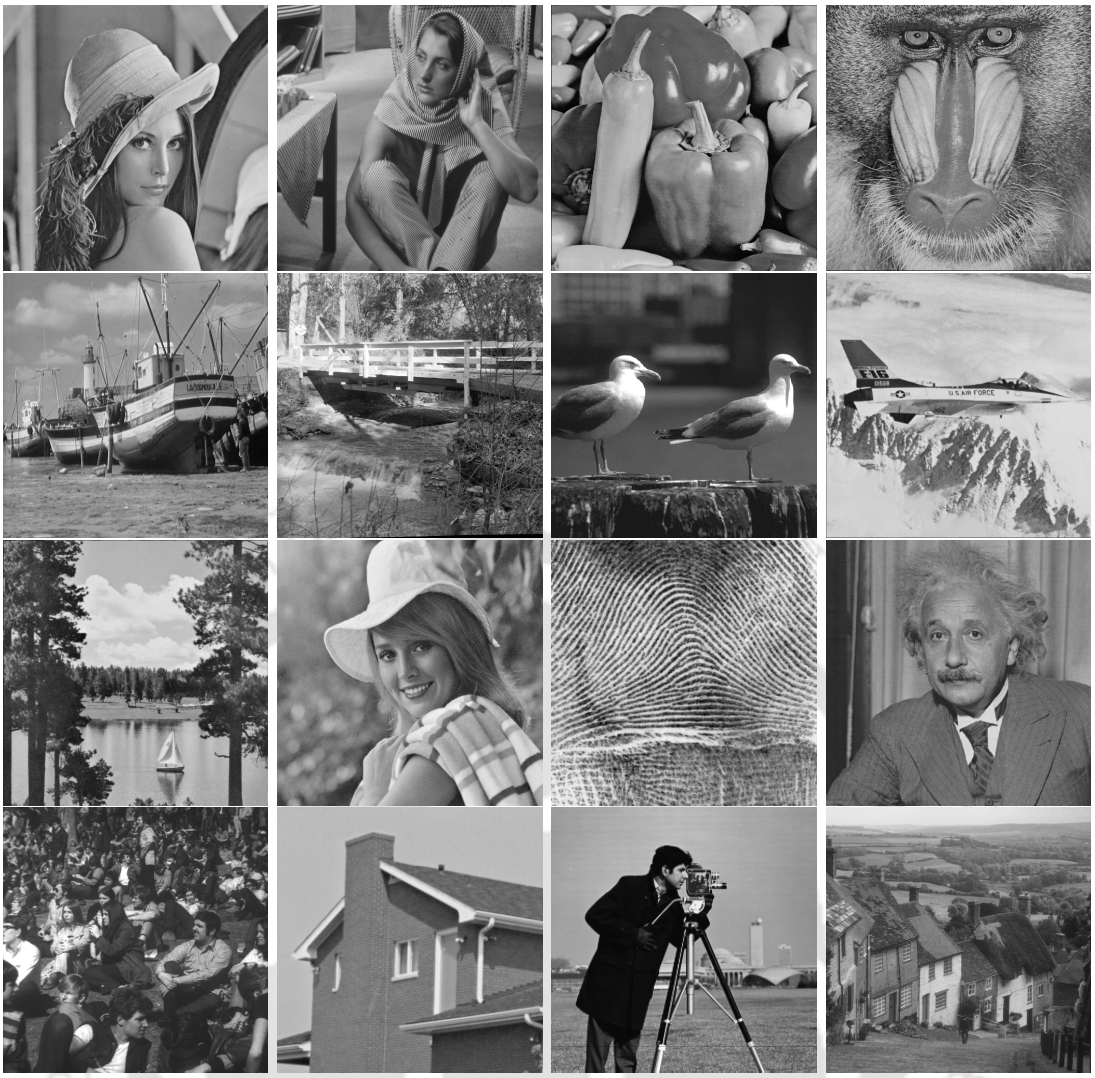

Fig. 5.3: Test images used in experiments (from top-left to bottom- right): Lena, Barbara, Peppers, Mandrill, Boats, Bridge, Birds, Airplane, Sailboat, Elaine, Fingerprint, Einstein, Crowd, House, Cameraman, Goldhill

Determination of the soft threshold value

- **Relation between experimentally observed 'optimal' threshold and JPEG image Quality factor**:

  The original training images Lena, Barbara, Peppers, Mandrill, Boats, Bridge, Birds, Airplane, Sailboat and Elaine shown in Fig. 5.3 are compressed with a standard JPEG coder with image quality factor Q_f from 1 to 50. The soft threshold T_h that offers the highest PSNR for each image at different Q_f is determined. These optimal soft threshold values are then plotted for different image Q_f as shown in Fig. 5.4. The scatter plot shows strong correlation between the soft threshold and the image quality factor Q_f. The data when fitted with a one term

exponential model gives the threshold T_h as

$$T_h\left(Q_f\right) = a\exp\left(bQ_f\right) \tag{5.5}$$

where a=28.71 and b=-0.09761. Fig. 5.4 show that one term exponential does not provide good fit to the given scatter plot.

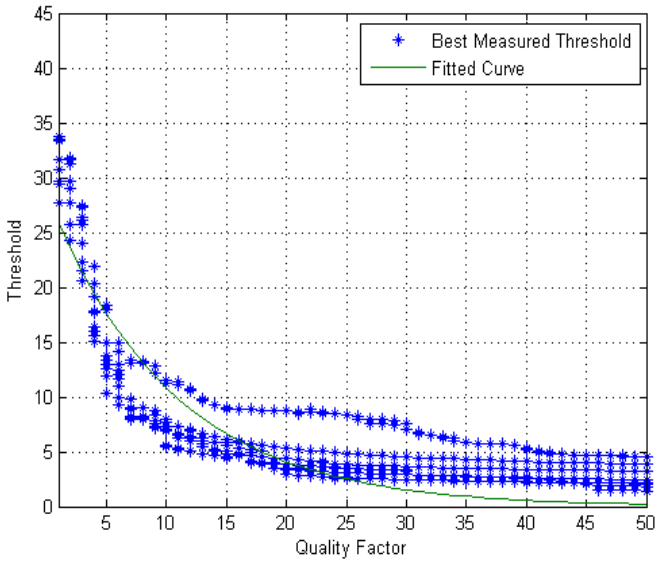

Fig. 5.4: Scatter plot of best measured threshold versus quality factor Q_f and curve fitting using one term exponential

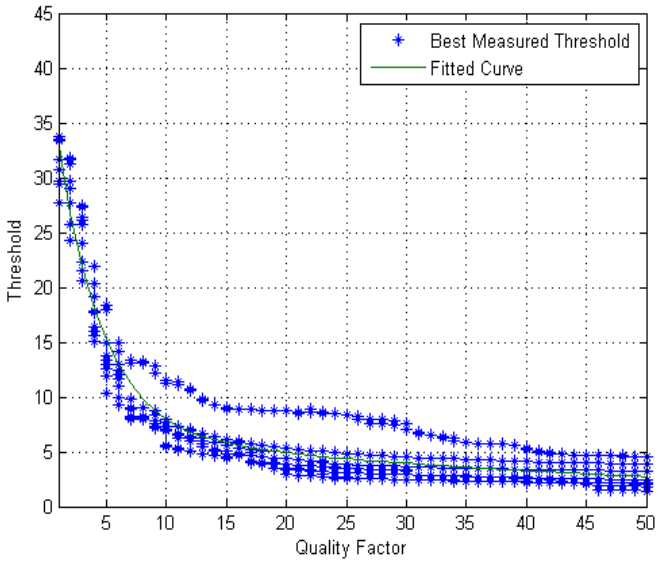

Fig. 5.5: Scatter plot of best measured threshold versus quality factor Q_f and curve fitting using two term exponential

The data when fitted with a two term exponential model gives the threshold T_h as

$$T_h(Q_f) = a\exp(bQ_f) + c\exp(dQ_f) \tag{5.6}$$

where a=34.74, b=-0.2724, c=6.877, d=-0.0185. Fig. 5.5 show that the two term exponential model provides a good fit to the given scatter plot.

- **Relation between experimentally observed 'optimal' threshold and Q_{av}:**

We further demonstrate that the experimentally observed 'optimal' threshold also has a high correlation with the average of first 3x3 values from the quantization table Q_{av}. We found that the experimentally observed optimal threshold is approximately linearly related to the Q_{av}. Since (5.6) is a function of JPEG image Quality factor(Q_f), it is useful only for the JPEG compressed images. The threshold proposed next is useful for any block DCT compressed (JPEG and non JPEG) images.

With the same experimental results obtained in the last section, we plot the experimentally observed optimal thresholds at different Q_{av} values as shown in Fig. 5.6. Q_{av} represents the average of the first 3x3 values of the quantization matrix Q used in compression procedure:

$$Q_{av} = \frac{1}{9}\sum_{i,j=1}^{3} Q_{i,j} \tag{5.7}$$

Note that any Q_f value i.e any quantization matrix used in JPEG compression results in different Q_{av} values. The scatter plot show that measured optimal threshold can be approximately linearly related to Q_{av}. Smaller Q_f which represents higher compression corresponds to larger values of Q_{av} and larger values of Q_f which indicates lower compression corresponds to smaller values of Q_{av}. The data when fitted with a linear polynomial gives the threshold T_h as

$$T_h(Q_{av}) = p1.Q_{av} + p2 \tag{5.8}$$

where $p1$=0.1072 and $p2$=1.362. From the simulation results discussed in next section, we observe that the results are not very sensitive to the fitting errors and the fitted curve can be considered for a wide range of JPEG compressed images with different quantization tables. The results presented (Section 5.2.4) confirm that the fitted curve can also be used with wide range of different block DCT quantization tables and performs well for images from inside and

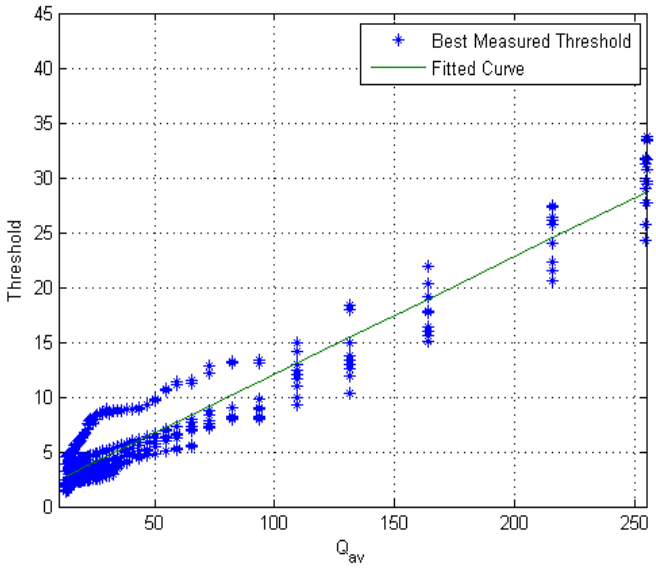

Fig. 5.6: Scatter plot of best measured threshold versus Q_{av} and curve fitting using linear polynomial

outside the training sets. We use (5.8) in the proposed algorithm to calculate the global soft threshold value, so that it can be used with any JPEG compressed images and other block DCT compressed images.

Finally the DCT quantization constraint and the range constraint is imposed onto the filtered output.

5.2.3 DCT Quantization Constraint and Range Constraint

In the POCS based deblocking schemes, the final deblocked image is constrained with the quantization constraint set. The quantization constraint found from the quantization table restricts the value of the DCT coefficients to be within the quantization interval. The deblocked image should satisfy the quantization constraint, to be consistent with the original image. The image $\tilde{d}$ (the output of inverse Lapped transform block in Fig. 5.2) generally do not satisfy the quantization constraint, so $\tilde{d}$ is projected onto the quantization constraint set to obtain a deblocked image which is consistent with the original image. Let $\tilde{m}$ represents the set of DCT coefficients of image $\tilde{d}$. The (u,v)th DCT coefficient at block position (x,y) is modified as follows

$$\tilde{m}_{x,y}(u,v) = \begin{cases} C_{\max}(u,v), if \tilde{m}_{x,y}(u,v) > C_{\max}(u,v) \\ C_{\min}(u,v), if \tilde{m}_{x,y}(u,v) < C_{\min}(u,v) \\ \tilde{m}_{x,y}(u,v), otherwise \end{cases} \tag{5.9}$$

where

$C_{\max}(u,v) = (q_{x,y}(u,v) + 0.5)\Delta(u,v)$

$C_{\min}(u,v) = (q_{x,y}(u,v) - 0.5)\Delta(u,v)$

for $u = 0, ...7, v = 0, ...7, x = 0, ...$(row / 8)-1, $y = 0, ...$(col / 8)-1.

The quantized coefficients (q) that is available at the decoder input is given by

$$q_{x,y}(u,v) = round\left[\frac{m_{a,b}(u,v)}{\Delta(u,v)}\right] \tag{5.10}$$

where m is the original image DCT coefficients and $\Delta(u,v)$ represents the quantization interval of the (u,v)th DCT coefficient. It is to be noted that it is q (not m) which is available at the decoder input.

A narrow quantization constraint set discussed in [58], produces better results in terms of mean square error. For narrow quantization constraint set, the $C_{\max}(u,v)$ and $C_{\min}(u,v)$ is given by

$$\begin{aligned} C_{\max}(u,v) &= (q_{x,y}(u,v) + \xi_1)\Delta(u,v) \\ C_{\min}(u,v) &= (q_{x,y}(u,v) - \xi_2)\Delta(u,v) \end{aligned} \tag{5.11}$$

where $0 < \xi_1, \xi_2 \leq 0.5$ We use $\xi_1 = 0.3$ and $\xi_2 = 0.3$ for the experiments. The inverse block DCT with the modified coefficients is performed to obtain the deblocked image. Finally the range constraint is applied on this image. Since the 8 bit original images used in the experiments have values in the range of (0-255), the deblocked image must also satisfy this range. Any value outside the range of (0-255) is projected into this given range.

5.2.4 Experimental Results

The proposed method has been tested on various test images compressed by the JPEG standard and the quantization tables Q1, Q2 and Q3 (Fig. 5.7) which are commonly used in literature for simulating various types of block DCT compression. The test images used in experiments are shown in Fig. 5.3. The images Lena, Barbara, Peppers, Mandrill, Boats, Bridge, Birds, Airplane, Sailboat and Elaine were used in training stage. The baseline IJG JPEG implementation [28] is used for the simulation of all JPEG experiments presented in this chapter. We use (5.8) to determine the threshold value for soft thresholding the rearranged LT coefficients in all the detailed subbands. In Table 5.1, the PSNR results of the proposed method is compared with the best PSNR results obtained by any of the methods [2] [13] [69] [88] [10] [31] as reported in [2]. Table 5.1 indicates that the proposed

method outperforms the best results reported in [2] for Lena and Barbara images and performs very close for the Peppers image. The PSNR improvement in the proposed scheme over the best results reported in [2] for Barbara image is approximately 0.45 dB and for Lena image it is approximately 0.2dB. In order to make a fair comparison with the results reported in [2], the Peppers image used in Table 5.1 corresponds to green channel of the RGB color Peppers image. In Table 5.2, the PSNR results of the proposed method is compared with the results of several well known decimated and non-decimated wavelet based image deblocking schemes [30, 42, 81, 83]. The method discussed in [81] is based on orthogonal wavelet transform and those in [30, 42, 83] are based on overcomplete wavelet transform. Table 5.2 shows that the proposed deblocking scheme outperforms [30, 81, 83] for all test images and performs very close to [42] for Lena and Peppers images. For the Barbara image, it outperforms by approximately 0.4 to 0.61dB. This suggests that the fitted curve in Fig. 5.6 may be considered for deblocking purpose for a wide range of quantization tables that include both JPEG and non-JPEG tables. Table 5.3 shows PSNR results for various test images compressed by JPEG standard at various quality factors (Q_f). Tables 5.1, 5.2 and 5.3 indicate that the images processed by the proposed scheme show significant increase in PSNR over the blocky image. The visual results shown in Fig. 5.8 and 5.9 indicate that the proposed scheme is well able to suppress the blocking artifacts while preserving the image details.

$$Q1 = \begin{bmatrix} 050 & 060 & 070 & 070 & 090 & 120 & 255 & 255 \\ 060 & 060 & 070 & 096 & 130 & 255 & 255 & 255 \\ 070 & 070 & 080 & 120 & 200 & 255 & 255 & 255 \\ 070 & 096 & 120 & 145 & 255 & 255 & 255 & 255 \\ 090 & 130 & 200 & 255 & 255 & 255 & 255 & 255 \\ 120 & 255 & 255 & 255 & 255 & 255 & 255 & 255 \\ 255 & 255 & 255 & 255 & 255 & 255 & 255 & 255 \\ 255 & 255 & 255 & 255 & 255 & 255 & 255 & 255 \end{bmatrix} \quad Q2 = \begin{bmatrix} 086 & 059 & 054 & 086 & 129 & 216 & 255 & 255 \\ 064 & 064 & 075 & 102 & 140 & 255 & 255 & 255 \\ 075 & 070 & 086 & 129 & 216 & 255 & 255 & 255 \\ 075 & 091 & 118 & 156 & 255 & 255 & 255 & 255 \\ 097 & 118 & 199 & 255 & 255 & 255 & 255 & 255 \\ 129 & 189 & 255 & 255 & 255 & 255 & 255 & 255 \\ 255 & 255 & 255 & 255 & 255 & 255 & 255 & 255 \\ 255 & 255 & 255 & 255 & 255 & 255 & 255 & 255 \end{bmatrix}$$

$$Q3 = \begin{bmatrix} 110 & 130 & 150 & 192 & 255 & 255 & 255 & 255 \\ 130 & 150 & 192 & 255 & 255 & 255 & 255 & 255 \\ 150 & 192 & 255 & 255 & 255 & 255 & 255 & 255 \\ 192 & 255 & 255 & 255 & 255 & 255 & 255 & 255 \\ 255 & 255 & 255 & 255 & 255 & 255 & 255 & 255 \\ 255 & 255 & 255 & 255 & 255 & 255 & 255 & 255 \\ 255 & 255 & 255 & 255 & 255 & 255 & 255 & 255 \\ 255 & 255 & 255 & 255 & 255 & 255 & 255 & 255 \end{bmatrix}$$

Fig. 5.7: Block DCT Quantization tables Q1, Q2 and Q3

Table. 5.1: PSNR (in dB) comparison between proposed method and the best results reported in [2] for restoration from JPEG compression with different quality factors (Q_f)

QF	Lena (512x512)		
	JPEG	Best results from [2]	Proposed
4	26.46	27.63	**27.76**
6	28.24	29.22	**29.51**
8	29.47	30.37	**30.54**
10	30.41	31.17	**31.37**
12	31.09	31.79	**31.98**
QF	Peppers (512x512)		
	JPEG	Best results from [2]	Proposed
4	25.61	**26.72**	**26.71**
6	27.32	28.22	**28.24**
8	28.40	**29.28**	29.15
10	29.16	**29.94**	29.82
12	29.78	**30.47**	30.34
QF	Barbara (512x512)		
	JPEG	Best results from [2]	Proposed
4	23.48	24.13	**24.61**
6	24.50	25.08	**25.47**
8	25.19	25.71	**26.12**
10	25.79	26.27	**26.64**
12	26.33	26.81	**27.14**

Table. 5.2: PSNR (in dB) comparison between [83], [30], [81], [42] and proposed scheme for restoration from block DCT quantization for three different quantization matrices.

Table	Lena (512x512)					
	Test image	[83]	[30]	[81]	[42]	Proposed
Q1	30.70	31.21	31.30	31.14	**31.61**	**31.60**
Q2	30.09	30.76	30.70	30.65	**31.19**	31.14
Q3	27.38	28.31	27.89	28.07	**28.65**	28.62
Table	Barbara (512x512)					
	Test image	[83]	[30]	[81]	[42]	Proposed
Q1	25.94	25.23	24.65	26.14	26.37	**26.77**
Q2	25.59	25.07	24.54	25.83	26.04	**26.47**
Q3	24.03	24.11	23.63	24.40	24.66	**25.05**
Table	Peppers(512x512)					
	Test image	[83]	[30]	[81]	[42]	Proposed
Q1	30.42	30.65	31.15	30.99	**31.33**	31.20
Q2	29.82	30.23	30.56	30.52	**30.97**	30.74
Q3	27.22	28.19	27.86	28.14	**28.55**	28.42

Table. 5.3: Grayscale image deblocking performance (in terms of PSNR) for the proposed scheme. For each image, the first and second row show the PSNR values of Test image and image processed with proposed scheme respectively. The third row for each image show improvement of PSNR of processed image over test image.

Image/Q_f	4	6	8	10	12	16	20	30	40	50
Bridge	22.35	23.62	24.48	25.12	25.63	26.42	27.01	28.08	28.85	29.54
	23.03	24.20	24.99	25.58	26.04	26.78	27.34	28.36	29.13	29.83
	0.68	0.58	0.51	0.46	0.41	0.36	0.33	0.28	0.28	0.29
Boat	24.64	26.26	27.31	28.13	28.78	29.76	30.49	31.84	32.76	33.49
	25.64	27.18	28.14	28.87	29.44	30.34	31.00	32.29	33.16	33.85
	1.00	0.92	0.83	0.74	0.66	0.58	0.51	0.45	0.40	0.36
Cameraman	23.53	25.00	25.87	26.48	27.04	27.90	28.59	29.93	30.89	31.74
	24.20	25.48	26.30	26.94	27.42	28.27	28.92	30.27	31.20	32.07
	0.67	0.48	0.43	0.46	0.38	0.37	0.33	0.34	0.31	0.33
Fingerprint	22.23	24.28	25.59	26.57	27.35	28.57	29.49	31.16	32.25	33.08
	23.66	25.47	26.60	27.55	28.25	29.41	30.26	31.82	32.82	33.61
	1.43	1.19	1.01	0.98	0.90	0.84	0.77	0.66	0.57	0.53
Bike	21.15	22.14	22.86	23.39	23.85	24.71	25.43	26.92	28.06	29.02
	21.80	22.70	23.36	23.82	24.27	25.13	25.83	27.30	28.43	29.38
	0.65	0.56	0.50	0.43	0.42	0.42	0.40	0.38	0.37	0.36
Crowd	24.75	26.58	27.89	28.86	29.62	30.81	31.68	33.24	34.27	35.10
	25.88	27.62	28.80	29.71	30.39	31.49	32.29	33.76	34.73	35.51
	1.13	1.04	0.91	0.85	0.77	0.68	0.61	0.52	0.46	0.41
House	26.15	28.10	29.64	30.58	31.22	32.25	33.04	34.21	35.07	35.78
	27.29	29.36	30.53	31.43	31.99	32.91	33.60	34.69	35.48	36.21
	1.14	1.26	0.89	0.85	0.77	0.66	0.56	0.48	0.41	0.43
Goldhill	25.30	26.86	27.89	28.65	29.23	30.16	30.87	32.11	32.90	33.58
	26.40	27.78	28.67	29.35	29.84	30.72	31.37	32.49	33.25	33.93
	1.10	0.92	0.78	0.70	0.61	0.56	0.50	0.38	0.35	0.35

(a) (b)

(c) (d)

Fig. 5.8: Deblocking results for Barbara image (a) Original Image (b) Block DCT compressed with Q1 (PSNR=25.95dB) (c) Processed image with Liew and Yan's [42] algorithm (PSNR=26.37dB) (d) Processed image with Proposed method (Threshold=8.39, PSNR=26.77dB)

Fig. 5.9: Deblocking results for Bridge and Goldhill image (a) Original Bridge image (b) JPEG image (Q_f=6, PSNR=23.62 dB) (c) Processed image with Proposed method (Threshold=13.07, PSNR=24.20) (d) Original Goldhill image (e) JPEG image (Q_f=4, PSNR=25.30 dB) (f) Processed image with Proposed method (Threshold=18.94, PSNR=26.40 dB)

5.2.5 Concluding Remarks

We have proposed a fast and efficient LT based image deblocking method for block DCT compressed images. The method is based on soft thresholding in the lapped orthogonal transform domain. We have shown that there exists a strong correlation between the experimentally observed global 'optimal' threshold and the JPEG image Quality factor (Q_f). We have also demonstrated that the experimentally observed global 'optimal' threshold is highly correlated to the average of first 3x3 values of the quantization table (Q_{av}). Our method can determine the soft threshold values that are adaptive to various compressed images using various quantization tables. The method outperforms several well known image deblocking schemes in terms of PSNR and is able to reduce the blocking artifacts effectively while preserving true edges and textural information.

5.3 Blocking and Ringing Artifacts Reduction Using Combined LT and Adaptive Bilateral Filtering

In this section, we propose a non iterative two stage image deblocking and deringing method where the first stage reduces a major part of the blocking artifacts in LT domain using local Wiener filtering and the second stage reduces the residual artifacts in spatial domain using an adaptive bilateral filter [78]. The first stage filter uses local variance in LT domain for pixel adaptive processing. The parameters of bilateral filter is selected adaptively through an empirical study. Finally the DCT quantization constraint and the range constraint are enforced onto the filtered output. The experimental results and an extensive comparison with various wavelet, non wavelet, iterative and non iterative schemes validate the efficiency of our proposed method.

5.3.1 Proposed Scheme

Fig. 5.10 shows the block diagram of the proposed image deblocking and deringing method. We use the same observation model (5.1) discussed in previous section:

$$y_t = x_t + \eta_t \tag{5.12}$$

where x_t is the original uncompressed image, y_t is the observed block DCT compressed image and η_t is the degradation due to quantization process. The orthogonal LT coefficients of the image y_t is

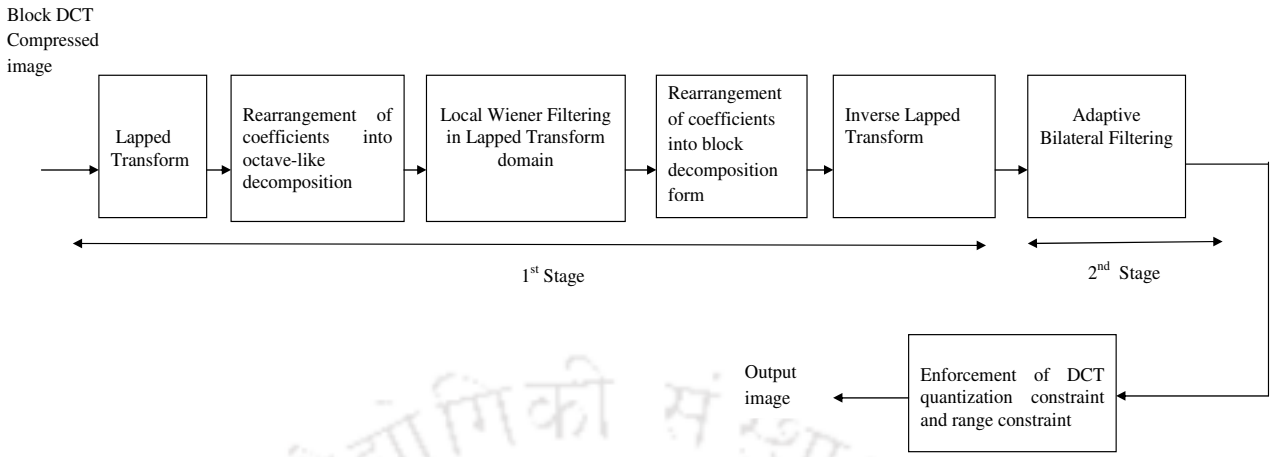

Fig. 5.10: Block diagram of the proposed two stage image deblocking scheme

given by

$$y(k) = x(k) + \eta(k) \tag{5.13}$$

where $x(k)$, $y(k)$ respectively represent the LT coefficients of the uncompressed and the block DCT compressed images. Motivated by the encouraging denoising performance of local Wiener filtering in LT domain as discussed in Chapter 4, we propose to use the same concept for reducing the blocking artifacts. The local Wiener filter estimate for $x(k)$ is given by (4.19) which is repeated here for convenience

$$\widehat{x}(k) = \frac{\widehat{\sigma}_x^2}{\widehat{\sigma}_x^2 + \sigma_\eta^2} y(k) \tag{5.14}$$

where $\widehat{\sigma}_x^2(k)$ represents the estimate of the variance of the uncompressed image LT coefficients. We propose to find $\widehat{\sigma}_x^2(k)$ using MAP estimation procedure (4.18) for each coefficient. The expression is repeated here for convenience

$$\hat{\sigma}_x^2(k) = \max\left(0, \frac{G}{4\lambda}\left[-1 + \sqrt{1 + \frac{8\lambda}{G^2}\sum_{j \in Z(k)} Y^2(j)}\right] - \sigma_\eta^2\right) \tag{5.15}$$

The parameter λ for each subband is estimated as discussed in Chapter 4. To apply the local Wiener filter (5.14), we need to find a suitable value of σ_η.

It is to be noted that the σ_η is not an estimate of the standard deviation of the difference between the original and the block DCT compressed image - σ_η is just the assumed value of standard deviation of η in our observation model (5.12). It is assumed that σ_η is the standard deviation of the noise when

added to the original image x_t would require, for removal, the same amount of adaptive smoothing necessary to reduce the blocking artifacts produced by the block DCT based compression scheme with the quantization table Q. Much larger values of σ_η may result in oversmoothing and much smaller values may result in insufficient removal of blocking artifacts. We performed experiments on

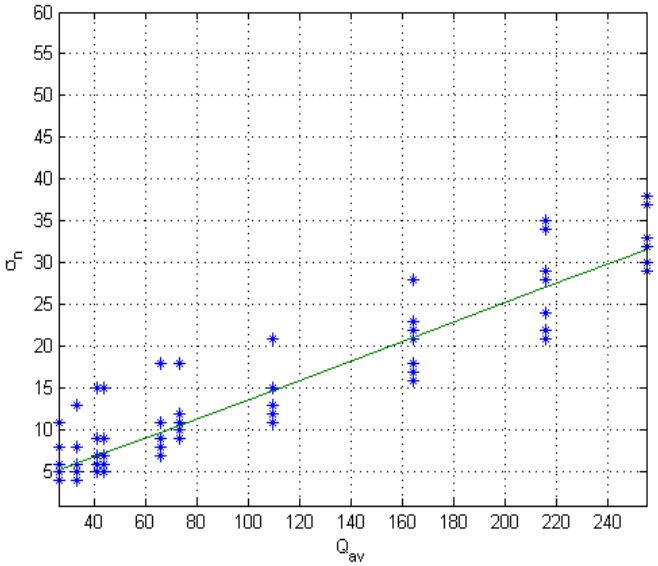

Fig. 5.11: Scatter plot of σ_n versus Q_{av} and curve fitting using linear polynomial

several JPEG compressed test images in which we plot the best values of σ_η (found experimentally) which gives the lowest mean square error for different values of Q_{av} as shown in Fig. 5.11. The scatter plot show approximately linear relationship between the standard deviation σ_η and Q_{av}.

The data when fitted with a linear polynomial, gives σ_η as

$$\sigma_n = p1.Q_{av} + p2 \tag{5.16}$$

where $p1$=0.1149 and $p2$=2.246. The experimental results show that the results are not very sensitive to the fitting errors and the fitted curve can be considered for a wide range of test images and quantization tables. The σ_η values are larger for higher compression ratios and smaller for lower compression ratios. The experimental results to be presented in next section will show that this technique reduces the blocking artifacts very efficiently while preserving edges and textures. This technique alone outperforms several well known image deblocking schemes reported in [2, 10, 13, 30, 31, 42, 69, 81, 83, 88].

It was observed that the images processed by the first stage shows significant reduction of blocking artifacts; however, the ringing artifacts were still visible near the strong edges. The artifacts present

in the first stage output which consists of mostly ringing artifacts is referred to as residual artifacts. As a result of coarse quantization, ringing artifacts are produced near strong edges due to truncation of high frequency DCT coefficients. The ringing artifacts are visually annoying and needs to be suppressed. To reduce the residual artifacts, we propose to use an adaptive bilateral filter. The bilateral filter smooths out the residual artifacts while preserving the edges.

Bilateral filter [78] is a linear, edge preserving smoothing filter. It modifies the pixel value by weighted average of its neighborhood pixels where the weights are determined using both the intensity distance as well as the spatial distance. The output of a bilateral filter at spatial position k is given by

$$V(k) = \frac{1}{F} \sum_{m \in Z(k)} e^{-\frac{\|m-k\|^2}{2\sigma_s^2}} e^{-\frac{|A(m)-A(k)|^2}{2\sigma_i^2}} A(m) \tag{5.17}$$

where σ_s and σ_i control the weights in spatial and intensity domain and F is a normalization factor given by

$$F = \sum_{m \in Z(k)} e^{-\frac{\|m-k\|^2}{2\sigma_s^2}} e^{-\frac{|A(m)-A(k)|^2}{2\sigma_i^2}} \tag{5.18}$$

and $Z(k)$ is a square window centered at $A(k)$.

The bilateral filter performance depends on two filter parameters σ_s and σ_i, which affect the filtering results significantly. The σ_s and σ_i control the weights in spatial and intensity domains. In [91], Zhang and Gunturk performed an empirical study on the parameter selection of bilateral filter in relation to image denoising. Motivated by their work, we performed similar empirical study based on the selection of σ_s and σ_i parameters of the bilateral filter to suppress the residual artifacts. With varying amount of residual artifacts, the selection of the parameter σ_i is much more important as compared to the parameter σ_s. Smaller σ_i value may not suppress the residual artifacts efficiently whereas larger σ_i values may lead to oversmoothing of textures or other important details which may result in increase in mean square error. It is also observed that the optimal σ_s values are very difficult to relate to the optimal σ_i values. Based on this observation, we performed experiments to find a relation between the optimal σ_i parameter of the 2nd stage and the σ_η value of the 1st stage in order to make the bilateral filter adaptive to different quantization tables. It is also observed that the optimal σ_s value is relatively insensitive to σ_η. The best value of σ_i (found experimentally) are recorded for different compression ratios and then plotted against the estimated values of σ_η as shown in Fig. 5.12. The scatter plot shows approximately a linear relationship between σ_η and σ_i.

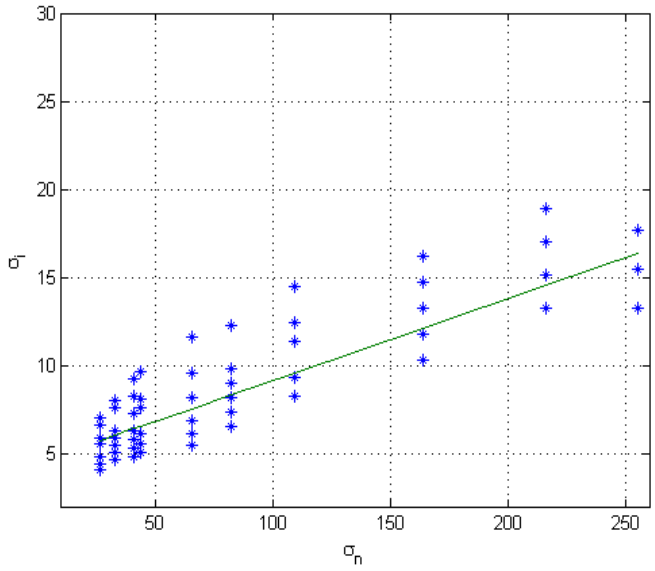

Fig. 5.12: Scatter plot of σ_n versus σ_i and curve fitting using linear polynomial

The data when fitted with a linear polynomial yields

$$\sigma_i = p1\sigma_n + p2 \tag{5.19}$$

where $p1$=0.6163 and $p2$=4.546. The simulation results shows that (5.16) is adequate for a wide range of quantization tables and images. Finally the quantization constraint and the range constraint are imposed on the filtered output. The results to be presented in next section will demonstrate the efficacy of the proposed technique.

Fig. 5.13(c) and Fig. 5.13(d) respectively show the 1st and the 2nd stage outputs of the proposed scheme. Fig. 5.13(c) shows that the 1st stage of the proposed method not only yields a good PSNR improvement, at the same time the subjective quality is almost free of the blocking artifacts while preserving the true edges and textural information. The bilateral filtering with appropriate parameter selection brings in further improvement in visual quality by suppressing the residual artifacts and without oversmoothing the textures and other important details as shown in Fig. 5.13(d) and 5.14(d). The combined action of these two stages shows very good subjective and objective results and outperforms several well known state of the art image deblocking techniques.

To verify whether an adaptive bilateral filter when directly applied on the input test image can bring so much of improvement in objective and subjective quality, we perform some experiments where in order to make the bilateral filter adaptive to any input test image we measure the best values of σ_i which gives the lowest mean square error (experimentally) at different compression ratios

i.e. at different Q_{av}. Then we plot the best values of σ_i against different Q_{av}; we find that the σ_i values can be approximately linearly related to Q_{av}. The data when fitted with an linear polynomial gives

$$\sigma_i = p1.Q_{av} + p2 \tag{5.20}$$

where $p1$=0.3241 and $p2$=3.1530. The post processing using (5.20) shows very good results for test images with relatively smooth regions but does not perform well for highly textured images. The main reason is that large σ_i parameters are required in this case to smooth out the large amount of blocking and ringing artifacts. A large σ_i value while smoothing the block discontinuities may also smoothen out the textural patterns.

The adaptive bilateral filter at the 2nd stage of our proposed scheme requires relatively smaller σ_i values to smooth out the residual artifacts and hence do not oversmooth the textural patterns present in the images.

5.3.2 Experimental Results

To evaluate the performance of our proposed method, we perform experiments on a large set of test images which include several test images outside the training set. The images Lena, Barbara, Peppers, Mandrill, Boats, Bridge, Birds, Airplane, Sailboat and Elaine were used in the training stage.

In Table 5.4, the PSNR results of the proposed method (1st stage alone) is compared with the best PSNR results obtained by any of the methods [2, 10, 13, 31, 69, 88] as reported in [2]. The results show that for Lena and Barbara images the proposed method outperforms the best results reported in [2] while it performs very close for the Peppers image.

In Table 5.5, the PSNR results of the proposed method (1st stage alone) is compared with the results of several well known decimated and non-decimated wavelet based image deblocking schemes [30, 42, 81, 83]. The results show that the proposed scheme (1st stage alone) outperforms [30, 81, 83] consistently for all the test images. The proposed method outperforms the method discussed in [42] for Lena and Barbara images while it performs very close for the Peppers image.

Table 5.6-5.8 show the comparison of PSNR and structural similarity (SSIM) index [80] results between the proposed method and the well known shape adaptive DCT based image deblocking scheme [25] for several images. SSIM index is a popular reference based measure of perceptual quality. The SSIM index is a number in the interval (0,1)- a larger value indicates better quality

with the value 1 indicating the ideal quality. The PSNR and SSIM results shown in Tables 5.6-5.8 show that the proposed method (combined stages) outperforms the SA-DCT based scheme in terms of PSNR for many images at different bit rates. In respect of SSIM index results, the proposed method outperforms SA-DCT based scheme for almost all the test images.

Table 5.9 shows that the method which uses only an adaptive bilateral filter performs quite close to the SA-DCT based method in terms of PSNR. However, in terms of SSIM index results, the adaptive bilateral filter alone outperforms the SA-DCT based method for almost all the images except the Barbara image. As discussed at the end of Section 5.3.1, this method does not perform well for images with high amount of textures which can also be seen from Table 5.9 for Barbara image.

Fig. 5.13 shows comparison of visual results of proposed scheme and those discussed in [42] and [25] for Crowd image. Fig. 5.14 and 5.15 respectively shows the visual results of proposed scheme and [25] for Goldhill and Barbara images. The visual results show that the blocking and ringing artifacts are significantly reduced in the output images obtained with the proposed scheme preserving most of the important details and textural information. The PSNR result improvements is more significant at low compression ratios. However, SSIM index results show good improvement at almost all the tested bit rates showing good visual quality improvement. Fig. 5.16 shows the visual results of proposed scheme and the case when adaptive bilateral filter alone is used for image deblocking for Lena image. As noted earlier (at the end of Section 5.3.1) the visual results show insufficient reduction of blocking artifacts at some texture regions and oversmoothing at some other texture regions.

5.3.3 Computational Complexity in Terms of Required Time For Processing

On a Intel Core 2 Duo, 2.10 GHz processor (with 2GB RAM) and a Windows 7 operating system (in MATLAB), in the case of Lena (512x512) image compressed with JPEG algorithm at Q_f=6, the results obtained are shown in Table 5.10. It is to be noted that the computational complexity of the proposed image deblocking algorithms was evaluated for an implementation which is not fully optimized for speed. As can be seen from the Table 5.10, the proposed image deblocking algorithm based on soft thresholding and the 1st stage of the proposed two stage deblocking algorithm requires much less processing time when compared to Liew et al's [42] scheme. Further, the proposed two stage method with both stages working requires comparatively less processing time when compared to Foi et al's scheme [25].

Table. 5.4: PSNR (in dB) comparison between proposed method (only 1st stage) and best results reported in [2] for restoration from JPEG compression with different quality factors (Q_f)

QF	Lena (512x512)		
	JPEG	Best results from [2]	Proposed (only 1st stage)
4	26.46	27.63	**27.74**
6	28.24	29.22	**29.49**
8	29.47	30.37	**30.59**
10	30.41	31.17	**31.41**
12	31.09	31.79	**32.04**
QF	Peppers (512x512)		
	JPEG	Best results from [2]	Proposed (only 1st stage)
4	25.61	**26.72**	26.69
6	27.32	**28.22**	**28.23**
8	28.40	**29.28**	29.14
10	29.16	**29.94**	29.84
12	29.78	**30.47**	30.34
QF	Barbara (512x512)		
	JPEG	Best results from [2]	Proposed (only 1st stage)
4	23.48	24.13	**24.56**
6	24.50	25.08	**25.40**
8	25.19	25.71	**26.04**
10	25.79	26.27	**26.53**
12	26.33	26.81	**27.03**

Table. 5.5: PSNR (in dB) comparison between [83], [30], [81], [42] and proposed scheme (only 1st stage) for restoration from block DCT quantization for three different quantization matrices.

Table	Lena (512x512)					
	Test image	[83]	[30]	[81]	[42]	Proposed (only 1st stage)
Q1	30.70	31.21	31.30	31.14	31.61	**31.66**
Q2	30.09	30.76	30.70	30.65	**31.19**	**31.18**
Q3	27.38	28.31	27.89	28.07	**28.65**	**28.66**
Table	Barbara (512x512)					
	Test image	[83]	[30]	[81]	[42]	Proposed (only 1st stage)
Q1	25.94	25.23	24.65	26.14	26.37	**26.68**
Q2	25.59	25.07	24.54	25.83	26.04	**26.34**
Q3	24.03	24.11	23.63	24.40	24.66	**25.03**
Table	Peppers(512x512)					
	Test image	[83]	[30]	[81]	[42]	Proposed (only 1st stage)
Q1	30.42	30.65	31.15	30.99	**31.33**	31.19
Q2	29.82	30.23	30.56	30.52	**30.97**	30.73
Q3	27.22	28.19	27.86	28.14	**28.55**	28.43

Table. 5.6: PSNR (dB, in regular) and SSIM index reults (in italics) comparison between proposed method and SA-DCT [25] based image deblocking scheme for restoration from JPEG compression with different quality factors (Q_f) and block DCT quantization for three different quantization matrices.

Q_f/Table	Lena (512x512)			
	Test image	SA-DCT scheme [25]	Proposed (only 1st stage)	Proposed (Both stages)
4	26.47 *0.7426*	28.07 *0.7957*	27.74 *0.7892*	**28.25** ***0.8122***
6	28.25 *0.8099*	29.86 *0.8574*	29.49 *0.8552*	**30.01** ***0.8741***
8	29.47 *0.8469*	**30.98** *0.8859*	30.59 *0.8862*	**30.98** ***0.8969***
10	30.41 *0.8763*	**31.84** *0.9087*	31.41 *0.9077*	**31.82** ***0.9171***
12	31.09 *0.8948*	**32.47** *0.9220*	32.04 *0.9214*	32.39 ***0.9270***
Q1	30.71 *0.8934*	**32.12** *0.9178*	31.66 *0.9183*	32.02 ***0.9226***
Q2	30.09 *0.8639*	31.55 *0.9012*	31.18 *0.9011*	**31.59** ***0.9110***
Q3	27.44 *0.7982*	29.03 *0.8432*	28.66 *0.8468*	**29.04** ***0.8573***
Q_f/Table	Barbara (512x512)			
	Test image	SA-DCT scheme [25]	Proposed (only 1st stage)	Proposed (Both stages)
4	23.49 *0.7149*	24.65 *0.7696*	24.56 *0.7654*	**24.81** ***0.7807***
6	24.49 *0.7845*	25.51 *0.8275*	25.40 *0.8227*	**25.66** ***0.8368***
8	25.19 *0.8342*	26.11 *0.8670*	26.04 *0.8658*	**26.24** ***0.8744***
10	25.79 *0.8696*	26.61 *0.8978*	26.53 *0.8947*	**26.72** ***0.8999***
12	26.33 *0.8914*	27.10 *0.9133*	27.03 *0.9116*	**27.21** ***0.9140***
Q1	25.95 *0.8816*	26.79 *0.9031*	26.68 *0.9011*	**26.87** ***0.9040***
Q2	25.59 *0.8576*	26.45 *0.8877*	26.34 *0.8856*	**26.56** ***0.8913***
Q3	24.05 *0.7635*	25.13 *0.8090*	25.03 *0.8103*	**25.19** ***0.8162***
Q_f/Table	Peppers (512x512)			
	Test image	SA-DCT scheme [25]	Proposed (only 1st stage)	Proposed (Both stages)
4	25.59 *0.7510*	27.40 *0.8148*	26.69 *0.7975*	**27.55** ***0.8326***
6	27.32 *0.8127*	28.96 *0.8679*	28.23 *0.8522*	**29.05** ***0.8790***
8	28.39 *0.8490*	**29.89** *0.8938*	29.14 *0.8828*	29.83 ***0.9033***
10	29.17 *0.8770*	**30.49** *0.9110*	29.84 *0.9035*	30.46 ***0.9185***
12	29.78 *0.8917*	**30.99** *0.9196*	30.34 *0.9133*	30.90 ***0.9250***
Q1	30.45 *0.8987*	**32.07** *0.9287*	31.19 *0.9220*	31.88 ***0.9325***
Q2	29.85 *0.8720*	31.43 *0.9142*	30.73 *0.9059*	**31.45** ***0.9217***
Q3	27.25 *0.8029*	29.13 *0.8717*	28.43 *0.8581*	**29.19** ***0.8814***
Q_f/Table	Boat (512x512)			
	Test image	SA-DCT scheme [25]	Proposed (only 1st stage)	Proposed (Both stages)
4	24.64 *0.7075*	25.82 *0.7447*	25.59 *0.7462*	**25.89** ***0.7562***
6	26.26 *0.7973*	27.39 *0.8244*	27.14 *0.8279*	**27.45 0.8336**
8	27.31 *0.8439*	**28.41** *0.8700*	28.13 ***0.8720***	28.38 *0.8714*
10	28.13 *0.8763*	**29.14** *0.8956*	28.87 ***0.8980***	29.11 *0.8976*
12	28.78 *0.9003*	**29.76** *0.9158*	29.46 ***0.9174***	29.68 *0.9150*
Q1	28.40 *0.8908*	**29.42** *0.9041*	29.08 ***0.9064***	29.29 *0.9024*
Q2	27.89 *0.8697*	**28.90** *0.8885*	28.64 ***0.8920***	28.87 *0.8902*
Q3	25.47 *0.7655*	**26.58** *0.7898*	26.29 ***0.7971***	26.48 *0.7967*

Table. 5.7: PSNR (dB, in regular) and SSIM index reults (in italics) comparison between proposed method and SA-DCT [25] based image deblocking scheme for restoration from JPEG compression with different quality factors (Q_f) and block DCT quantization for three different quantization matrices.

Q_f/Table	Elaine (512x512)			
	Test image	SA-DCT scheme [25]	Proposed (only 1st stage)	Proposed (Both stages)
4	26.45 *0.7044*	28.29 *0.7913*	27.96 *0.7874*	**28.59** ***0.8170***
6	28.18 *0.7837*	29.76 *0.8522*	29.40 *0.8470*	**29.99** ***0.8681***
8	29.23 *0.8344*	30.54 *0.8826*	30.21 *0.8829*	**30.62** ***0.8919***
10	29.94 *0.8656*	31.03 *0.9012*	30.74 *0.9016*	**31.08** ***0.9081***
12	30.43 *0.8875*	**31.35** *0.9137*	31.08 *0.9149*	**31.36** ***0.9180***
Q1	30.19 *0.8829*	**31.22** *0.9084*	30.91 *0.9111*	**31.21** ***0.9137***
Q2	29.73 *0.8592*	30.89 *0.8972*	30.59 *0.8982*	**30.95** ***0.9049***
Q3	27.74 *0.7800*	29.49 *0.8464*	29.15 *0.8524*	**29.58** ***0.8616***
Q_f/Table	House (256x256)			
	Test image	SA-DCT scheme [25]	Proposed (only 1st stage)	Proposed (Both stages)
4	26.15 *0.6690*	27.38 ***0.7119***	27.19 *0.6459*	**27.72** *0.6880*
6	28.09 *0.7040*	29.17 *0.7354*	29.23 *0.7087*	**29.94** ***0.7458***
8	29.64 *0.7333*	30.99 *0.7657*	30.45 *0.7373*	**31.16** ***0.7700***
10	30.58 *0.7499*	**32.09** *0.7779*	31.37 *0.7551*	**32.08** ***0.7816***
12	31.22 *0.7638*	**32.63** *0.7867*	31.97 *0.7685*	**32.63** ***0.7915***
Q1	30.84 *0.7499*	32.38 *0.7785*	31.54 *0.7560*	**32.22** ***0.7821***
Q2	30.03 *0.7329*	31.59 *0.7675*	31.04 *0.7448*	**31.84** ***0.7778***
Q3	27.46 *0.6773*	**28.99** ***0.7273***	28.38 *0.6857*	28.92 *0.7215*
Q_f/Table	Goldhill (512x512)			
	Test image	SA-DCT scheme [25]	Proposed (only 1st stage)	Proposed (Both stages)
4	25.29 *0.6939*	26.45 *0.7329*	26.28 *0.7368*	**26.55** ***0.7421***
6	26.86 *0.7875*	27.91 *0.8156*	27.68 *0.8161*	**27.94** ***0.8187***
8	27.89 *0.8383*	**28.76** *0.8541*	28.59 ***0.8586***	**28.76** *0.8553*
10	28.65 *0.8700*	29.44 *0.8802*	29.29 ***0.8865***	**29.46** *0.8821*
12	29.23 *0.8919*	**29.97** *0.8984*	29.81 ***0.9048***	29.93 *0.8980*
Q1	28.88 *0.8803*	**29.67** *0.8854*	29.48 ***0.8919***	29.62 *0.8855*
Q2	28.40 *0.8592*	**29.22** *0.8710*	29.07 ***0.8779***	**29.22** *0.8732*
Q3	26.26 *0.7479*	**27.26** *0.7741*	27.07 ***0.7821***	27.18 *0.7761*
Q_f/Table	Crowd (512x512)			
	Test image	SA-DCT scheme [25]	Proposed (only 1st stage)	Proposed (Both stages)
4	24.75 *0.7697*	26.22 *0.8094*	25.89 *0.8074*	**26.28** ***0.8194***
6	26.58 *0.8434*	27.99 *0.8751*	27.65 *0.8741*	**28.10** ***0.8855***
8	27.89 *0.8838*	29.26 *0.9072*	28.87 *0.9067*	**29.29** ***0.9133***
10	28.86 *0.9076*	30.18 *0.9275*	29.79 *0.9262*	**30.21** ***0.9322***
12	29.62 *0.9245*	**30.91** *0.9396*	30.49 *0.9390*	30.88 ***0.9422***
Q1	28.99 *0.9172*	**30.33** *0.9320*	29.87 *0.9312*	30.28 ***0.9349***
Q2	28.55 *0.8999*	29.88 *0.9201*	29.51 *0.9197*	**29.91** ***0.9251***
Q3	25.55 *0.8151*	**26.92** *0.8467*	26.59 *0.8494*	26.86 ***0.8531***

Table. 5.8: PSNR (dB, in regular) and SSIM index reults (in italics) comparison between proposed method and SA-DCT [25] based image deblocking scheme for restoration from JPEG compression with different quality factors (Q_f) and block DCT quantization for three different quantization matrices.

Q_f/Table	Mandrill (512x512)			
	Test image	SA-DCT scheme [25]	Proposed (only 1st stage)	Proposed (Both stages)
4	20.89 *0.6690*	21.53 *0.6694*	21.49 ***0.6877***	**21.61** *0.6713*
6	22.05 *0.7804*	22.60 *0.7830*	22.58 ***0.7976***	**22.68** *0.7845*
8	22.83 *0.8383*	23.32 *0.8404*	23.29 ***0.8525***	**23.36** *0.8381*
10	23.43 *0.8744*	23.85 *0.8730*	23.85 ***0.8839***	**23.91** *0.8733*
12	23.90 *0.8970*	24.30 *0.8963*	24.29 ***0.9041***	**24.36** *0.8940*
Q1	23.39 *0.8764*	23.82 *0.8736*	23.80 ***0.8842***	**23.87** *0.8726*
Q2	23.24 *0.8638*	23.68 *0.8636*	23.68 ***0.8753***	**23.74** *0.8626*
Q3	21.18 *0.7076*	21.69 *0.6941*	21.68 ***0.7189***	**21.72** *0.6935*
Q_f/Table	Einstein (256x256)			
	Test image	SA-DCT scheme [25]	Proposed (only 1st stage)	Proposed (Both stages)
4	27.18 *0.6275*	28.50 *0.6757*	28.56 *0.6883*	**29.03** ***0.7058***
6	29.31 *0.7268*	30.66 *0.7621*	30.51 *0.7705*	**30.99** ***0.7803***
8	30.45 *0.7752*	31.73 *0.8046*	31.51 *0.8120*	**31.81** ***0.8137***
10	31.39 *0.8216*	32.46 *0.8299*	32.31 ***0.8449***	**32.58** *0.8430*
12	32.06 *0.8473*	33.02 *0.8503*	32.89 ***0.8663***	**33.04** *0.8611*
Q1	31.71 *0.8331*	**32.73** *0.8341*	32.52***0.8503***	32.70 *0.8440*
Q2	31.10 *0.8085*	32.24 *0.8213*	32.08 ***0.8364***	**32.32** *0.8339*
Q3	28.94 *0.7090*	30.28 *0.7430*	30.25 ***0.7591***	**30.49** *0.7580*

Table. 5.9: PSNR (dB, in regular) and SSIM index reults (in italics) comparison between the scheme where only adaptive Bilateral filtering is used, proposed method and SA-DCT [25] based image deblocking scheme for restoration from JPEG compression with different quality factors (Q_f).

QF	Lena (512x512)			
	JPEG	[25]	Only Adaptive Bilateral filter	Proposed
4	26.46 *0.7426*	28.07 *0.7957*	27.83 *0.7977*	**28.25** ***0.8122***
6	28.24 *0.8099*	29.86 *0.8574*	29.55 *0.8613*	**30.01** ***0.8741***
8	29.47 *0.8469*	**30.98** *0.8859*	30.61 *0.8901*	**30.98** ***0.8969***
10	30.41 *0.8763*	**31.84** *0.9087*	31.42 *0.9111*	31.82 ***0.9171***
12	31.09 *0.8948*	**32.47** *0.9220*	32.05 *0.9242*	32.39 ***0.9270***
QF	Peppers (512x512)			
	JPEG	[25]	Only Adaptive Bilateral filter	Proposed
4	25.59 *0.7510*	27.40 *0.8148*	27.33 *0.8211*	**27.55** ***0.8326***
6	27.32 *0.8127*	28.96 *0.8679*	28.99 *0.8697*	**29.05** ***0.8790***
8	28.39 *0.8490*	**29.89** *0.8938*	**29.89** *0.8988*	29.83 ***0.9033***
10	29.17 *0.8770*	30.49 *0.9110*	**30.54** *0.9153*	30.46 ***0.9185***
12	29.78 *0.8917*	**30.99** *0.9196*	30.93 *0.9238*	30.90 ***0.9250***
QF	Barbara (512x512)			
	JPEG	[25]	Only Adaptive Bilateral filter	Proposed
4	23.49 *0.7149*	24.65 *0.7696*	24.39 *0.7615*	**24.81** ***0.7807***
6	24.49 *0.7845*	25.51 *0.8275*	25.26 *0.8200*	**25.66** ***0.8368***
8	25.19 *0.8342*	26.11 *0.8670*	25.89 *0.8624*	**26.24** ***0.8744***
10	25.79 *0.8696*	26.61 *0.8978*	26.38 *0.8899*	**26.72** ***0.8999***
12	26.33 *0.8914*	27.10 *0.9133*	26.86 *0.9063*	**27.21** ***0.9140***

Table. 5.10: Average computation time required for processing of Lena image compressed by JPEG algorithm at Q_f=6, on a Intel Core 2 Duo, 2.10 GHz processor (with 2 GB RAM) and a Windows 7 operating system (in MATLAB)

Method	Required time for processing
[42]	9.52 s
[25]	17.68 s
Proposed (Soft Th.)	3.87 s
Proposed (1st stage)	5.08 s
Proposed (Both stages)	13.66 s

Fig. 5.13: A fragment of Crowd image (σ_n=10.33, σ_i=10.91, σ_s=4.8) (a) Original Image (b) Block DCT compressed with Q2 (PSNR=28.55dB, SSIM=0.8999) (c) Processed image with only first stage of Proposed method (PSNR=29.51dB, SSIM=0.9197) (d) Processed image with both stages of Proposed method (PSNR=29.91dB, SSIM=0.9251)(e) Processed image with Liew and Yan's [42] algorithm (PSNR=29.31dB, SSIM=0.9108) (f) Processed image with SA-DCT based image deblocking scheme [25] (PSNR=29.88dB, SSIM=0.9201)

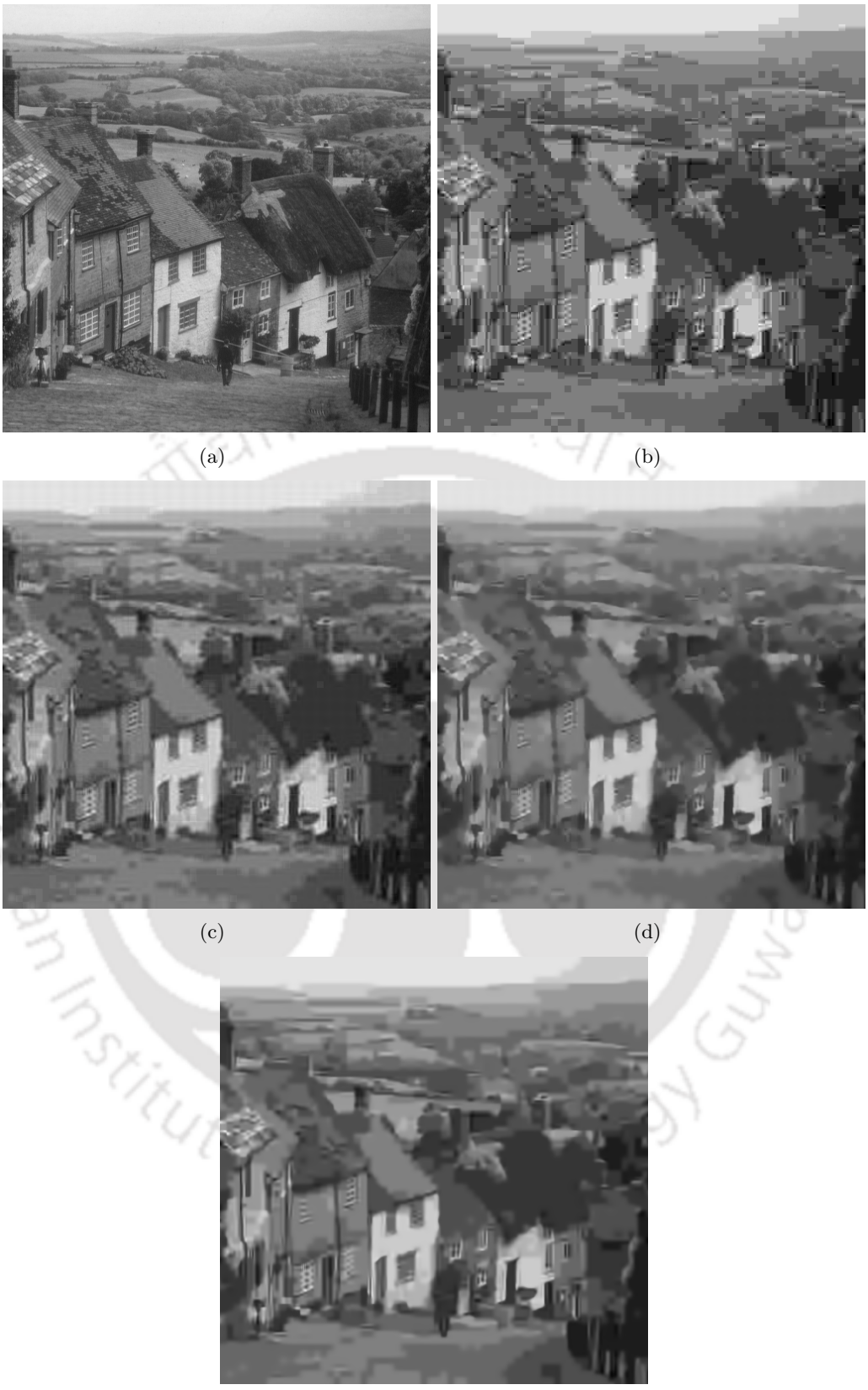

Fig. 5.14: Deblocking results for Goldhill image (σ_n=21.09, σ_i=17.54, σ_s=4.8) (a) Original Image (b) JPEG compressed (Q_f=6) (PSNR=25.29dB, SSIM=0.6939) (c) Processed image with only First stage of Proposed method (PSNR=26.28dB, SSIM=0.7368) (d) Processed image with both stages of Proposed method (PSNR=26.55dB, SSIM=0.7421) (e) Processed image with SA-DCT based image deblocking scheme [25] (PSNR=26.45dB, SSIM=0.7329)

(a) Original Image

(b) JPEG compressed (Q_f=6) (PSNR=24.49dB, SSIM=0.7845)

(c) Processed image with both stages of Proposed method (PSNR=25.66dB, SSIM=0.8368)

(d) Processed image with SA-DCT based image deblocking scheme [25] (PSNR=25.51dB, SSIM=0.8275)

Fig. 5.15: A fragment of Barbara image (σ_n=14.79, σ_i=13.66, σ_s=4.8)

(a) Original Image

(b) Block DCT compressed with Q3 (PSNR=27.44dB, SSIM=0.7982)

(c) Processed image with only adaptive Bilateral filter (PSNR=28.23dB, SSIM=0.8401)

(d) Processed image with both stages of Proposed method (PSNR=29.04dB, SSIM=0.8573)

Fig. 5.16: A fragment of Lena image

5.3.4 Concluding Remarks

We have presented a new and efficient two stage compression artifacts reduction algorithm for block DCT compressed images based on combined LT and adaptive bilateral filtering. We have modeled the degradation due to quantization noise as some additive noise. The first stage effectively reduces the blocking artifacts in the LOT domain using the concept of local Wiener filtering. We have demonstrated that the noise standard deviation has a high correlation with the average of first 3x3 values from the quantization matrix (Q_{av}). The noise standard deviation is made adaptive to the quantization table used in the compression process and is calculated using an empirical expression. The local variance estimate of each coefficient is estimated from the local observation of the signal. The method used in the first stage of the proposed algorithm is spatially adaptive and this stage alone can outperform several well known wavelet and non wavelet based image deblocking methods while preserving the true edges and textural information. The left out artifacts which include ringing is smoothed out using a edge preserving adaptive bilateral filter. The bilateral filter parameters are chosen based on an empirical study. We have demonstrated that the σ_i parameter of the bilateral filter is highly correlated to the noise standard deviation (σ_n) estimated in the first stage. The parameter σ_i is calculated from an empirical expression which is a function of σ_n. Since σ_n value is a function of Q_{av}, the parameter σ_i of bilateral filter becomes adaptive to the quantization tables used in the compression process. The final output of the proposed scheme shows excellent visual results with very good preservation of important image details. The proposed method outperforms many existing well known image deblocking methods both objectively and subjectively. The method outperforms one well known SA-DCT based image deblocking algorithm for many test images in terms of PSNR. When compared in terms of SSIM index results, the final output of the proposed method outperforms the SA-DCT based algorithm for almost all the test images. It is to be noted that the SSIM index is known to be a good indicator of perceived image quality. The experimental results indicates that the proposed two stage compression artifacts reduction algorithm can preserve the textures better than the SA-DCT based method.

Chapter 6

Conclusions and Future Work

6.1 Summary

In this thesis, we have investigated the statistical distributions which best model the LT coefficients and proposed various image denoising and deblocking algorithms based on statistical modeling of LT coefficients. The key contributions are summarized below:

- Based on KS and Chi-square goodness of fit tests, an appropriate probability density function is proposed which best models the block LOT and LBT coefficients. An exhaustive comparative study is carried out on the performance of Gaussian, Laplacian, Gamma and Generalized Gaussian distributions in modeling the block LOT and LBT coefficients. The goodness of fit test carried out on large number of different test images shows that no single distribution can be used to model the distributions of all the AC coefficients of natural images. However the distribution of a majority of the significant AC coefficients can be modeled by the Generalized Gaussian distribution. The knowledge of the statistical distribution of LOT and LBT coefficients helps in design of optimal quantizers that may lead to minimum distortion and hence achieve optimal coding efficiency. [**Chapter 3**]

- The LT coefficients when rearranged into octave-like representation can be modeled in a manner similar to wavelet coefficients. The rearranged LT coefficients when used in applications like image compression, denoising, deblocking etc. can perform at par with relevant wavelet transform based methods. In this thesis, an extensive comparative study on the performance of Gaussian pdf and several non-Gaussian pdfs in modeling of rearranged orthogonal LT coefficients in different subbands has been performed. The Gaussian, Laplacian, Gamma, Generalized Gaussian and SNIG pdfs are considered in our experiments. Based on the KS goodness of fit test, we show that most of the subband coefficients for the majority of the natural images can be better

modeled by the Generalized Gaussian pdf. The knowledge of appropriate statistical distribution helps in developing more efficient algorithms for compression and denoising applications. [**Chapter 3**]

- Based on statistical distribution of LOT coefficients we have proposed three image denoising algorithms. We observed that the dyadic remapped LOT coefficients in different subbands exhibits highly non Gaussian statistics. The main idea is that since the LOT is a orthogonal transform, the signal and noise statistics can be modeled precisely in the LOT domain.

  In Chapter 3, based on KS goodness of fit test performed on dyadic remapped LOT coefficients, the Generalized Gaussian distribution was found to be the most appropriate statistical distribution for modeling the dyadic rearranged LT coefficients. The first LT based image denoising method uses a Bayesian estimator to obtain the estimate of noise free coefficients, which is based on modeling the global distribution of the rearranged LT coefficients using a Generalized Gaussian pdf. The experimental results show that the proposed scheme performs consistently better than the wavelet based image denoising scheme which uses a Bayesian estimator based on modeling the global distribution of the wavelet coefficients using a SNIG pdf. The SNIG pdf was demonstrated to be most appropriate pdf for modeling the wavelet transform coefficients of the natural images. The proposed method consistently outperforms the technique which uses the Bayesian estimator based on modeling the global distribution of the wavelet coefficients using the Generalized Gaussian pdf.

  In the second image denoising method, we have extended the local Wiener filtering concept in LT domain and next proposed a efficient doubly local Wiener filtering (LTDLWF) framework in LT domain. The low complexity local Wiener filtering in LT domain outperforms the local Wiener filtering results in wavelet transform domain for the majority of the images. The encouraging performance of local Wiener filtering in LT domain motivated us to propose a doubly local Wiener filtering framework in the same domain. The proposed doubly local Wiener filtering scheme in LT domain significantly improves the single local Wiener filtering performance both in terms of PSNR and visual quality. When compared to wavelet based doubly local Wiener filtering schemes which uses complex elliptic directional windows, the proposed LTDLWF scheme with simple square shaped windows shows comparable performance for the highly textured Barbara image. The LTDLWF scheme outperforms several well known wavelet based image denoising schemes.

The third image denoising algorithm models the rearranged LT coefficients in a subband using Laplace probability density function with local variance. This simple distribution is well able to model the locality and the heavy tailed property of LOT coefficients. A *maximum a posteriori* (MAP) estimator using the Laplace pdf with local variance is used for the estimation of noise free lapped transform coefficients. Experimental results show that the proposed low complexity image denoising method outperforms several well known wavelet based image denoising methods. This algorithm consistently outperforms the wavelet based Laplace prior method.

All the three image denoising algorithms proposed in Chapter 4 consistently outperform the previous LT based image denoising results in terms of PSNR. The objective and subjective performance of LTDLWF algorithm is the best among all the proposed LT domain image denoising methods. It is observed that the proposed LT based image denoising methods provide denoised images that are of improved visual quality and are comparable to that of many well known wavelet based image denoising methods. [**Chapter 4**]

- We have proposed two LT based image deblocking methods. The proposed image deblocking methods utilize the good denoising property of lapped orthogonal transforms to reduce the blocking artifacts.

  The first method is based on soft thresholding in the LOT domain. We have shown that there exists a strong correlation between the experimentally observed global 'optimal' threshold and the JPEG image Quality factor (Q_f). We have also demonstrated that the experimentally observed global 'optimal' threshold is highly correlated to the average of the first (3x3) values of the quantization table (Q_{av}). Our method can determine the soft threshold values that are adaptive to various compressed images using various quantization tables. The proposed low complexity method outperforms several well known image deblocking schemes in terms of PSNR and is able to reduce the blocking artifacts effectively while preserving true edges and textural information.

  In the second method we have proposed an efficient two stage algorithm for reduction of compression artifacts in block DCT compressed images using combined LT and adaptive bilateral filtering. We have modeled the degradation due to quantization noise as some additive noise. The first stage effectively reduces the blocking artifacts in the LOT domain using the concept of local Wiener filtering. We have demonstrated that the noise standard deviation has a high

correlation with the average of the first 3x3 values from the quantization matrix (Q_{av}). The noise standard deviation is made adaptive to the quantization table used in the compression process and is calculated from an empirical expression. The local variance of each coefficient is estimated from the local observation of the signal. The method used in the first stage of the proposed algorithm is spatially adaptive and this stage alone can outperform several well known wavelet and non wavelet based image deblocking methods. The test images processed by the first stage alone shows significant reduction of blocking artifacts while preserving true edges and textural information. The residual artifacts which include ringing is smoothed out using a edge preserving adaptive bilateral filter. The bilateral filter parameters are chosen based on an empirical study. We have demonstrated that the σ_i parameter of the bilateral filter is highly correlated to the noise standard deviation (σ_n) estimated in the first stage. The parameter σ_i is calculated from an empirical relation as a function of σ_n. Since σ_n is a function of Q_{av}, the parameter σ_i of bilateral filter becomes adaptive to the quantization tables used in the compression process. The final output of the proposed scheme shows excellent visual results with very good preservation of important image details. The proposed method outperforms many existing well known image deblocking methods both objectively and subjectively. The method outperforms one well known SA-DCT based image deblocking algorithm for many test images in terms of PSNR. When compared in terms of SSIM index results, the final output of the proposed 2 stage method outperforms the SA-DCT based algorithm for almost all the test images. It is to be noted that the SSIM index is known to be a good indicator of perceived image quality. The experimental results indicate that the proposed two stage algorithm for reduction of compression artifacts can preserve the textures better than the SA-DCT based method. [**Chapter 5**]

6.2 Tracks for future work

Many issues regarding statistical modeling of LT coefficients and its applications still remain open. A few possible research directions are outlined below

- *Evaluation of image coding performance*:

  It is well known that in transform based image coding systems the knowledge of the statistical distribution of the transform coefficients helps in design of optimal quantizers that may lead to minimum distortion and hence achieve optimal coding efficiency. Based on the KS and

Chi-square goodness of fit tests the Generalized Gaussian distribution was found to be the most appropriate statistical distribution for modeling the block LOT and LBT coefficients. It would be interesting to investigate the image coding performance of block LOT and LBT using quantizer based on the Generalized Gaussian distribution.

- *Reduction of speckle noise from medical ultrasound images*:

  Ultrasound images are inherently contaminated with speckle noise that makes image processing tasks like compression and segmentation very difficult. Further, speckle noise also affects the accuracy of diagnosis. Reduction of speckle noise is a challenging problem in the processing of medical ultrasound images. The performance of different non Gaussian pdfs in modeling the dyadic remapped LOT coefficients of the log transformed reflectivity of ultrasound images may be investigated. The knowledge of the appropriate statistical model then can be used to develop efficient homomorphic methods for reducing the speckle noise from medical ultrasound images.

- *LT based texture retrieval*:

  The two important tasks in a typical content based image retrieval (CBIR) system are: the feature extraction and the similarity measurement. The features used in CBIR system includes color, texture, shape and layout. Wavelet based texture extraction methods have shown good results in the literature. Statistical modeling is often used in CBIR systems. These methods use suitable statistical distribution to represent texture images in wavelet domain. Since the LTs are very good in preserving textural information present in images, it would be interesting to investigate the problem of texture retrieval in LT domain using the statistical framework where dyadic remapped LT coefficients in each subband are modeled by Generalized Gaussian distribution.

Bibliography

[1] N. Ahmad, T. Natarajan, and K. Rao, "Discrete cosine transform," *IEEE Transactions on Computers*, vol. C-23, no. 1, pp. 90–93, 1974.

[2] A. Z. Averbuch, A. Schclar, and D. L. Donoho, "Deblocking of block transform compressed images using weighted sums of symmetrically aligned pixels," *IEEE Transactions on Circuits and Systems for Video Technology*, vol. 14, no. 12, pp. 200–212, 2005.

[3] F. Bellifemine, A. Capellino, A. Chimienti, R. Picco, and R. Ponti, "Statistical analysis of the 2d-dct coefficients of the differential signal for images," *Signal Processing, Image Communication*, vol. 4, pp. 477–488, 1992.

[4] V. Bhaskaran and K. Konstantinides, *Image and video compression standards - Algorithms and architectures*, 2nd ed. Kluwer Academic Publishers, 1997.

[5] M. Bhaskaranand and J. D. Gibson, "Distributions of 3d dct coeffcients for video," in *Proc. of IEEE International Conference on Acoustics, Speech and Signal Processing*, 2009, pp. 793 – 796.

[6] M. I. H. Bhuiyan, M. O. Ahmad, and M. N. S. Swamy, "Spatially adaptive wavelet-based method using the cauchy prior for denoising the sar images," *IEEE Transactions on Circuits and Systems for Video Technology*, vol. 17, no. 4, p. 500507, 2007.

[7] ——, "Wavelet-based image denoising with the normal inverse gaussian prior and linear mmse estimator," *IET Image Processing*, vol. 2, no. 4, pp. 203–217, 2008.

[8] ——, "On the performance of non-gaussian distributions in modelling the wavelet coefficients of medical ultrasound images," in *14th IEEE International Conference on Electronics, Circuits and Systems*, 2007, pp. 1372–1375.

[9] P. Cassereau, "A new class of optimal unitary transforms for image processing," Master's thesis, Deptt. Elect. Eng. Comp. Sci., Mass. Inst. Technol, Cambridge, MA, 1985.

[10] R. Castagno, S. Marsi, and G. Ramponi, "A simple algorithm for the reduction of blocking artifacts in images and its implementation," *IEEE Transactions on Consumer Electronics*, vol. 44, no. 3, 1998.

[11] J. H. Chang, J. W. Shin, N. S. Kim, and S. K. Mitra, "Image probability distribution based on generalized gamma function," *IEEE Signal Processing Letters*, vol. 12, no. 4, pp. 325–328, 2004.

[12] S. Chang, B. Yu, and M. Vetterli, "Adaptive wavelet thresholding for image denoising and compression," *IEEE Transactions on Image Processing,*, vol. 9, p. 15321546, 2000.

[13] T. Chen, H. R. Wu, and B. Qiu, "Adaptive postfiltering of transform coefficients for the reduction of blocking artifacts," *IEEE Transactions on Circuits and Systems for Video Technology*, vol. 11, no. 5, pp. 594–602, 2001.

[14] M. S. Crouse, R. D. Nowak, and R. G. Baraniuk, "Wavelet-based signal processing using hidden markov models," *IEEE Transactions on Signal Processing*, vol. 46, p. 886902, 1998.

[15] M. N. Do and M. Vetterli, "Wavelet-based texture retrieval using generalized gaussian density and kullbackleibler distance," *IEEE Transactions on Image Processing*, vol. 11, no. 2, p. 13721375, 2002.

[16] D. L. Donoho, "De-noising by soft-thresholding," *IEEE Transactions on Information Theory*, vol. 41, pp. 613–627, 1995.

[17] D. L. Donoho and I. M. Johnstone, "Ideal spatial adaptation by wavelet shrinkage," *Biometrika*, vol. 3, no. 81, pp. 425–455, 1994.

[18] L. Duval and T. Q. Nguyen, "Lapped transform domain denoising using hidden markov trees," in *IEEE International Conference on Image Processing*, vol. 1, 2003, pp. 125–128.

[19] ——, "Hidden markov tree image denoising with redundant lapped transforms," in *IEEE International Conference on Acoustics, Speech and Signal Processing*, vol. 3, 2004, pp. 193–196.

[20] J. D. Eggerton and M. D. Srinath, "Statistical distributions of image dct coefficients," *Computer Electrical Engineering*, vol. 12, pp. 137–145, 1986.

[21] I. K. Eom and Y. S. Kim, "Wavelet-based denoising with nearly arbitrarily shaped windows," *IEEE Signal Processing Letters*, vol. 11, no. 12, pp. 937–940, 2004.

[22] G. Fan and X.-G. Xia, "Wavelet-based statistical image processing using hidden markov tree model," in *Proc. of 34th Annual Conference on Information Sciences and Systems*, 2000.

[23] G. Fan and X. G. Xia, "Image denoising using local contexual hidden markov model in the wavelet domain," *IEEE Signal Processing Letters*, vol. 8, no. 5, pp. 125–128, 2001.

[24] M. A. T. Figueiredo and R. D. Nowak, "Wavelet-based image estimation:an empirical bayes approach using jeffrey's non informative prior," *IEEE Transactions on Image Procesing*, vol. 10, no. 3, p. 13221331, 2001.

[25] A. Foi, V. Katkovnik, and K. Egiazarian, "Pointwise shape adaptive dct for high quality denoising and deb-locking of grayscale and color images," *IEEE Transactions on Image Processing*, vol. 16, no. 5, pp. 1395–1411, 2007.

[26] S. P. Ghael, A. M. Sayeed, and R. G. Baraniuk, "Improved wavelet denoising via empirical wiener filtering," *SPIE*, pp. 389–399, 1997.

[27] R. A. Gopinath, "Wavelet-based post-processing of low bit rate transform coded images," in *IEEE International Conference on Image Processing*, 1994, pp. 913–917.

[28] I. J. Group. [Online]. Available: http://www.ijg.org

[29] A. Hanssen and T. A. Oigard, "The normal inverse gaussian distribution for heavy-tailed processes," in *IEEE EURASIP Workshop on Nonlinear Signal and Image processing*, 2001.

[30] T. C. Hsung and D. P. K. Lun, "Application of singularity detection for the deblocking of jpeg decoded images," *IEEE Transactions on Circuits Systems II*, vol. 45, no. 5, pp. 640–644, 1998.

[31] *MPEG-4 video verication model version 18.0 (VM-18)*, ISO/IEC JTC1/SC29/WG11 Std., 2001.

[32] ITU-T, *Video codec for audiovisual services at p 64 kbps*, Recommendation H.261 Std., 1993.

[33] A. K. Jain, *Fundamental of Digital image processing.* Englewoods Cliffs, NJ:Prentice hall, 1989.

[34] I. H. Jang, N. C. Kim, and H. J. So, "Iterative blocking artifact reduction using a minimum mean square error filter," *Signal Processing*, vol. 83, pp. 2607–2619, 2003.

[35] N. S. Jayant and P. Noll, *Digital Coding of waveforms.* Prentice Hall, 1984.

[36] R. L. Joshi and T. R. Fischer, "Comparison of generalized gaussian and laplacian modeling in dct image coding," *IEEE Signal Processing Letters*, vol. 2, no. 5, pp. 81–82, 1995.

[37] S. M. Kay, *Fundamentals of statistical signal processing: estimation theory.* Prentice-Hall Ltd, Englewood Cliffs, USA, 1993.

[38] M. Kazubek, "Wavelet domain image denoising by thresholding and wiener filtering," *IEEE Signal Processing Letters*, vol. 10, no. 11, pp. 324–326, 2003.

[39] N. C. Kim, I. H. Jang, D. H. Kim, and W. H. Hong, "Reduction of blocking artifact in block-coded images using wavelet transform," *IEEE Transactions on Circuits and Systems for Video Technology*, vol. 8, no. 3, pp. 253–257, 1998.

[40] P. lang Shui, "Image denoising algorithm via doubly local wiener filtering with directional windows in wavelet domain," *IEEE Signal Processing Letters*, vol. 12, no. 10, pp. 681–684, October 2005.

[41] P. lang Shui and Y.-B. Zhao, "Image denoising algorithm using doubly local wiener filtering with block adaptive windows in wavelet domain," *Signal Processing*, vol. 87, pp. 1721–1734, 2007.

[42] A. W. C. Liew and H. Yan, "Blocking artifacts suppression in block coded images using overcomplete wavelet representation," *IEEE Transactions on Circuits and Systems for Video Technology*, vol. 14, no. 4, pp. 450–461, 2004.

[43] J. Liu and P. Moulin, "Image denoising based on scale-space mixture modeling of wavelet coefficients," in *IEEE International Conference on Image processing*, vol. 42, October 1999, pp. 2181–2193.

[44] S. Mallat, "A theory for multiresolution signal decomposition: The wavelet representation," *IEEE Transactions on Pattern Recognition Machine Intelligence*, vol. 11, pp. 674–693, 1989.

[45] H. S. Malvar, "The lot : Transform coding without blocking effects," *IEEE Transactions on Accoustics, Speech and Signal Processing*, vol. 37, no. 4, pp. 553–559, 1989.

[46] ——, *Signal Processing with Lapped Transforms.* Norwood, MA : Artech House, 1992.

[47] ——, "Lapped biorthogonal transform for transform coding with reduced blocking and ringing artifacts," in *IEEE International Conference on Acoustics, Speech and Signal Processing*, vol. 3, 1997, pp. 2421–2424.

[48] ——, "Biorthogonal and nonuniform lapped transforms for transform coding with reduced blocking and ringing artifacts," *IEEE Transactions on Signal Processing*, vol. 46, no. 4, pp. 1043–1053, April 1998.

[49] ——, "Fast progressive image coding without wavelets," in *Data Compression Conference*, 2000, pp. 243–252.

[50] S. Marsi, R. Castagno, and G. Ramponi, "A simple algorithm for the reduction of blocking artifacts in images and its implementation," *IEEE Transactions on Consumer Electronics*, vol. 44, no. 3, pp. 1062–1070, 1998.

[51] M. K. Michak, I. Kozintsev, and K. Ramchandran, "Low complexity image denoising based on statistical modelling of wavelet coefficient," *IEEE Signal Processing Letters*, vol. 6, no. 12, pp. 300–303, 1999.

[52] S. Minami and A. Zakhor, "An optimization approach for removing blocking artifacts in transform coding," *IEEE Transactions on Circuit and Systems for Video Technology*, vol. 5, no. 2, pp. 74–82, 1995.

[53] P. Moulin and J. Liu, "Analysis of multiresolution image denoising schemes using generalized gaussian and complexity priors," *IEEE Transactions on Information Theory*, vol. 45, no. 3, p. 909919, 1999.

[54] F. Muller, "Distribution shape of two dimensional dct coefficients of natural images," *Electronics Letters*, vol. 29, no. 22, pp. 1935–1936, 1993.

[55] V. K. Nath, D. Hazarika, and A. Mahanta, "Blocking artifacts reduction using adaptive bilateral filtering," *International Conference on Signal processing and communications*, vol. 6, pp. 243–250, 2010.

[56] O. Onalan, "Financial risk management with normal inverse gaussian distributions," *International research Journal of Finance and Economics*, no. 38, pp. 104–115, 2010.

[57] H. Paek, R. C. Kim, and S. U. Lee, "On the pocs based postprocessing technique to reduce the blocking artifacts in transform coded images," *IEEE Transactions on Image Processing*, vol. 8, no. 3, pp. 358–367, 1998.

[58] S. H. Park and D. S. Kim, "Theory of projection onto the narrow quantization constraint set and its application," *IEEE Transactions on Image Processing*, vol. 8, no. 10, pp. 1361–1373, 1999.

[59] W. B. Pennebaker and J. L. Mitchell, *JPEG still image data compression standard.* New York: Van Nostrand Reinhold, 1992.

[60] D. Po and M. N. Do, "Directional multiscale modeling of images using the contourlet transform," *IEEE Transactions on Image Processing*, vol. 15, no. 6, p. 16101620, 2006.

[61] J. Portilla, V. Strela, M. J. Wainwright, and E. P. Simoncelli, "Image denoising using scale mixtures of gaussians in the wavelet domain," *IEEE Transactions on Image Processing*, vol. 12, no. 11, pp. 1338–1351, 2003.

[62] H. Rabbani, "Image denoising in steerable pyramid domain based on local laplace prior," *Pattern Recognition*, vol. 42, pp. 2181–2193, 2009.

[63] H. Rabbani and M. Vafadust, "Image / video denosing based on a mixture of laplace distributions with local parameters in multidimensional complex wavelet domain," *Signal Processing*, vol. 88, no. 11, pp. 158–173, 2008.

[64] B. S. Raghvendra and P. S. Bhat, "Image denosing using mixture distributions with lapped transforms," in *National Conference of Communications*, 2006, pp. 217–220.

[65] H. C. Reeve and J. S. Lim, "Reduction of blocking artifacts in image coding," *Optical Engineeering*, vol. 23, no. 1, pp. 34–37, 1984.

[66] R. C. Reininger and J. D. Gibson, "Distributions of the two dimensional dct coefficients for images," *IEEE Transactions on Communications*, vol. 31, no. 6, pp. 835–839, 1983.

[67] V. K. Rohatgi and A. K. E. Saleh, *An Introduction to Probability and Statistics.* John Wiley and Sons, 2001.

[68] J. Romberg, H. Choi., and R. Baraniuk, "Bayesian tree structured image modeling using wavelet-domain hidden markov models," in *SPIE Technical conference on Mathemetical modeling, Bayesian estimation and Inverse problems*, 31-44.

[69] R. Rosenholts and A. Zakhor, "Iterative procedures for reduction of blocking artifacts in transform domain image coding," *IEEE Transactions on Circuits and Systems for Video Technology*, vol. 2, no. 2, pp. 91–95, 1992.

[70] A. Said and W. A. Pearlman, "A new and efficient image codec based on set partitioning in hierarchical trees," *IEEE Transactions on circuits and systems for Video technology*, vol. 6, pp. 243–250, 1996.

[71] L. Sendur and I. W. Selesnick, "Bivariate shrinkage functions for wavelet-based denoising," *IEEE Transactions on Signal Processing*, vol. 50, p. 27442756, 2002.

[72] ——, "Bivariate shrinkage with local variance estimation," *IEEE Signal Processing Letters*, vol. 9, no. 12, pp. 438–441, 2002.

[73] J. Shapiro, "Embedded image coding using zero trees of wavelet coefficients," *IEEE Transactions on Signal Processing*, vol. 41, pp. 3445–3462, 1993.

[74] K. Sharifi and A. Leon-Garcia, "Estimation of shape parameter for generalized gaussian distributions in subband decompositions of video," *IEEE Transactions on Circuits and Systems for Video Technology*, vol. 5, no. 1, p. 5256, 1995.

[75] E. P. Simoncelli and E. H. Adelson, "Noise removal via bayesian wavelet coring," in *IEEE International Conference on Image Processing*, vol. 1, 1996, pp. 379 –382.

[76] S. R. Smoot and L. A. Rowe, "Study of dct coefficient distributions," *SPIE*, vol. 2657, pp. 403–411, 1996.

[77] G. Strang and T. Nguyen, *Wavelets and Filter Banks*. Wellesley-Cambridge Press, 1996.

[78] C. Tomasi and R. Manduchi, "Bilateral filtering for gray and color images," in *IEEE International Conference on Computer Vision*, 1998, pp. 839–846.

[79] T. D. Tran and T. Q. Nguyen, "A progressive transmission image coder using linear phase uniform filter banks as block transforms," *IEEE Transactions on Image processing*, vol. 8, no. 11, pp. 1493–1507, 1999.

[80] Z. Wang, A. C. Bovik, H. R. Sheikh, and E. P. Simoncelli, "Image quality assessment : From error visibility to structural similarity," *IEEE Transactions on Image processing*, vol. 13, no. 4, pp. 600–612, 2004.

[81] S. Wu, H. Yan, and Z. Tan, "An efficient wavelet-based deblocking algorithm for highly compressed images," *IEEE Transactions on Circuits and Systems for Video Technology*, vol. 11, no. 11, pp. 1193–1198, 2001.

[82] Z. Xiong, O. G. Guleryuz, and M. T. Orchard, "A dct based embedded image coder," *IEEE Signal Processing Letters*, vol. 3, no. 11, pp. 289–290, 1996.

[83] Z. Xiong, M. T. Orchard, and Y. Zhang, "A deblocking algorithm for jpeg compressed images using overcomplete wavelet representation," *IEEE Transactions on Circuits and Systems for Video Technology*, vol. 7, no. 2, pp. 433–437, 1997.

[84] J. Xu, S. Zheng, and X. Yang, "Adaptive video blocking artifact removal in discrete hadamard transform domain," *Optical Engineering*, vol. 45, no. 8, 2006.

[85] S. Yang and T. Q. Nguyen, "Denoising in the lapped transform domain," in *IEEE International Conference on Acoustics, Speech and Signal Processing*, vol. 6, 2003, pp. 173–176.

[86] Y. Yang and N. P. Galatsanos, "Projection based spatially adaptive reconstruction of block transform compressed images," *IEEE Transactions on Image Processing*, vol. 4, no. 7, pp. 896–908, 1995.

[87] ——, "Removal of compression artifacts using projections onto convex sets and line process modeling," *IEEE Transactions on Image Processing*, vol. 6, no. 10, pp. 1345–1357, 1997.

[88] Y. Yang, N. P. Galatsanos, and A. K. Katsaggelos, "Regularized reconstruction to reduce blocking artifacts of block discrete cosine transform compressed images," *IEEE Transactions on Circuits and Systems for Video Technology*, vol. 3, no. 6, pp. 421–432, 1993.

[89] G. Zhai, W. Zhang, X. Yang, W. Lin, and Y. Xu, "Efficient image deblocking based on postfiltering in shifted windows," *IEEE Transactions on Circuits and Systems for Video Technology*, vol. 18, no. 1, pp. 122–126, 2008.

[90] M. Zhang and G. K. Bahadir, "Compression artifact reduction with adaptive bilateral filtering," in *Visual Communications and Image Processing*, vol. 7257, 2009.

[91] M. Zhang and B. K. Gunturk, "Multiresolution bilateral filtering for image denoising," *IEEE Transactions on Image Processing*, vol. 17, no. 12, pp. 2324–2333, 2008.

[92] Z. F. Zhou and P. L. Shui, "Contourlet-based image denoising algorithm using directional windows," *IEE Electronics Letters*, vol. 43, no. 2, 2007.